2015-12

East Sea spatial and temporal variability of thermohaline structure and circulation identified from observational (t, s) profiles

Choi, Hyewon

Monterey, California: Naval Postgraduate School

NAVAL POSTGRADUATE SCHOOL

MONTEREY, CALIFORNIA

THESIS

EAST SEA SPATIAL AND TEMPORAL VARIABILITY OF THERMOHALINE STRUCTURE AND CIRCULATION IDENTIFIED FROM OBSERVATIONAL (T, S) PROFILES

by

Hyewon Choi

December 2015

Thesis Advisor: Peter C. Chu
Co-Advisor: Chenwu Fan

Approved for public release; distribution is unlimited

THIS PAGE INTENTIONALLY LEFT BLANK

REPORT DOCUMENTATION PAGE			*Form Approved OMB No. 0704–0188*
Public reporting burden for this collection of information is estimated to average 1 hour per response, including the time for reviewing instruction, searching existing data sources, gathering and maintaining the data needed, and completing and reviewing the collection of information. Send comments regarding this burden estimate or any other aspect of this collection of information, including suggestions for reducing this burden, to Washington headquarters Services, Directorate for Information Operations and Reports, 1215 Jefferson Davis Highway, Suite 1204, Arlington, VA 22202-4302, and to the Office of Management and Budget, Paperwork Reduction Project (0704-0188) Washington, DC 20503.			
1. AGENCY USE ONLY ***(Leave blank)***	**2. REPORT DATE** December 2015	**3. REPORT TYPE AND DATES COVERED** Master's thesis	
4. TITLE AND SUBTITLE EAST SEA SPATIAL AND TEMPORAL VARIABILITY OF THERMOHALINE STRUCTURE AND CIRCULATION IDENTIFIED FROM OBSERVATIONAL (T, S) PROFILES			**5. FUNDING NUMBERS**
6. AUTHOR(S) Hyewon Choi			
7. PERFORMING ORGANIZATION NAME(S) AND ADDRESS(ES) Naval Postgraduate School Monterey, CA 93943-5000			**8. PERFORMING ORGANIZATION REPORT NUMBER**
9. SPONSORING /MONITORING AGENCY NAME(S) AND ADDRESS(ES) N/A			**10. SPONSORING / MONITORING AGENCY REPORT NUMBER**
11. SUPPLEMENTARY NOTES The views expressed in this thesis are those of the author and do not reflect the official policy or position of the Department of Defense or the U.S. Government. IRB Protocol number ____N/A____.			
12a. DISTRIBUTION / AVAILABILITY STATEMENT Approved for public release; distribution is unlimited			**12b. DISTRIBUTION CODE**

13. ABSTRACT (maximum 200 words)

Synoptic monthly varying 3-D gridded temperature and salinity data for the East Sea were established in this study (January 1960 to December 2013). From the gridded data, seasonal and inter-annual variability of thermohaline structure and circulation of the East Sea were analyzed.

Found was a low salinity effect caused by the Amur River's discharge into the Tatar Strait, and a one-month delay after maximum discharge in September. The research discovered another low salinity effect through the Korea Strait in summer by the Changjiang River's discharge into the East China Sea, which identified with a matching strong inflow in the surface layer of the Korea Strait in an absolute geostrophic velocity distribution. The anticyclonic pattern of the Ulleung Warm Eddy in the intermediate layer and an opposite pattern in the deep layer were noticed.

Inter-annual variability by EOF analysis shows that the difference in heat content according to area is more significant in the surface layer, while the freshwater content difference is more significant in the deep layer. By temporal analysis, an increase of heat content in all areas and layers since 1990 and a decrease of the freshwater content in the deep layer since mid-1990s were identified.

14. SUBJECT TERMS East Sea, Japan East Sea, Seasonal variability, Inter-annual variability, Temperature distribution, Salinity distribution, Spatial variability, Temporal variability, Heat content, Freshwater content, absolute geostrophic velocity, water mass			**15. NUMBER OF PAGES** 145
			16. PRICE CODE
17. SECURITY CLASSIFICATION OF REPORT Unclassified	**18. SECURITY CLASSIFICATION OF THIS PAGE** Unclassified	**19. SECURITY CLASSIFICATION OF ABSTRACT** Unclassified	**20. LIMITATION OF ABSTRACT** UU

NSN 7540–01-280-5500 Standard Form 298 (Rev. 2–89)
Prescribed by ANSI Std. 239–18

THIS PAGE INTENTIONALLY LEFT BLANK

Approved for public release; distribution is unlimited

EAST SEA SPATIAL AND TEMPORAL VARIABILITY OF THERMOHALINE STRUCTURE AND CIRCULATION IDENTIFIED FROM OBSERVATIONAL (T, S) PROFILES

Hyewon Choi
Lieutenant Commander, Republic of Korea Navy
B.A., Republic of Korea Naval Academy, 2003

Submitted in partial fulfillment of the
Requirements for the degree of

MASTER OF SCIENCE IN PHYSICAL OCEANOGRAPHY

From the

NAVAL POSTGRADUATE SCHOOL
December 2015

Approved by: Peter C. Chu
Thesis Advisor

Chenwu Fan
Co-Advisor

Peter C. Chu
Chair, Department of Oceanography

THIS PAGE INTENTIONALLY LEFT BLANK

ABSTRACT

Synoptic monthly varying 3-D gridded temperature and salinity data for the East Sea were established in this study (January 1960 to December 2013). From the gridded data, seasonal and inter-annual variability of thermohaline structure and circulation of the East Sea were analyzed.

Found was a low salinity effect caused by the Amur River's discharge into the Tatar Strait, and a one-month delay after maximum discharge in September. The research discovered another low salinity effect through the Korea Strait in summer by the Changjiang River's discharge into the East China Sea, which identified with a matching strong inflow in the surface layer of the Korea Strait in an absolute geostrophic velocity distribution. The anticyclonic pattern of the Ulleung Warm Eddy in the intermediate layer and an opposite pattern in the deep layer were noticed.

Inter-annual variability by EOF analysis shows that the difference in heat content according to area is more significant in the surface layer, while the freshwater content difference is more significant in the deep layer. By temporal analysis, an increase of heat content in all areas and layers since 1990 and a decrease of the freshwater content in the deep layer since mid-1990s were identified.

THIS PAGE INTENTIONALLY LEFT BLANK

TABLE OF CONTENTS

LIST OF FIGURES

THIS PAGE INTENTIONALLY LEFT BLANK

LIST OF TABLES

THIS PAGE INTENTIONALLY LEFT BLANK

LIST OF ACRONYMS AND ABBREVIATIONS

DSM	Deep Salinity Minimum
ECS	East China Sea
EKWC	East Korea Warm Current
EOF	Empirical Orthogonal Function
ES	East Sea
ESBW	East Sea Bottom Water
ESCW	East Sea Central Water
ESDW	East Sea Deep Water
ESIW	East Sea Intermediate Water
JB	Japan Basin
KHOA	Korea Hydrographic and Oceanographic Administration
LCC	Liman Cold Current
NKCC	North Korea Cold Current
OSD	Optimal Spectral Decomposition
PC	Principal Component
SPF	Subpolar Front
SST	Sea Surface Temperature
TWC	Tsushima Warm Current
TWW	Tsushima Warm Water
UB	Ulleung Basin
WOD	World Ocean Data
YB	Yamato Basin
YR	Yamato Rise

THIS PAGE INTENTIONALLY LEFT BLANK

ACKNOWLEDGMENTS

First of all, I would like to express sincere gratitude to my thesis advisor, Distinguished Professor Peter C. Chu, for his invaluable support, scientific guidance and passion. He opened my eyes toward a physical oceanography academic world. I also would like to thank to my co-advisor, Mr. Chenwu Fan, for his time, patience and professional knowledge in MATLAB programming. Without their help, I would not have been able to accomplish my thesis in a timely manner.

I also would like to express my great appreciation to the Republic of Korea and my navy for allowing me the opportunity of this invaluable academic experience.

Moreover, I need to thank to all professors at NPS who helped me in every field during my education. Thank you to my classmates, especially LTJG. Nuri Karaaslan, Turkish navy, who shared experiences and tips while doing this research.

Most of all, thank you to my devoted wife, Jaesun Kim, who always supported me to achieve my academic goals. She deserves the biggest part of my appreciation.

THIS PAGE INTENTIONALLY LEFT BLANK

I. INTRODUCTION

A. EAST SEA

The East Sea (hereafter ES), widely known as Sea of Japan after Japan's forced occupation of Korea in early twentieth century, is a marginal sea of the western Pacific Ocean (Kantha et al., 1994), between the Asian continent, the Japanese archipelago, and Sakhalin Island (see Figure 1). Thus, the ES acts like a canal "for the exchange of materials along the Asian Pacific coast." Since the ES is situated at "mid-latitude, heat energy from the Equator is transported toward the North Pole" through the ES (National Geographic Information Institute, 2015).

Figure 1. East Sea Topography and Neighboring Countries

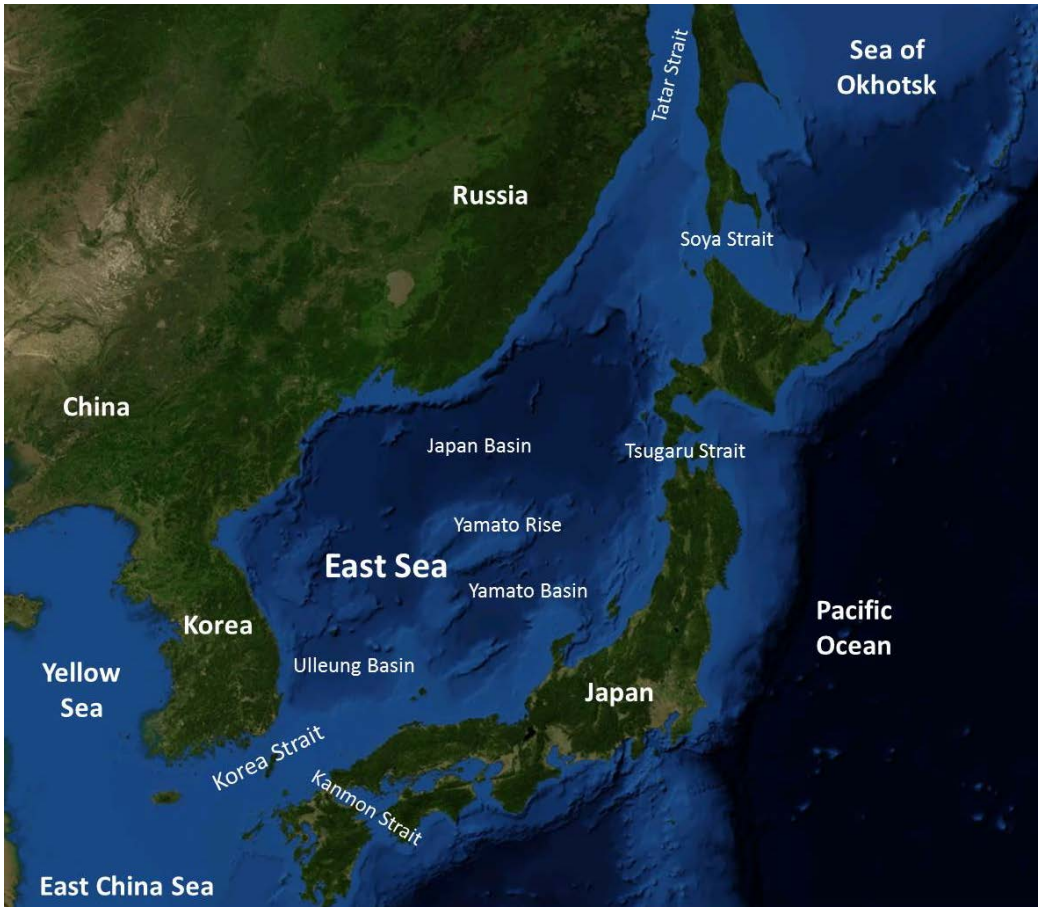

The ES is “a unique” deep “semi-enclosed ocean basin overlaid by” significant “monsoon surface winds,” and “covers an area of” 978,000km^2. “It has a maximum depth of” (Chu et al., 2005) 3,742m and mean depth of 1,752m. The ES is isolated from the Pacific Ocean except for narrow (< 200km) and shallow (< 250m) straits, which connect the ES with the North Pacific through the Korea, Kanmon, and Tsugaru Straits and with the Okhotsk Sea through the Soya and Tatar Straits. This geography “hinders water exchange thereby isolating the water and aquatic life of the” ES “from the neighboring seas and oceans” (Dobrovolsky and Zalogin, 1982).

The ES has three major basins, the Japan Basin (JB) in the north, Ulleung Basin (UB) in the southwest, and Yamato Basin (YB) in the southeast, and a shallower bank (240 ~ 500m deep) in center of the ES called Yamato Rise (YR) (see Figure 2). The ES holds great scientific interest as a microcosmic prototype ocean since it has characteristics of a large ocean such as basin-wide circulation pattern, a western boundary current, Subpolar Front (SPF), mesoscale eddy activities, and deep water formation. Therefore, studying long-term variabilities of the ES can improve understanding of the characteristics of the open ocean (Chu et al., 2001).

Figure 2. Bottom Topography of the ES

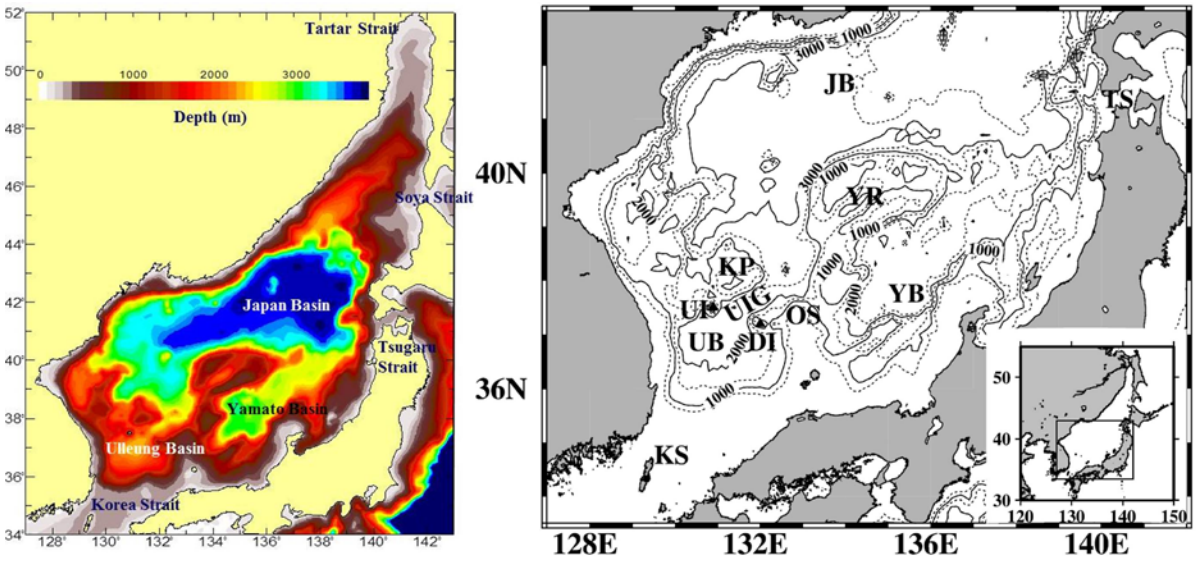

(left) Bathymetric chart of the ES. Most part of ES is 1,500 ~ 3,500m depth. Japan Basin is the deepest basin among three major basins in the ES. (Source: http://slideplayer.com/slide/1633181/)

(right) Area map. DI : Dok Island, JB : Japan Basin, KP : Korea Plateau, KS : Korea Strait, OS : Oki Spur, TS : Tsugaru Strait, UB : Ulleung Basin, UI : Ulleung Island, UIG : Ulleung Interplain Gap, YB : Yamato Basin, YR :Yamato Rise (from Park, K., J. Y. Chung, and K. Kim, 2004a: Sea surface temperature fronts in the East (Japan) Sea and temporal variations. *Geophys. Res. Lett.*, **31**, L07304)

The ES has winter and summer monsoons every year. In the winter monsoon season, a cold wind blows from the northwest over the ES, generated by the

> Siberian high pressure system located over the East Asian continent. Radiative cooling and persistent cold air advection maintain cold air over the JES. The northwest–southeast oriented jet stream is positioned above the JES. Such a typical winter monsoon pattern lasts nearly six months (Nov–Apr). During the summer monsoon, a warm and weaker southeast wind blows over the JES. Such a typical summer monsoon pattern lasts nearly 4 months (mid-May to mid-Sep). (Chu et al., 2001)

B. NATURAL RESOURSES AND INTERESTS

Fishery was the conventional main economic activity on the ES. The East Korea Warm Current and North Korean Cold Current meet around 40°N (see Figure 3), generating a sub-polar front which makes a good fishing ground. Squid is a representative species of the warm current and the king crab is representative of the cold current. Other important species are salmon, walleye pollack, herring, cod, anger fish, mullet, filefish, flatfish, mackerel, anchovy, sardine, and sea eel. Due to fishery's importance and because the distances between neighboring countries are shorter than 200NM which is the standard for drawing an Exclusive Economic Zone (EEZ), disputes between Korea-Japan and Russia-Japan have arisen to secure more fishing ground in the ES. As a result of the rapid growth of related technologies and ocean geography, interest in the underwater mineral resources of the ES has increased in the 21st century.

Figure 3. Monthly Averages of the ES Surface Temperature (°C)

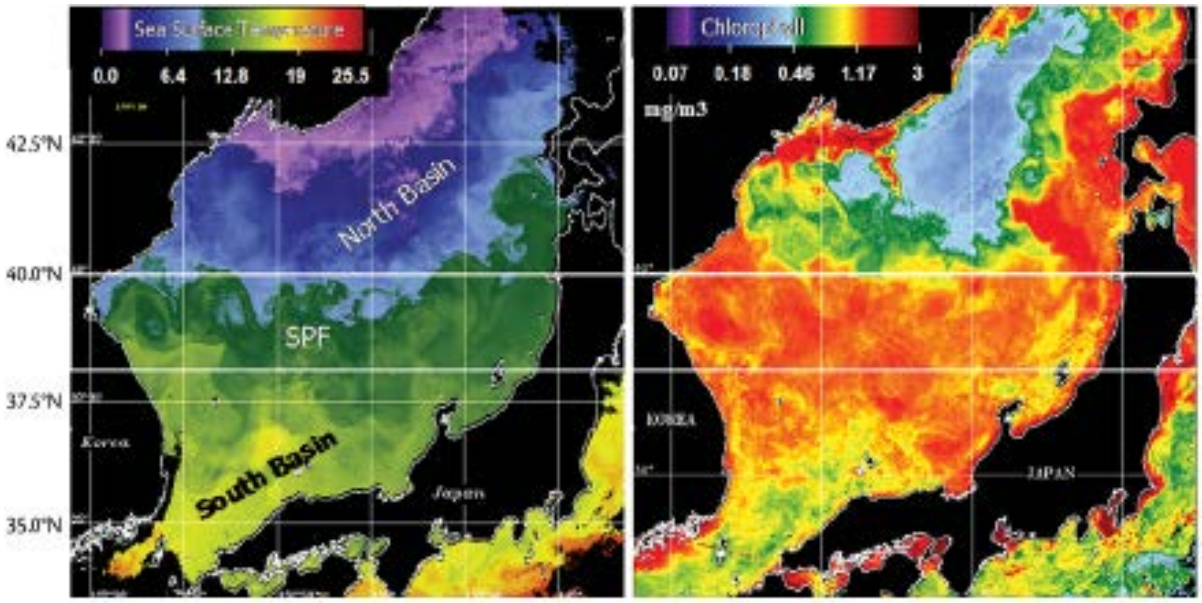

On the left plot and chlorophyll (mg m^{-3}) on the right plot in April 1999, "from satellites, showing the distinct northern and southern regions of the ES separated by the Subpolar Front (SPF) (delineated by the horizontal white lines). Sea surface temperature and chlorophyll from NOAA Advanced Very High Resolution Radiometer (AVHRR) and Sea-viewing Wide Field-of-view Sensor (SeaWIFS) satellites, respectively." (Source: Ashjian, C. J., R. Arnone, C. S. Davis, B. Jones, M. Kahru, C. M. Lee, and B. G. Mitchell, 2006: Biological structure and seasonality in the Japan/East Sea.) A good fishing ground is located around this SPF and high chlorophyll concentrated area.

The presence of substantial gas hydrates (see Figure 4) in UB was reported in the 1990s and 2000s by utilizing 12kHz side scan sonar images, core samples, and multi-channel reflection seismic data and finally confirmed by piston coring and a deep-drilling expedition in 2007 (Ryu et al., 2009). Gas hydrates are considered a source of natural gas that is essentially 100% methane (CH4) gas (Englezos and Lee, 2005). An economically proper extraction technology has not been proven yet, but these natural gas hydrates are considered as a potential vast energy resource (Lee et al., 2013).

Figure 4. Burning Gas Hydrates and Gas Hydrates in Sediment Deposits

Source: Center for Marine Environmental Sciences, 2015: General Geology / Marine Geology. Accessed 10 December 2015. [Available online at http://www.marum.de/en/general_geology__marine_geology.html].

C. MILITARY INTERESTS

The ES is not only the sea surrounded by Russia, Japan, and Korea but also a crossroad of complex interests of other countries, such as China and United State. Additionally, all of these countries are relatively stronger than others in the region. All of the neighboring countries are in the top nine of the greatest military powers in the world (Global Firepower (GFP), 2015: 2015 World Military Strength Rankings. Accessed 10 December 2015. [Available online at http://www.globalfirepower.com/]), within the top 11 oil-consuming countries, and also within the top 11 exporting countries (CIA The World Factbook, 2015: Country Comparison / Exports. Accessed 10 December 2015. ; https://www.cia.gov/library/publications/the-world-factbook/rankorder/2078rank.html]).

The military and strategic value of the ES is important enough to determined nation's vicissitude as learned in history such as Battle of Tsushima in Russo-Japanese War. Bilateral or trilateral combined exercises are common among the neighboring countries such as Joint Sea (China-Russia) (see Figure 5), Foal Eagle (South Korea-United States), and others. Therefore, the neighboring countries that are aware of the strategic importance of the ES have been continuously reinforcing their naval power, including submarines. Submarine detection is very difficult, due to the complex underwater circumstances of the ES, so the neighboring countries have constantly been

promoting oceanographic research. For example, in the 1990s, the U.S Office of Naval Research (ONR) sponsored the ES research initiative as part of an effort to learn more about the underwater circumstances of the ES.

Figure 5. Chinese Sovremenny-Class Destroyer Taizhou Arrives at Vladivostok, Russia on 20 August 2015 to Take Part in The Joint Sea 2015 Naval Drills in the ES Between Russia and China

Source: IHS Jane's 360, 2015: China, Russia conduct large-scale joint naval exercise. Accessed 10 December 2015. [Available online at http://www.janes.com/article/53759/china-russia-conduct-large-scale-joint-naval-exercise].

D. OBJECTIVE

An in-depth study is required to address the interest in the ES from various fields. However, each neighboring countries of the ES carried out their own oceanographic researches individually due to cultural and language differences. Even the cooperation between the countries is remarkably improved recently; researches have carried out without enough understanding and knowledge of neighboring countries (Danchenkov et al., 2006).

Accordingly, the spatial and temporal variations of the ES are important to examine and confirm previous studies. In this thesis, inter-annual, seasonal, and monthly temperature, salinity, and current velocity variation are analyzed. Using data from the World Ocean Database (WOD) from 1960 to 2013, long-term spatial and temporal analysis is used to determine thermohaline structure and current patterns and also to

verify anomalies. The importance of this thesis is that the general circulation in the ES is primarily driven by the thermohaline circulation combined with its mesoscale variability. Data analysis is followed by comparison with a number of previous studies. Thus, this provides a better understanding of the general circulation patterns of the ES.

E. THESIS ORGANIZATION

In chapter II, ES oceanography, including characteristics of the water masses and seasonal variability, is explained. This is based on previous research for easier understanding and background knowledge about the ES thermohaline structure and circulation.

In chapter III, the data and methodology used in this thesis are introduced. The WOD, the source of the data set for long-term analysis, and analysis methods such as OSD, P-vector inverse method, and EOF analysis are explained with applied equations.

In chapter IV, seasonal variability analysis of the data is handled, and a comparison of these results and previous research is presented. For easier understanding, this chapter is divided into several subsections by variables such as seasonal and monthly variations for the temperature, salinity and absolute geostrophic velocity of the levels of the ES's water column, and heat content and freshwater content of the each separated layer.

In chapter V, inter-annual variability analysis of the data is handled. This part focuses on the spatial and temporal variability of heat content and freshwater content to find abnormalities and a changing trend of ocean circumstances.

In chapter VI, this study's results are summarized, and recommendations for further study are presented.

THIS PAGE INTENTIONALLY LEFT BLANK

II. OCEANOGRAPHY OF THE ES

A. CURRENTS AND WATER MASSES

The major currents in the ES are the Tsushima Warm Current (TWC) and Liman Cold Current (LCC). The TWC flows from the East China Sea through the Korea Strait between the Korean peninsula and Kyushu Island, Japan. The LCC flows from the Sea of Okhotsk through the Tatar Strait between Sakhalin Island and the Asian continent (see Figure 6).

Figure 6. Major Currents in the ES

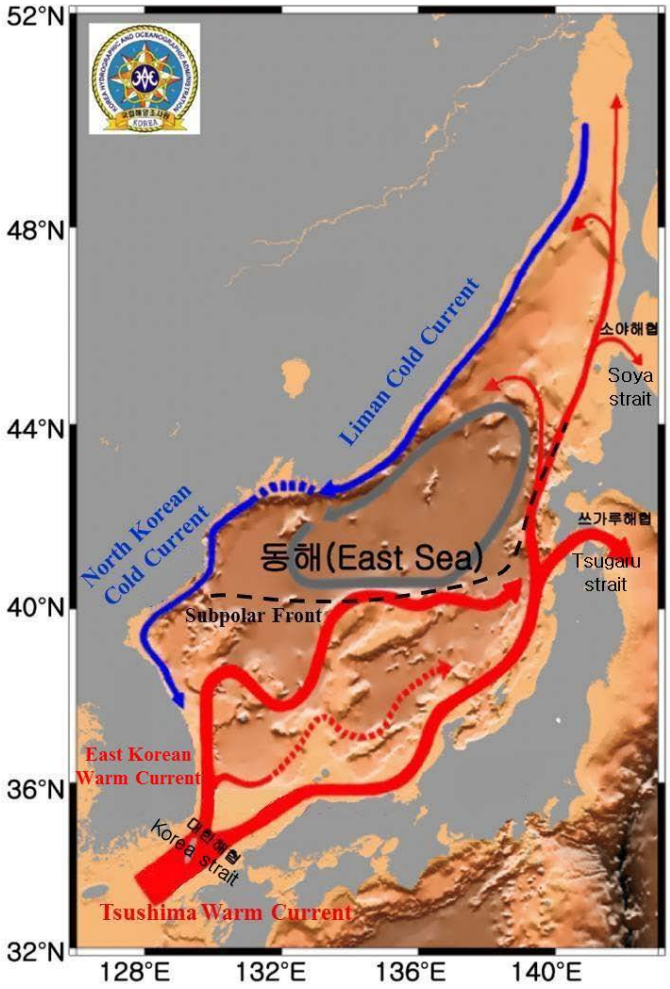

Source: Korea Hydrographic and Oceanographic Administration (KHOA), 2015: Accessed 10 December 2015. Adapted from, Korea Hydrographic and Oceanographic Agency, http://sms.khoa.go.kr/koofs/kor/introduce/a_current_wfavg.asp.

The “water exchange between the” ES “and the North Pacific Ocean is limited to the upper layer,” because “three main channels leading into the” ES (“Korea, Tsugaru and Soya Straits) are very shallow” and narrow (Kim et al., 2004). The Korea Strait is the widest and deepest strait among these channels. The TWC affects the ES more than the LCC since most water inflow to the ES is through the Korea Strait, which is divided into two channels by Tsushima Island. The western channel (Korea side) is as deep as 230m where the eastern (Japan side) channel’s sill depth is approximately 120m (Teague et al., 2006). “As the TWC enters the ES through Korea Strait, it splits into three separate branches, the Nearshore Branch, the Offshore Branch and the East Korea Warm Current (EKWC). The majority of the warm water flows along the western coastline of Honshu Island and exits through Tsugaru Strait.” (Hoiles et al., 2012) The EKWC and the North Korea Cold Current (NKCC) meet around 40°N and generate the SPF (see Figure 7). The EKWC further flows across the ES and meets the Nearshore Branch, which flows along the Japanese coast and eventually flows through the Tsugaru and Soya Strait.

Figure 7. VHRR IR Image 1745 from NOAA 4

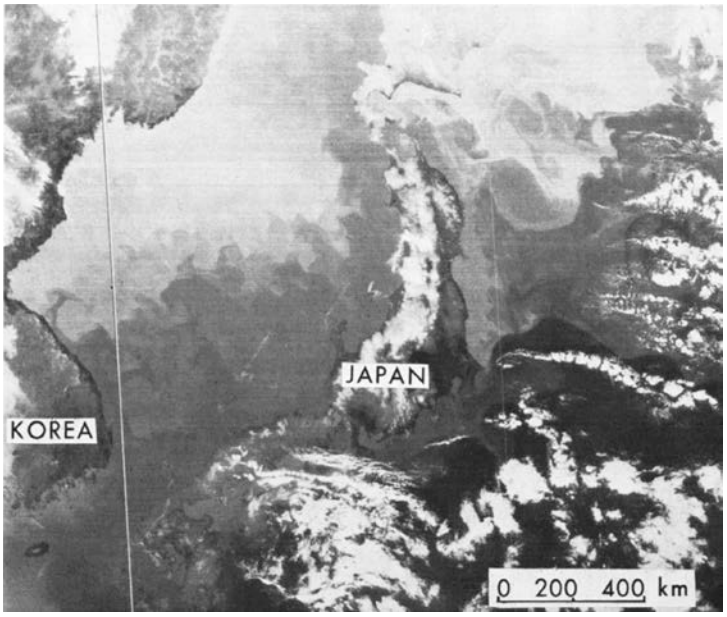

This image was obtained on April 4, 1975. The zonally oriented front in the ES extends from Korea to Japan. The warmest water (in darkest shades of gray) east of Japan is part of the Kuroshio. The Oyashio front appears to the north of the Kuroshio. Source: Legeckis, R., 1978: A survey of worldwide sea surface temperature fronts detected by environmental satellites. *Journal of Geophysical Research: Oceans (1978–2012)*, **83**, 4501–4522.

The SPF is about 100 ~ 150km wide and acts as a thermal boundary of the surface water of the ES, which separates warm saline waters provided by the TWC in the southern region and colder and less saline waters provided by the LCC in the northern region (Robinson and Brink 1998). Therefore, the upper layer of the southern half of the ES is warmer compared to upper layer of the northern half year-round (Moriyasu 1972).

Antithetically, the vertical separation of the water masses in the ES is more complicated. The "vertical distribution of water properties in the ES is characterized by a distinction between its upper and deeper layers" (National Geographic Information Institute, 2015: The Geography of Dokdo. Accessed 10 December 2015. [Available online at http://www.ngii.go.kr/dokdoen/contents/contentsView.do?rbsIdx=54#none]). Except for the saline warm water from the surface to 100m depth in the southern region of the ES, the majority of the water column in the ES is filled with cold water (< 1°C); this cold water is called "Proper Water" (PW) which concept was first introduced by Uda (1934). Later, Moriyasu (1972) mentioned that high salinity water occupies the southern half of the ES over the permanent thermocline approximately 200m depth, which is called the Tsushima Warm Water (TWW) (see Table 1).

East Sea Intermediate Water (ESIW) was first reported by Kim and Chung (1984). ESIW is located southwestern area of the ES near Korea Strait beneath the TWW from 200m to 300m depth. ESIW is a distinct salinity minimum layer with very highly dissolved oxygen and low temperatures of 1 ~ 3°C. By these characteristics, Kim and Chung identified that ESIW is originated from northern area of the ES where cold water formed in winter by air–sea interaction caused by Siberian wind since this characteristics of water cannot be generated locally in the UB. Their research of ESIW supports evidence that waters from northern area of the ES are adequately dynamic enough to reach the UB. Thus, ESIW is regarded as a tracer to understand intermediate depth's circulation pattern. Abnormally cold waters off the eastern Korean coast in the upper layer of the UB in 1981 were reported by Kim and Legeckis (1986). This is the area where usually East Korean Warm Current (EKWC) was observed, thus by this anomaly, cold waters which are generated in northern area of the ES could have effect on the direction of the TWC (Kim et al., 2004).

According to Sudo (1986), the Proper Water is divided into upper and deep water by the 0.1°C water temperature isotherm around 800 ~ 1,000m depth. Subsequently Senjyu and Sudo (1993) clarified the definition of the Upper Portion of the Proper Water (UPPW). The result is that the temperature–salinity relationship in the ES is similar "to that of the open ocean, except that the range of salinity variation for deep waters in the ES is of the order of 0.001 psu, one order of magnitude lesser than that of the open oceans" (Kim et al., 2004).

The ES has a "1,000m thick, homogeneous layer near the bottom. This homogeneous layer is found at all over the ES deeper than 2,000m and this water is called East Sea Bottom Water (ESBW)" (Kim et al. 2004). A weak vertical salinity minimum is observed at the depth of 1,500m, and it is thus called the Deep Salinity Minimum (DSM) (see Table 2). DSM presumed to have originated by convection or salinity rejection in western subpolar gyre. The East Sea Deep Water (ESDW) sits between the DSM and the ESBW. The ESDW has a potential temperature lower than 0.12°C. "The East Sea Central Water (ESCW) is defined between the intermediate waters and the DSM" (Kim et al. 2004). The ESCW is approximately 1,100m thick between depths of 400m, the depth of the salinity maximum and 1,500m, the depth of the DSM.

The data in this thesis from World Ocean Data 2013 has 57 levels of observed data down to 1,500m depth; therefore, for the purpose of simpler analysis, the water masses have been divided into three layers. Surface warm layer is surface to 200m in depth, the intermediate layer from 200m to 400m in depth, and the deep layer from 400m to 1,500m depth.

Table 1. Definition of Water Masses in the ES.

water masses	Potential temperature (°C)	Salinity (psu)	Dissolved oxygen (lmol/l)	Remarks
Tsushima Warm Water	>10	>34.3		Primarily south of 41°N
East Sea Intermediate Water	1–5	< 34.06	>250	western Japan Basin, Ulleung Basin
High Salinity Intermediate Water	1–5	>34.07	>250	Eastern Japan Basin
East Sea Central Water	0.12–0.6	>34.067		Deeper limit at 1500dbar (DSM)
East Sea Deep Water	<0.12	34.067–34.070		Upper limit at 1500dbar (DSM)
East Sea Bottom Water layer	<0.073	34.070		Homogeneous mixed

Source: Kim, K. et al., 2004: Water masses and decadal variability in the East Sea (Sea of Japan). *Prog.Oceanogr.*, **61**, 157–174.

Table 2. Water Masses and Structures, Identifying Characteristics, and Source.

Water Mass	Distinguishing Characteristic	Source
Tsushima Warm Water	Vertical salinity maximum in upper 150 m	Tsushima Strait inflow, local evaporation and subduction
East Sea Intermediate Water	Vertical salinity minimum in upper ocean	Subduction of fresh subpolar water southward across the Subpolar Front
Upper Japan Sea Proper Water		Open ocean convection in the subpolar gyre
High-Salinity Intermediate Water (Upper Japan Sea Proper Water)	Vertical salinity maximum between 200–500m	Convective cooling of Tsushima Warm Water in the northeast subpolar gyre
Central Water	Water between the salinity maximum and deep salinity minimum	Deep convection
Lower Japan Sea Proper Water		Most likely sea-ice formation and brine rejection
Deep Salinity Minimum (Lower East Sea Proper Water)	Weak vertical salinity minimum at about 1,500m depth	Convection or brine rejection in the western subpolar gyre
Oxygen Minimum (Lower East Sea Proper Water)	Vertical oxygen minimum at about 2,000m depth	Biological consumption in water column and in sediments
Deep Water (Lower East Sea Proper Water)	Water between the salinity minimum and the bottom layer	Most likely sea-ice formation and brine rejection
Bottom Water (Lower East Sea Proper Water)	High oxygen bottom layer (following winter 2001)	Sea-ice formation and brine rejection
Bottom Adiabatic Layer (Lower East Sea Proper Water)	Vertically homogeneous bottom layer	Turbulent mixing of bottom waters

Source: Talley, L. D. et al., 2006: Water Masses, *Oceanography*, **19**, 32.

B. SEASONAL VARIABILITY OF THE ES

Seasonal variability is strongly related with seasonal wind over the ES. The ES has distinct winter and summer seasonal winds. In winter, the typical wind direction is northwesterly, and in summer, the typical wind direction is southerly (see Figure 8).

The ES's "water properties and circulation are determined to a large extent by the significant difference in surface forcing between summer and winter; a typical

subtropical climate in summer and severe cold-air outbreaks in winter." (Park et al., 2005) Occasional outbreaks are brought by very cold Siberian air with combination of surrounding surface topography.

The ES is surrounded by high coastal mountains (2,000 ~ 3,000m) and separated from the Manchurian Plain and the Asian continent by a coastal mountain range along the western side (see Figure 9). When the cold air mass from the continent moves southward, this coastal range is the obstacle to overcome in order to reach the ES. The temperatures of January mean surface air in the continent are -20°C to -15°C. Because the dominant airflow direction is entirely toward offshore, the air temperature is rising to around 0°C along the Russian east coast due to serious coastal mountain lee-side warming (see Figure 10) (Dorman et al., 2004).

Mostly the amplitude difference greater than 9°C in of the annual cycle is found in the northern region of the SPF (Park et al., 2004a), and this difference is approximately 7°C, relatively smaller in the southern region (Yoon, 1982). This results is caused by large SST differences such as ~16°C (-1 to 15°C) in winter and ~10°C (16 to 26°C) in summer between north and south (see Figure 11). Amplitudes are greater in the northern regions and lesser in the southern region. "This low amplitude region is also associated with the occurrence of cold water masses in summer" (Park et al., 2005).

Figure 8. Spatial Distribution of Monthly-Mean Wind Vectors (2000 ~ 2008)

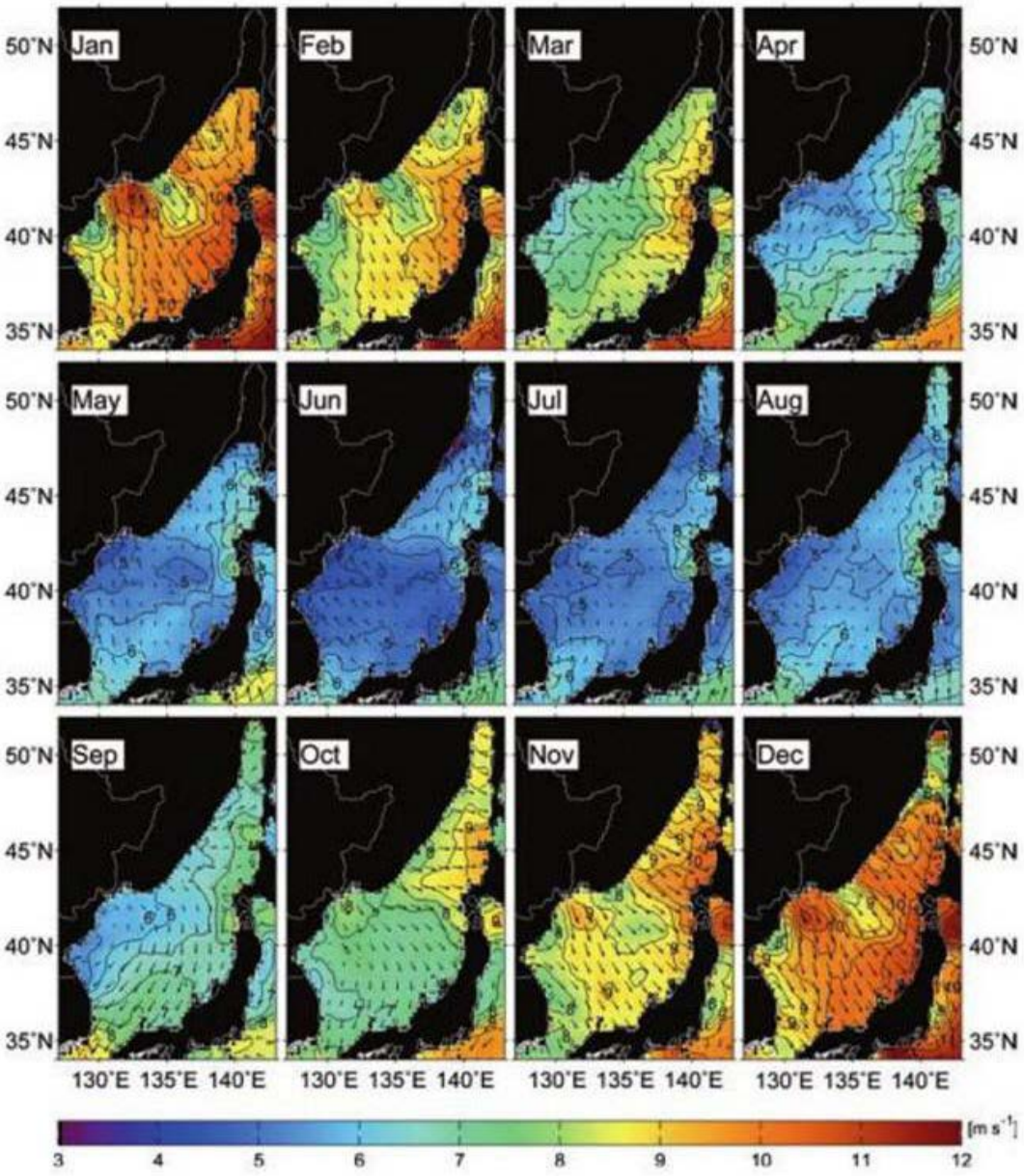

Spatial distribution of monthly-mean wind vectors from 9 years (2000 ~ 2008) of QuikSCAT data over the ES shows a significant difference between winter and summer wind characteristics. The wind speed is higher in winter (monthly mean greater than $8ms^{-1}$), from November reaching a peak (> $10ms^{-1}$) in January of the next year and lasting into March. This northwesterly wind blows fast especially south of Vladivostok and along the Primorye coast due to the Vladivostok Gap. The southerly wind starts blowing in April, and the speed of it is relatively weaker than in winter. The slowest southerly wind blows in June (monthly mean less than $5ms^{-1}$) and lasts until August Source: Chang, K., C. Zhang, C. Park, D. Kang, S. Ju, S. Lee, and M. Wimbush, 2015: Oceanography of the East Sea.

Figure 9. Connecting Waters and Surrounding Lands of the ES Presented on Earth's Curved Surface

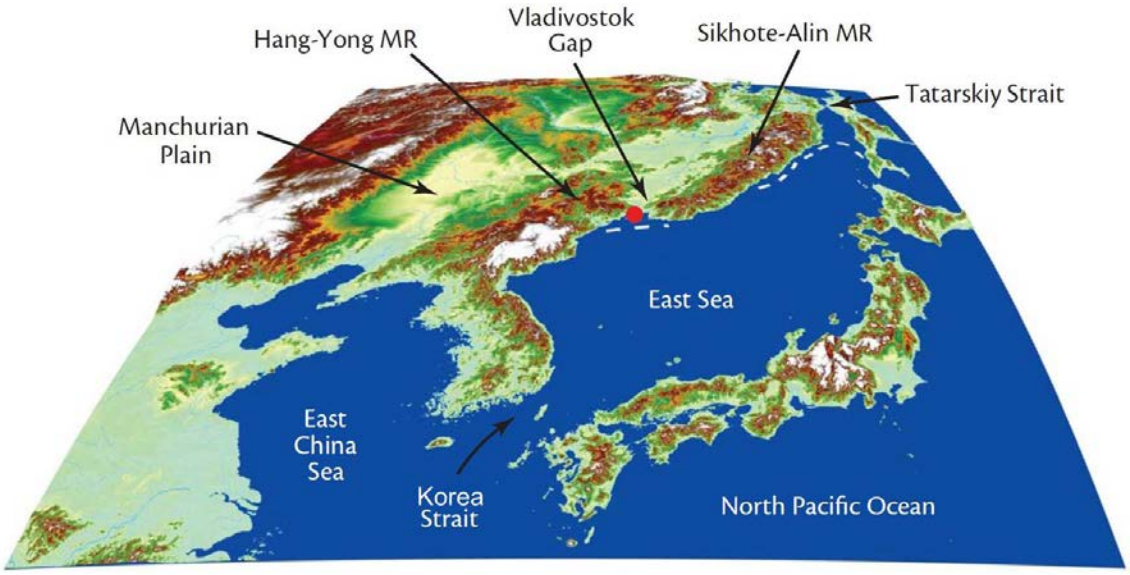

The image's vertical exaggeration shows the Asian continental landform and the high coastal mountain ranges along the Korean and Russian coasts bordering the ES. The white dashed lines are the mean edge of the winter fast sea ice along the Russian coast off Vladivostok (red dot) and north near the Tatar Strait. The Vladivostok Gap is the only major gap in the Russian coastal mountain ranges connecting the Manchurian Plain and lower plateau to the ES. Adapted from Dorman, C. E., C. A. Friehe, D. Khelif, A. Scotti, J. Edson, R. C. Beardsley, R. Limeburner, and S. S. Chen, 2006: Winter atmospheric conditions over the Japan/East Sea: The structure and impact of severe cold-air outbreaks. *Oceanography-Washington DC-Oceanography Society-*, **19**, 96.

Figure 10. Siberian Winter Wind over the ES

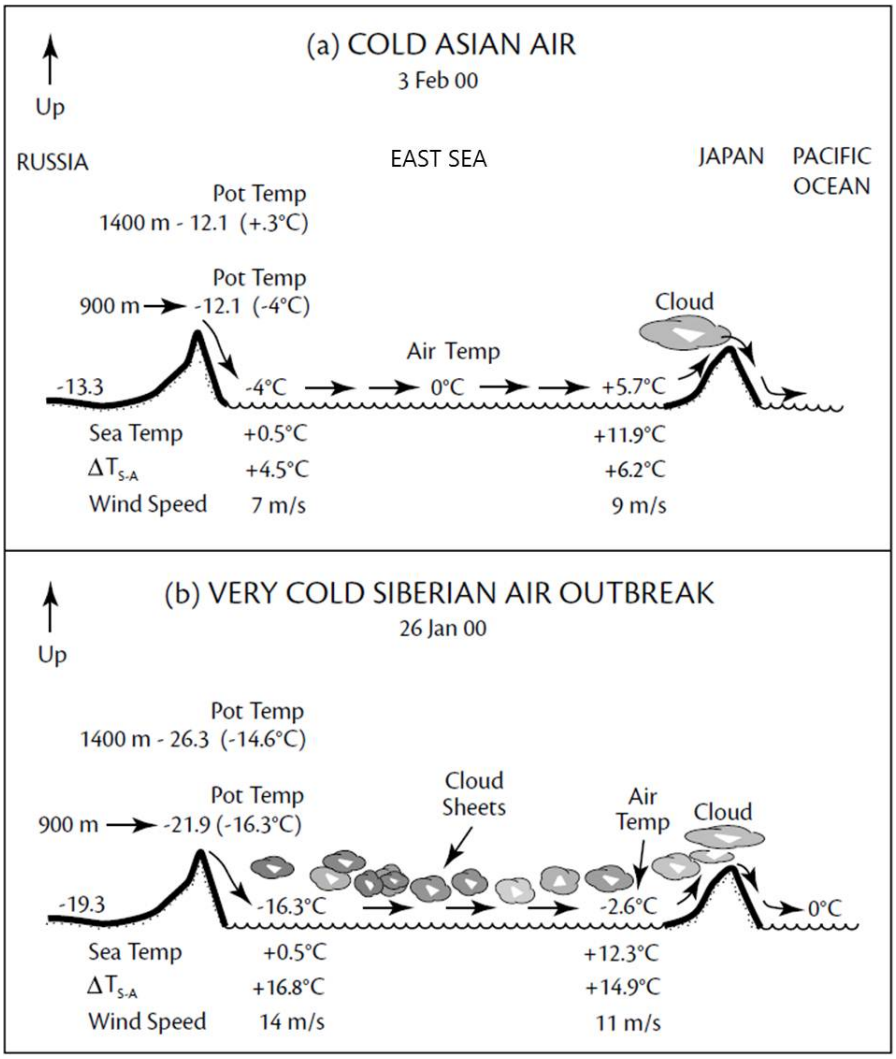

"A schematic of the role of coastal mountains in lee-side warming during (a) cold Asian air flow conditions and (b) a very cold Siberian air outbreak (VCSAO) moving over the ES." There is a much larger difference between sea-air and colder surface-air and wind speed during the VCSAO. Source: Dorman, C. E., R. C. Beardsley, N. Dashko, C. Friehe, D. Kheilf, K. Cho, R. Limeburner, and S. Varlamov, 2004: Winter marine atmospheric conditions over the Japan Sea. *Journal of Geophysical Research: Oceans (1978–2012)*, **109**.)

Figure 11. ES Monthly Mean Current and SST Plot (1993 ~ 2013)

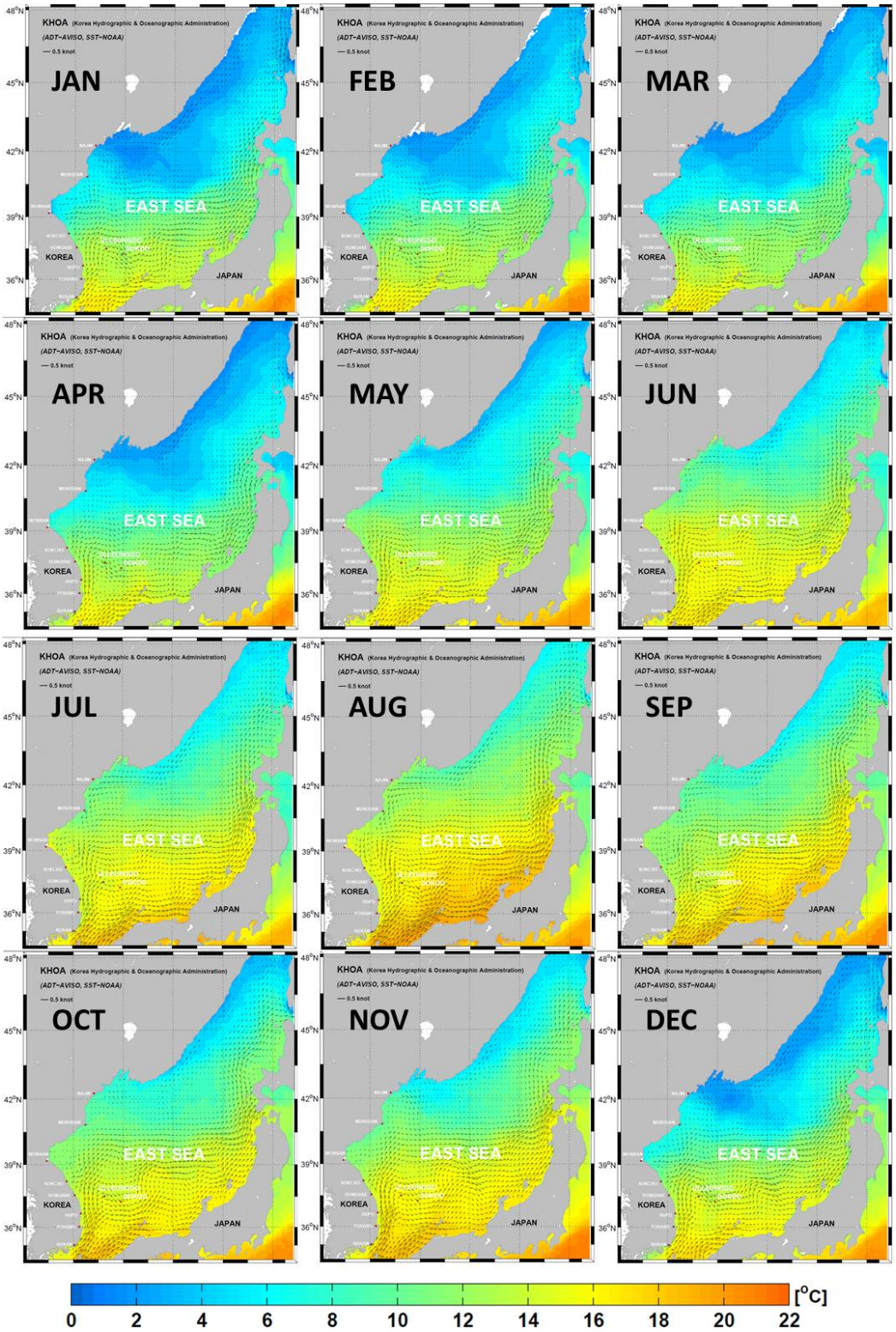

SST is strongly related with monthly-mean wind vectors. (Adapted from, Korea Hydrographic and Oceanographic Administration (KHOA))

THIS PAGE INTENTIONALLY LEFT BLANK

III. DATA AND METHODOLOGY

A. WORLD OCEAN DATABASE

Data for this thesis is based on the World Ocean Database (WOD) 2013 which is the largest internationally opened ocean data source. WOD contains general oceanographic data such as temperature, salinity, dissolved oxygen and nutrients, etc. "WOD is produced by the NOAA National Oceanographic Data Center (NODC) and its' co-located World Data Center for Oceanography" (Boyer et al., 2013). The "WOD is a product built by merging thousands of originators' data sets from many different countries and organizations." (Levitus et al., 2013) "These data sets, which are sent to NODC/WDC in many different formats, are put into a common database, and quality control is performed on the data." (Conkright et al., 1994) The WOD was first released in 1994, and updates have been released approximately every four years. The latest version was released in 2013; thus, the WOD 2013 (WOD13) was used in this research. Since the WOD is an enormous archive of ocean data, a changing tendency of a particular ocean characteristic could be found by analyzing the WOD with selected time window and region. In this thesis, the observational (T, S) profiles from the WOD 2013 from 1960 to 2014 are used.

The data from WOD13 are organized according to the geographical area of the ES. Data were analyzed into temporal distribution and spatial distribution for each variable by utilizing the MATLAB program. Location and frequency of data collection were obtained by this analysis.

Most of the data were collected between 1990s and 2000s, but some were collected between 2000s and 2010s. There were two remarkable research projects on the ES in the 1990s; CREAMS (Circulation Research of East Asian Marginal Seas) and the U.S. Office of Naval Research (ONR) program. These two research efforts may have resulted in the higher frequency of the data collection in 1990s. CREAMS was a long-term research program in the ES, conducted internationally by Korean, Japanese and Russian oceanographers. During the CREAMS, ocean data were collected from 1993 to

1999. Subsequently, another international effort was initiated by the U.S. Office of Naval Research (ONR) from 1997 to 2001; this program encompassed over 15 various research projects (Danchenkov et al., 2006).

Figure 12. Temporal Distribution of the Temperature Profiles

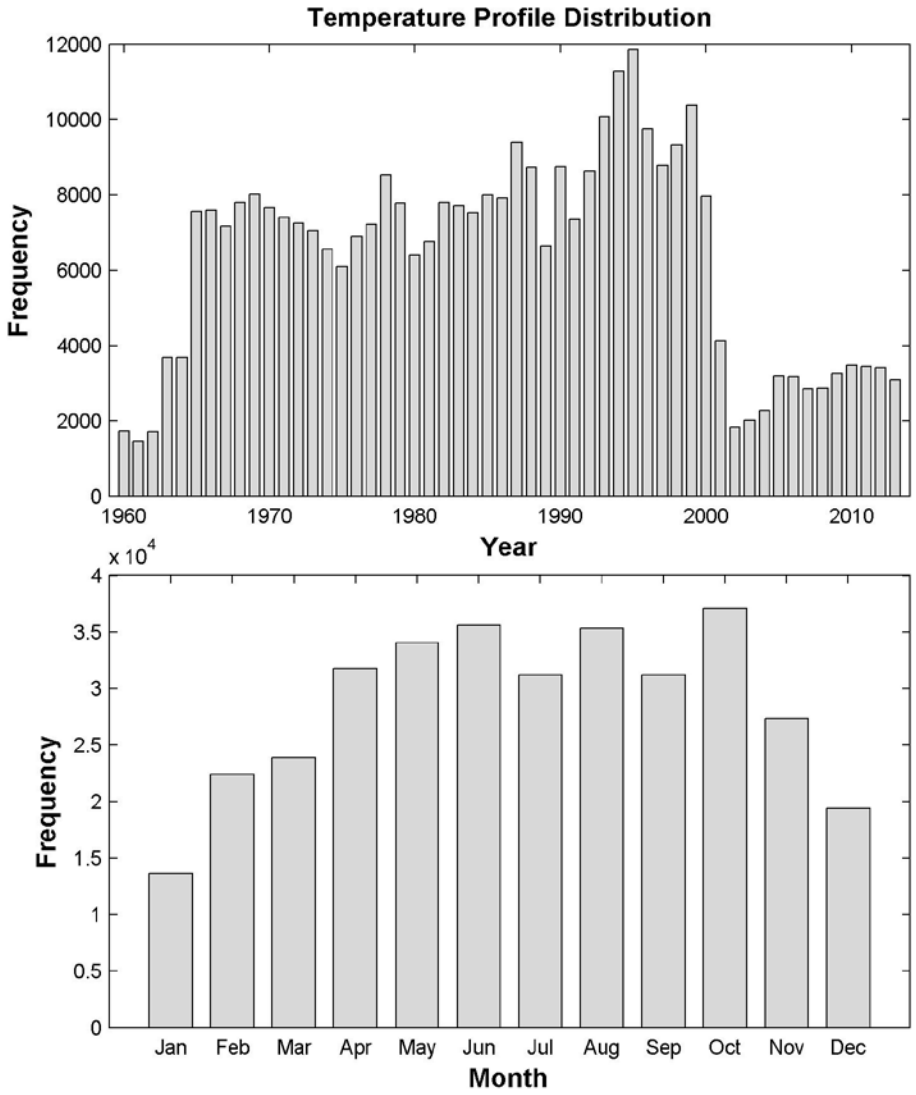

This shows a higher annual frequency in 1990s and seasonal frequency in winter.

By the monthly distribution, data were collected in summer relatively more often than in winter (see Figure 12 and 13). Severe sea conditions may cause this distribution: the highest wave height is approximately 2 ~ 4.4m, and the average wave height is 2m in

winter, while the highest wave height is approximately 0.7 ~ 1m, and the average wave height is 0.4 ~ 0.5m in summer. (Adapted from Korea Ocean Observing and forecasting System, http://sms.khoa.go.kr/koofs/kor/observation/obs_past_search_statistic.asp).

Figure 13. Temporal Distribution of the Salinity Profiles

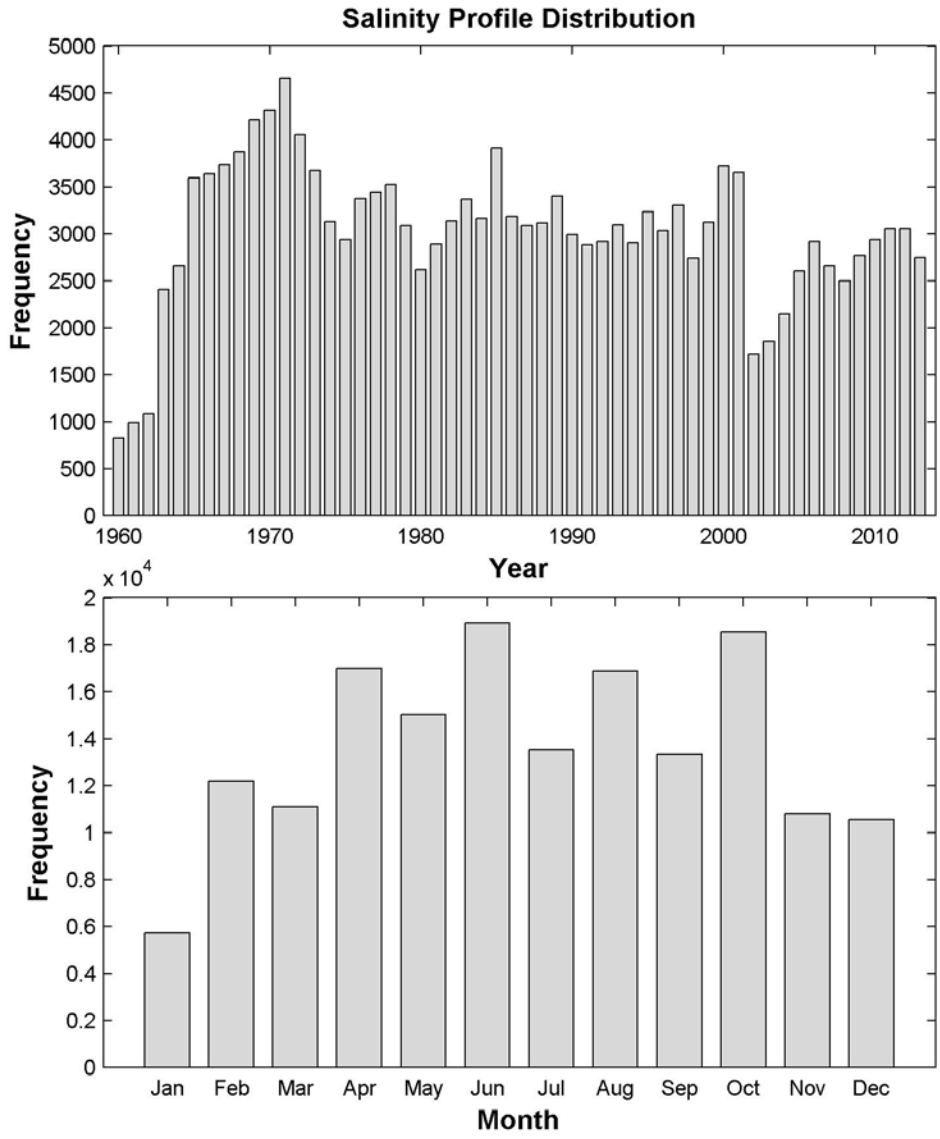

Most data were collected in 1970s; however the total numbers for the temperature and salinity data are still the highest in 1990s. There is a higher seasonal frequency in summer and lower frequency in winter, as also seen in the temperature profiles.

Dense ocean data collection in the ES is shown on spatial distribution of the both temperature and salinity profiles. From 1960 to 2013, 342,617 and 163,502 data points for temperature and salinity respectively were collected in the ES (see Figure 14). Relatively fewer data were collected around the Tatar Strait and off the North Korean coast. This may be the result of the current political climate in North Korea since North Korea is an internationally closed country. The winter fast sea ice along the Russian coast and near the Tatar Strait (see Figure 9) may be the reason for lesser data collection of the Tatar Strait area.

Figure 14. Spatial Distribution of the Temperature and Salinity Profiles

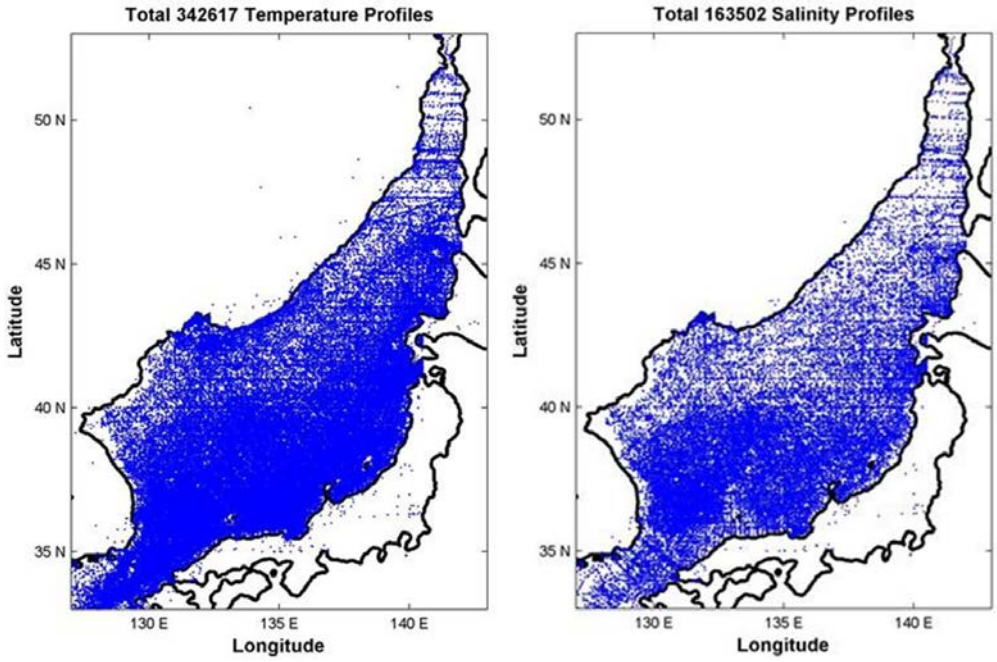

Spatial distribution of temperature profiles (left), spatial distribution of the salinity profiles (right). There are twice as many temperature data points as salinity data points.

These seasonal and spatial data collection frequency and density are more clearly shown in monthly spatial data profiles (see Figure 15 and 16). Very few temperature and salinity data were collected near the Tatar Strait area and off the Russian coast from November to March. There is a large difference in the number of data collected in each season; about two times more data were collected in summer. For all seasons, both temperature and salinity data were poorly collected off North Korea.

Figure 15. Monthly Spatial Temperature Data Profile

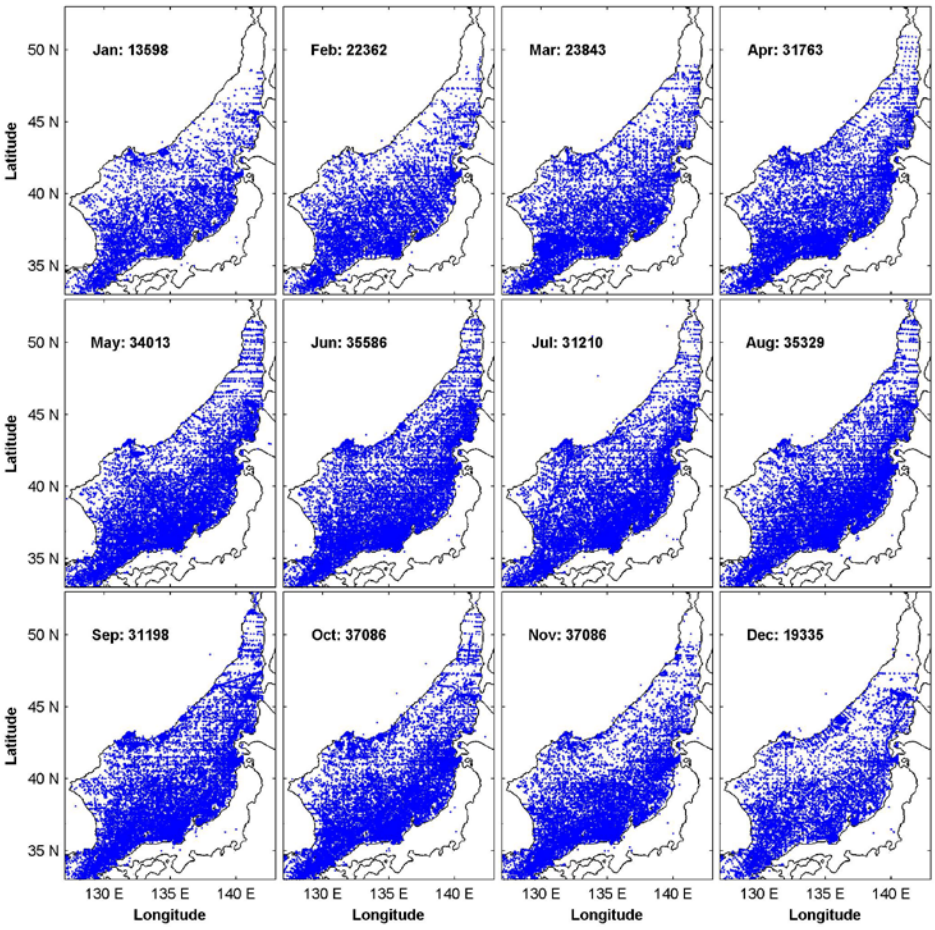

Figure 16. Monthly Spatial Salinity Data Profile

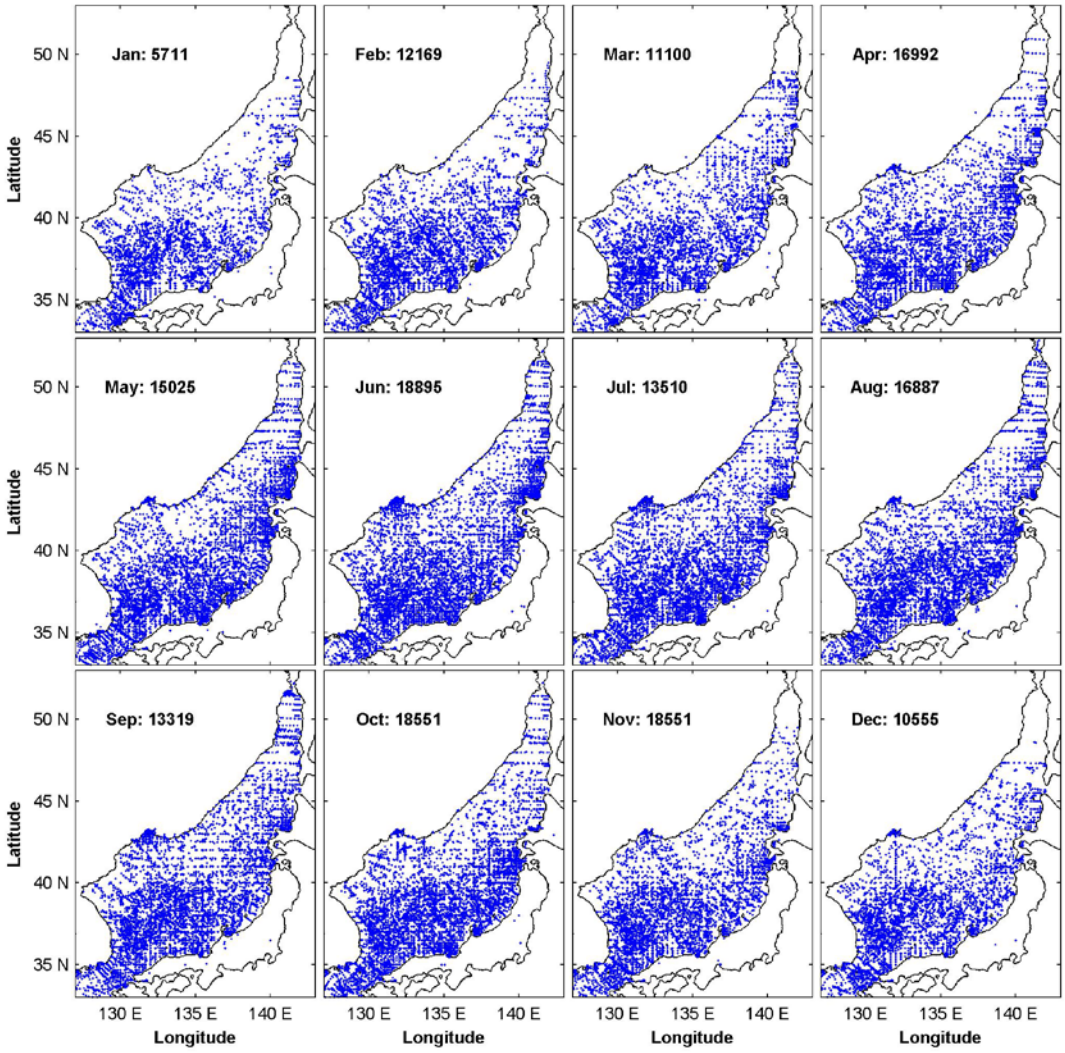

B. OPTIMAL SPECTRAL DECOMPOSITION (OSD)

The Optimal Spectral Decomposition (hereafter OSD) method is used to establish temporally varying 3-D gridded (T, S) fields from the WOD13 profiles (Chu et al., 2015),

$$\mathbf{c}_a - \mathbf{c}_b = f_n \mathbf{s}^{(K)}, \quad s_K(\mathbf{x}_n) \equiv \sum_{k=1}^{K} a_k \, \phi_k(\mathbf{x}_n) \qquad (1)$$

where the vector **c** represents (T, S), and $\{\phi_k(x_n), k = 1, 2, \ldots, K\}$ are the basis functions.

"The basis functions, depending only on the topography of the ocean basin, are the eigenvectors of the Laplacian operator with the same lateral boundary conditions as the assimilated variable anomalies" (Chu et al., 2015) (see Figure 17).

Figure 17. First Nine Basis Functions of the Surface

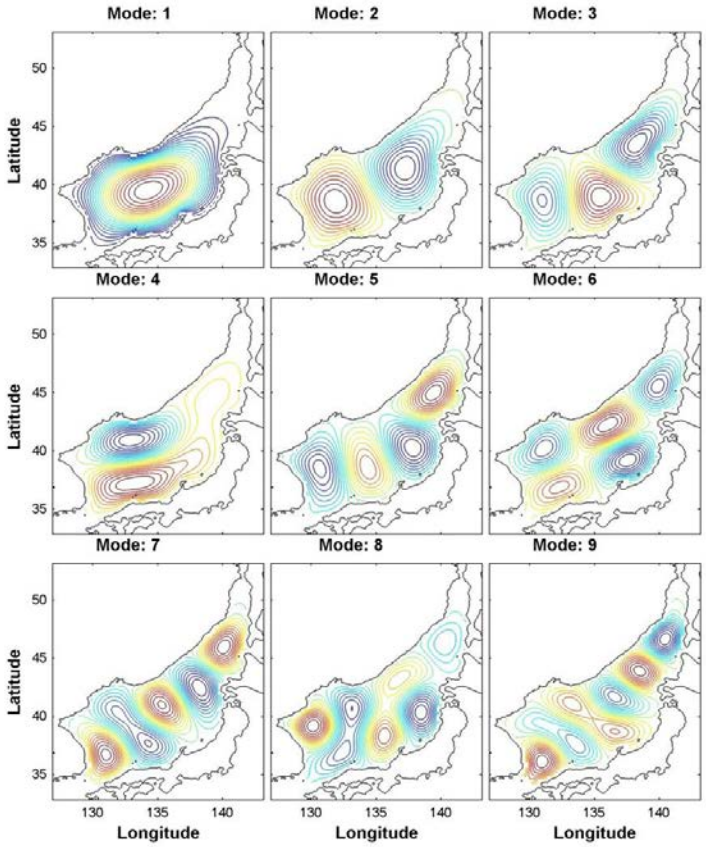

"Basis functions $\{\varnothing k(x,z)\}$ needs to satisfy three necessary conditions: (i) satisfaction of the same homogeneous boundary condition of the assimilated variable anomaly, (ii) orthonormal, and (iii) independence of the assimilated variable" (Chu et al., 2015). If K is the number of basis function (mode number of the optimal truncation) and N is the number of grid points, the orthonormal set can be shown in (2) and (3)

$$\sum_{n=1}^{N} \varnothing_k(x_n)\varnothing_{k'}(x_n) = \delta_{kk'} \qquad (2)$$

$$\delta_{kk'} = \begin{cases} 0 & if \quad k \neq k' \\ \\ 1 & if \quad k = k' \end{cases} \qquad (3)\ (\text{Chu et al., 2015})$$

Because of the "independence of the assimilated variable (the third necessary condition), the basis functions are available prior to the data assimilation" (Chu et al., 2015).

Here, x_n = (x_i, y_j), "n = 1, 2, ... , N, representing the horizontal grid points and vertical coordinate z is omitted for simplicity" then "the first K discrete basis functions for all grid points are represented by the matrix" (Chu et al., 2015) below

$$G = \{g_{nk}\} = \begin{bmatrix} \varnothing_1(x_1) & \varnothing_1(x_2) & \cdots & \varnothing_1(x_N) \\ \varnothing_2(x_1) & \varnothing_2(x_2) & \cdots & \varnothing_2(x_N) \\ \cdots & \cdots & \cdots & \cdots \\ \varnothing_k(x_1) & \varnothing_k(x_2) & \cdots & \varnothing_k(x_N) \end{bmatrix} \qquad (4)$$

Total error E can be explained in (5)

$$E = \sum_{n=1}^{N} f_n \left(\varphi(x_n) - D_n(x_n)\right)^2 \qquad (5)$$

f_n is "observational data influence at grid point" x_n. "The larger the value of" f_n , "the larger the observational influence on that grid point" (Chu et al., 2015).). f_n can be 0 if there are no observed data near the grid point or a large number if reliable observed data is very close to the grid point. Magnitude of f_n is determined according to the distance between the position of observed data and grid point. Therefore, the calculated value by utilizing f_n is more accurate than average value of observed data in the grid. f_n is the sum of h_{mn} where H = [h_{mn}] operator is an M (number of observed data) × N (number of grid points) matrix. h_{mn} denotes interpolation weight number.

$$f_n = \sum_{m=1}^{M} h_{mn}, \ \sum_{n=1}^{N} h_{mn} = 1 \qquad (6)$$

The data influence matrix "F is an N × N diagonal matrix" (Chu et al., 2015).

$$F = \begin{bmatrix} f_1 & 0 & 0 & 0 \\ 0 & f_2 & 0 & 0 \\ 0 & 0 & \ddots & 0 \\ 0 & 0 & 0 & f_N \end{bmatrix} \qquad (7)$$

D_n is "distributed N-dimensional vector on grid points. Distribution of all innovations $d^{(m)}(x^{(m)})$ (m = 1, 2, ... , M) from the observational points into the grid points is represented by the same proportionality coefficient. The mean adjustment at grid point x_n due to all the observations is given" (Chu et al., 2015) in (8).

$$D_n = \frac{\sum_{m=1}^{M} h_{mn} d^{(m)}}{f_n} \qquad (8)$$

And $\varphi(x_n)$ is represented in (9).

$$\varphi(x_n) = \sum_{k=1}^{K} a_k \varnothing_k(x_n) \qquad (9)$$

Therefore the total error E can be written again in (10).

$$E = \sum_{n=1}^{N} f_n \left(\sum_{k=1}^{K} a_k \varnothing_k(x_n) - D_n(x_n)\right)^2 \qquad (10)$$

To minimize total error, differentiation of E

$$\frac{\partial E}{\partial a_k} = \frac{\partial}{\partial a_k} \sum_{n=1}^{N} f_n \left(\sum_{k=1}^{K} a_k \varnothing_k(x_n) - D_n(x_n)\right)^2 = 0 \qquad (11)$$

"leads to a set of algebraic equations for the spectral coefficients {a_k}," (Chu et al., 2015)

$$\sum_{k=1}^{K} \left[\sum_{n=1}^{N} \varnothing_l(x_n) f_n \varnothing_k(x_n)\right] a_k = \sum_{n=1}^{N} \varnothing_l(x_n) f_n D_n \quad l=1,2,3\ldots,K \qquad (12)$$

This can be written again into a matrix form

$$GFG^T A = GFD \qquad (13)$$

"where *A* is the spectral coefficient vector" (Chu et al., 2015).

$$A = \begin{bmatrix} a_1 \\ a_2 \\ a_3 \\ \vdots \\ a_k \end{bmatrix} \qquad (14)$$

The solution of matrix form above for *A* is shown as

$$A = [GFG^T]^{-1} GFD \qquad (15)$$

Horizontal grid resolution set in this thesis 0.25° (latitude) × 0.25° (longitude).

C. P-VECTOR INVERSE METHOD FOR ABSOLUTE VELOCITY (U, V) DATA

The P-vector inverse method is used for obtaining absolute geostrophic velocity (u, v) from hydrographic data. Since "the quantities T, S are relatively easy to measure, and in contrast to velocity observations, the climatological signal in the T, S fields is less contaminated by energetic smaller-scale motions induced by eddies and waves" (Chu et al., 1998), the P-vector inverse method is useful for verifying velocity with observed temperature and salinity data. Three physical bases for the P-vector inverse method are required: "geostrophic balance, mass conservation and no major cross-isopycnal mixing except in water masses in contact with the atmosphere" (Chu et al., 1998) where ρ is the potential density,

$$\vec{V} \cdot \nabla \rho = 0 \qquad (16) \text{ (Chu et al., 1998)}$$

"represents conservation of mass and by differentiating this equation with respect to z, using the geostrophic and hydrostatic balance, and including the latitudinal variation of the Coriolis parameter, conservation of potential vorticity equation (Pedlosky, 1986) can be obtained" (Chu et al., 1998) in (17)

$$\vec{V} \cdot \nabla q = 0, \; q = f \frac{\partial \rho}{\partial z} \qquad (17) \text{ (Chu et al., 1998)}$$

Equation (17) indicates that $\vec{V}$ is perpendicular to both $\nabla\rho$ and ∇q therefore, the velocity $\vec{V}$ is parallel to $\nabla q \times \nabla p$. Since "the potential density surface does not coincide with the potential vorticity surface, $\nabla q \times \nabla p \neq 0$ is satisfied" (Chu et al., 1998). Thus, unit vector $\vec{P}$ (hereafter P-vector) which is parallel to $\vec{V}$ is obtained in (18)

$$\vec{P} = \frac{\nabla\rho \times \nabla q}{\left|\nabla\rho \times \nabla q\right|} \qquad (18) \text{ (Chu et al., 1998)}$$

The "P-vector lies on the intersection of the potential density and potential vorticity surfaces." (see Figure 18)

Figure 18. Absolute Velocity and the Intersection of Surfaces of Potential Density and Potential Vorticity

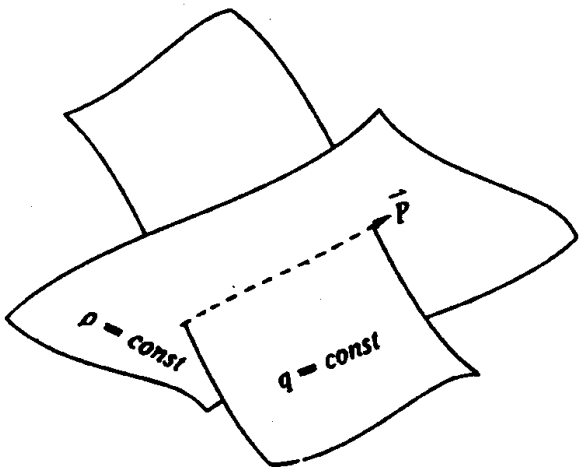

Source: Chu, P. C., C. Fan, and W. Cai, 1998: P-vector inverse method evaluated using the Modular Ocean Model (MOM). *J.Oceanogr.*, **54**, 185–198).

"The relationship between velocity, $\vec{V}$ = (u, v, w), and $\vec{P}$ =(P_x, P_y, P_z), is shown below where r is the proportionality"

$$\vec{V} = r(x, y, z)\vec{P} \qquad (19) \text{ (Chu et al., 1998)}$$

A proportionality parameter r is determined with a set of algebraic equations by "applying the thermal wind relation at two different depths z_k and z_m," (Chu et al., 2001)

$$r^{(k)}\vec{P}_x^{(k)} - r^{(m)}\vec{P}_x^{(m)} = \Delta\vec{u}_{km}$$
$$r^{(k)}\vec{P}_y^{(k)} - r^{(m)}\vec{P}_y^{(m)} = \Delta\vec{v}_{km} \qquad (20)\ (\text{Chu et al., 2001})$$

"which are two linear algebraic equations for $r^{(k)}$ and $r^{(m)}$ $[r^{(i)}=r(x, y, z_i)]$. Here"

$$(\Delta\vec{u}_{km}, \Delta\vec{v}_{km}) = \frac{g}{f\rho_0}\int_{z_m}^{z_k}\left(\frac{\partial\hat{\rho}}{\partial y}, -\frac{\partial\hat{\rho}}{\partial x}\right)dz' \qquad (21)\ (\text{Chu et al., 2001})$$

"where $\hat{\rho}$ is the in situ water density, and ρ_0 is the characteristic value of the density. There are N-1 sets (m = 1, 2, k-1, k+1, . . . , N) for calculating $r_{(k)}$. Here N is the total number of vertical levels of the water column. All the N-1 sets of equations are compatible under the thermal wind constraint and should provide the same solution. However, because of errors in measurements (instrumentation errors) and computations (truncation errors), the parameters $r_{(k)}$ may vary with m. A least squares error algorithm is used to minimize the error." (Chu et al., 2001)

Thus, "absolute velocity at any level m" (Chu et al., 1998) can be obtained when the absolute velocity $(\vec{u}^{(k)}, \vec{v}^{(k)})$ is known,

$$\hat{\vec{u}}^{(m)} = \vec{u}^{(k)} + \Delta\vec{u}_{mk}$$
$$\hat{\vec{v}}^{(m)} = \vec{v}^{(k)} + \Delta\vec{v}_{mk} \qquad (22)\ (\text{Chu et al., 1998})$$

and error E_m at level m is in (23).

$$E_m = \left|V^{(m)}\vec{P}^{(m)} - \hat{\vec{V}}^{(m)}\right| = 2\sin\left[\frac{1}{2}(\vec{P}^{(m)}, \hat{\vec{V}}^{(m)})\right] \simeq V^{(m)}\sin(\vec{P}^{(m)}, \hat{\vec{V}}^{(m)}) \qquad (23)\ (\text{Chu et al., 1998})$$

The absolute velocity $(\vec{u}^{(k)}, \vec{v}^{(k)})$ would be determined by minimizing error in (24)

$$\frac{\partial E}{\partial\vec{u}^{(k)}} = 0, \frac{\partial E}{\partial\vec{v}^{(k)}} = 0 \qquad (24)\ (\text{Chu et al., 1998})$$

D. EMPIRICAL ORTHOGONAL FUNCTION (EOF) ANALYSIS

The Empirical Orthogonal Function (hereafter EOF) analysis,

> first introduced to geophysics by Lorenz in 1956, has subsequently been used to enable analysis of data with complex spatial/temporal structures. Using this method, the most efficient decomposition of the data into representative modes is determined by empirically finding the eigenfunctions that best describe the information. Retention of only the first few modes can contain a significant allocation of the total variance and each mode contains phenomena with differing spatial/temporal scales and so can be confined. (Kaihatu et al., 1998)

Therefore, it is applied to the anomaly data relative to the climatological mean. Since the present paper analyzes 54 years of long-term data, it is not simple to research and compare long-term variation. EOF analysis allows for easier identification of particular anomalies.

For thermal variability, temperature anomaly field $\hat{T}$ can be explained as a product of monthly mean $\overline{T}$ subtraction from temperature data set *T*.

$$\hat{T}\left(x_i, y_j, z_k, \tau_l, t_m\right) = T\left(x_i, y_j, z_k, \tau_l, t_m\right) - \overline{T}\left(x_i, y_j, z_k, t_m\right) \qquad (25)\ \text{(Chu, 2006)}$$

$\hat{T}$ is arranged into a N×P matrix $\hat{T}\left(r_n, \tilde{t}_p\right)$. N is corresponding number of grids and P "is the total number of the time points used for computing the covariance matrix." In this thesis, 54years × 12month = 648 was used for P. N is depends on the area and depth boundary thus varies according to established depth layers in this thesis. This processes "separates the data sets into eigenmodes and each mode has an associated variance, a dimensional time series and a non-dimensional" spatial pattern (Chu et al., 1997) (see Figure 19).

In $\hat{T}\left(r_n, \tilde{t}_p\right)$, spatial covariance matrix can be calculated as (26)

$$R = \begin{bmatrix} R_{11} & R_{12} & \cdots & R_{1N} \\ R_{21} & R_{22} & \cdots & R_{2N} \\ \cdots & \cdots & \cdots & \cdots \\ R_{N1} & R_{N2} & \cdots & R_{NN} \end{bmatrix},\ R_{mn} = \sqrt{\frac{1}{P}\sum_{P}\hat{T}\left(r_n, \tilde{t}_p\right)\hat{T}\left(r_m, \tilde{t}_p\right)} \qquad (26)$$

where n and m represent grid points. This symmetric matrix has eigenvalues λ_α and eigenvectors Φ_α as (27).

$$\sum_{j=1}^{N} R_{ij}\Phi_\alpha(r_i) = \lambda_\alpha \Phi_\alpha(r_i),\ \text{i=1,2,…N} \qquad (27)$$

Figure 19. Freshwater Content in 200m ~ 400m Depth of the ES

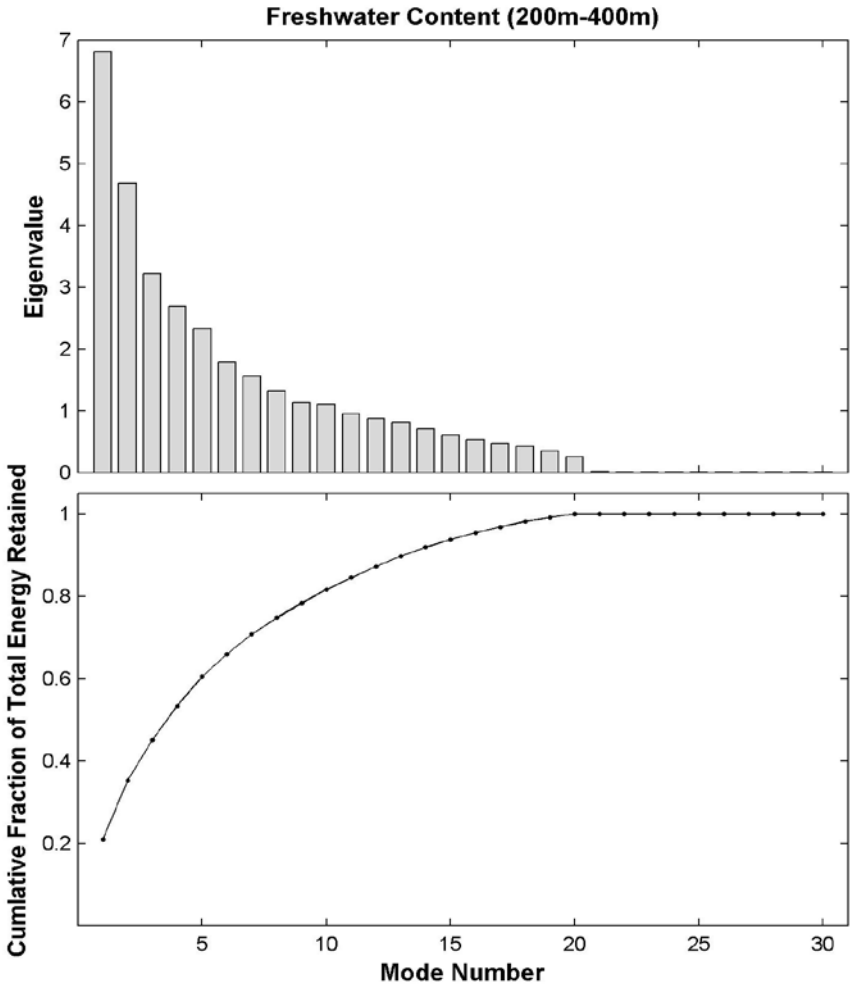

(Above) Eigenvalues of freshwater content in 200m shown in decreasing order pattern. (Below) First few modes account for most of the total variance. In this figure, the first 5 modes explain approximately 60% of the total variance.

The eigenvectors are called EOFs, which have "non-seasonal variation temperature anomaly pattern. The eigenvalues are all positive and the sum of all

eigenvalues equals the total variance. Therefore, λ_α is considered as the portion of total variance 'explained' by the EOF Φ_α. It is favorable to label the eigenfunctions Φ_α so that the eigenvalues are in decreasing order" (Chu et al., 1997).

Singular value decomposition (SVD) is used for factorizing N×P matrix $\hat{T}\left(r_n, \tilde{t}_p\right)$. svd($\hat{T}$) = [U×S×V] produces a diagonal matrix S, of the dimension as $\hat{T}$ and with nonnegative diagonal elements in decreasing order, and unitary matrices U and V so that $\hat{T}$ = U×S×V. Thus, $\hat{T}\left(r_n, \tilde{t}_p\right)$ is written again as (28)

$$\hat{T}\left(r_n, \tilde{t}_p\right) = \sum_\alpha PC_\alpha\left(\tau_l, t_m\right)\Phi_\alpha\left(x_i, y_j, z_k\right) \qquad (28)$$

This equation makes it easy to separate temporal and spatial parts. U × S in (28), is the principal component, which $PC_\alpha\left(\tau_l, t_m\right)$ represents temporal variation. V in equation is EOF $\Phi_\alpha\left(x_i, y_j, z_k\right)$, which represents associated spatial variation. $PC_\alpha\left(\tau_l, t_m\right)$ can be plotted in time series form to recognize temporal anomalies.

The first few modes can account for most of the total variance. The percentage of variance may differ due to layer and variable settings, but still the first few modes cover approximately 50 ~ 70% of variance in each variable. Therefore, the first five modes were used in this thesis to plot spatial variation.

THIS PAGE INTENTIONALLY LEFT BLANK

IV. SEASONAL VARIABILITY

A. TEMPERATURE FIELD

Figure 20 clearly proves the water mass depth layer set up. From the surface to 200m depth, temperature drops drastically.

Figure 20. Total Mean Temperature (^{O}C) at Different Depths

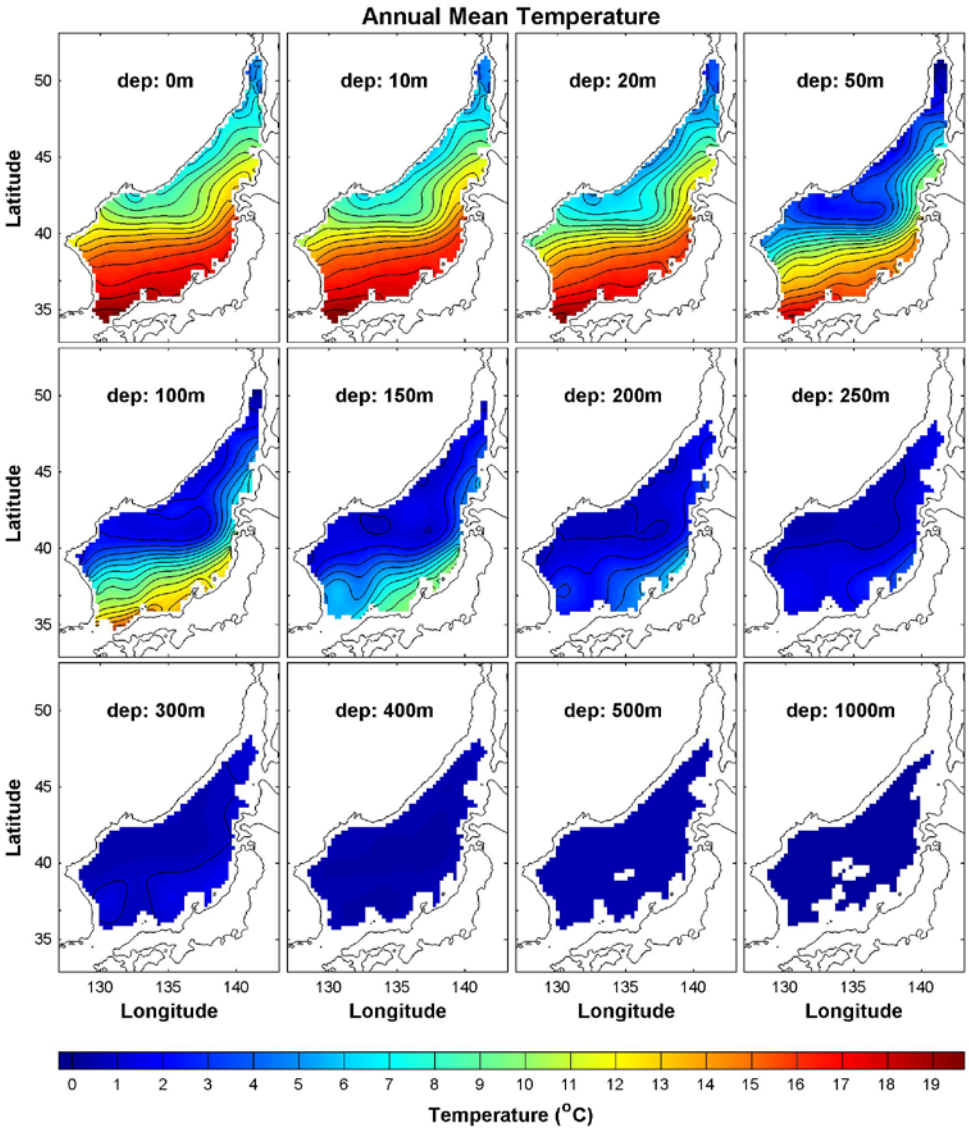

There is a difference between the northern and southern part of the SPF but an obvious temperature drop is observed in the entire ES. There is a lesser temperature drop between 200m and 400m depth, and an almost homogeneous temperature is observed from 400m depth to the bottom.

Figure 21. Climatological Monthly Mean Temperature at the Surface

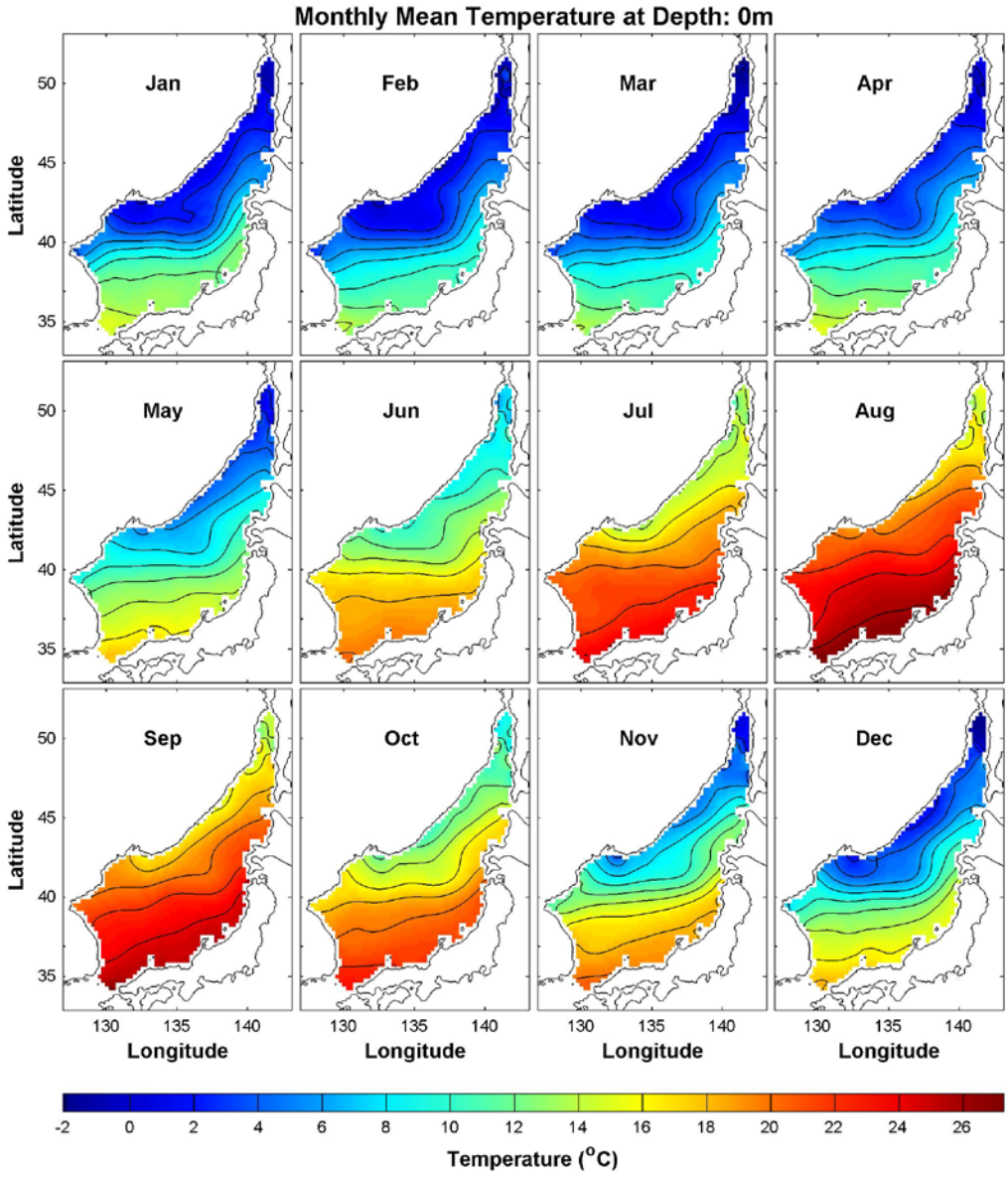

Seasonal differences are very significant in the surface layer (see Figure 21). The SPF is clearer from October to June than from July to September. Seasonal wind characteristics of the winter reach a peak in January, and seasonal wind characteristics of summer reach a peak in June (see Figure 8). However, the monthly mean temperature of sea surface, which is very strongly influenced by seasonal wind, shows a delay of the SST peak. The coldest SST is shown in February, which is a one-month delay after winter wind peak in January, and the warmest SST is shown in August, which is a two-month delay after the summer wind peak in June. These SST peak months are matched to monthly mean SST data from 1930 to 1997 reported by Chu et al. (2001). The summer SST peak of 54 years mean matches with the SST monthly mean for the 21 years plotted by the KHOA (see Figure 11), but the winter SST peak plotted by the KHOA appears in January with no delay after the winter wind peak.

A monthly temperature difference at 200m depth is rarely observed (see Figure 22). A regional pattern at this depth is very clear on the north and south halves of the SPF. Cold water less than 1°C stays in the northern half, while the southern half has an eddy in the UB and warm water flows along the northwest coast off Honshu. This warm eddy in the UB is called the Ulleung Warm Eddy. The Ulleung Warm Eddy is found in the vicinity of Ulleungdo and Dokdo (islands off the Korean coast).

> Areas around Dokdo are controlled by warm water in general because the polar fronts appear in the north of Ulleungdo except when the East Sea Warm Current is not formed. The polar front varies a lot in terms of its shape and pattern, such that it can regulate the current patterns around Dokdo even though the front itself is to the north. This meandering creates eddies, both clockwise and counter-clockwise, and eddies are one of the most important oceanographic factors that determine the local oceanic conditions. Eddies appear in various sizes, with a diameter up to hundreds of kilometers. Monitoring of currents around Dokdo showed that a warm eddy near Ulleungdo recirculates the warm current toward the southwest. This Ulleung Warm Eddy maintains a clockwise direction and affects seawater hundreds of meters deep. Relatively small cold water eddies are also observed. (Korea National Geographic Information Institute Dokdo Jirinet, 2015: [Available online at http://www.ngii.go.kr/dokdoen/contents/contentsView.do?rbsIdx=54#none])

Figure 22. Climatological Monthly Mean Temperature at 200m Depth

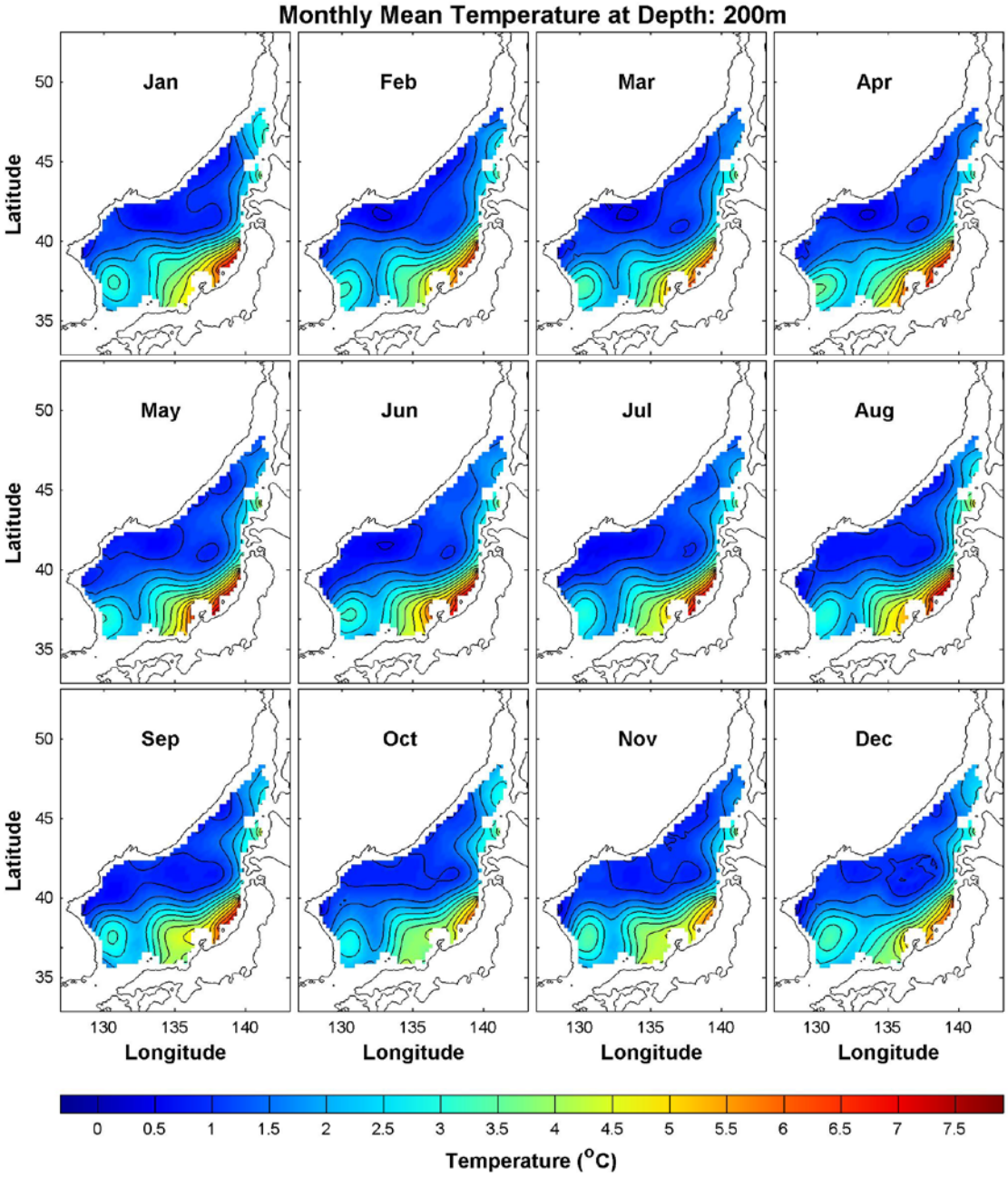

According to 54 years of monthly mean temperature profile, Ulleung Warm Eddy is clearly distinguished from 200m depth to 300m depth in every month.

Temperature field in deep layer is almost homogeneous. At 400m depth, warmer water forms along the coastline and colder water in major basins (see Figure 23). Colder water in basins enlarged in summer and shrunk in winter. Relatively warm water found

near Tatar Strait from December to April next year. At 1,000m depth, seasonal difference is rarely found and temperature is almost homogeneous (see Figure 24).

Figure 23. Climatological Monthly Mean Temperature at 400m Depth

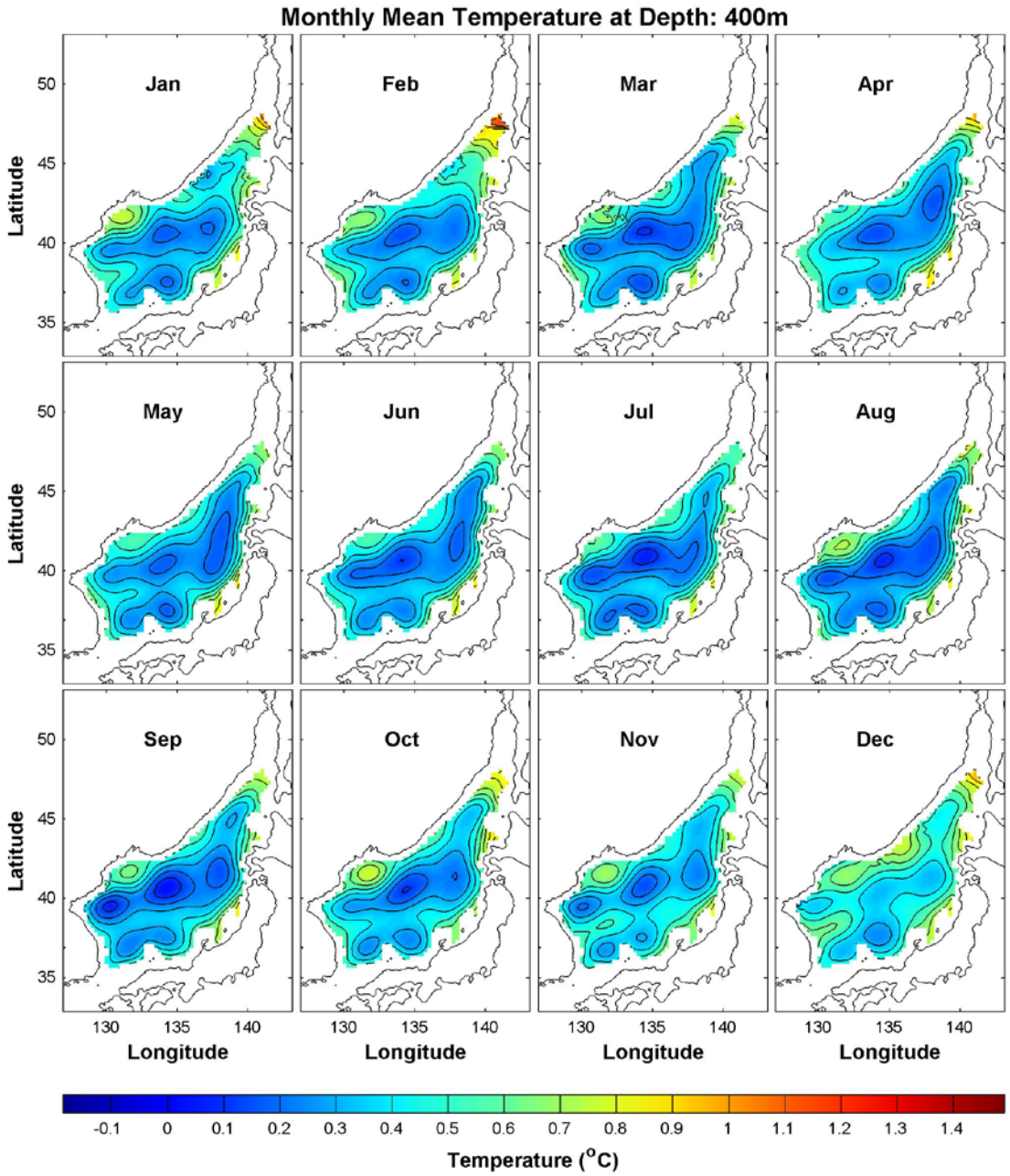

Figure 24. Climatological Monthly Mean Temperature at 1,000m Depth

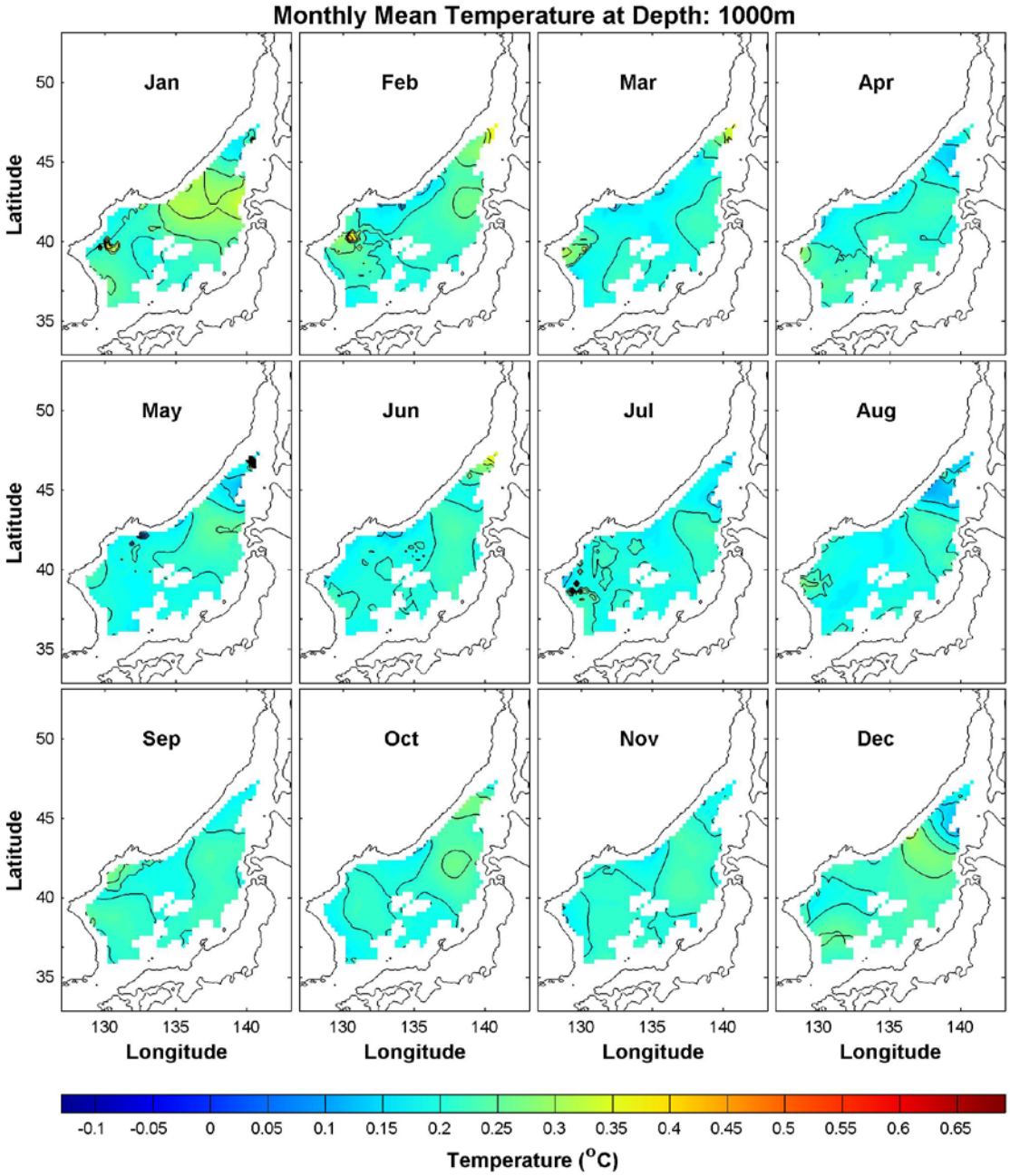

B. SALINITY FIELD

Relatively very fresh water appears near the Tatar Strait and very saline water inflow through the Korea Strait is observed from surface to 100m depth (see Figure 25). The salinity field below 200m depth appears almost homogenous, but this is due to range separation of the whole water column. The salinity distribution of the deeper layer is explained in Figure 28 and 29.

Figure 25. Total Mean Salinity (psu) at Different Depths

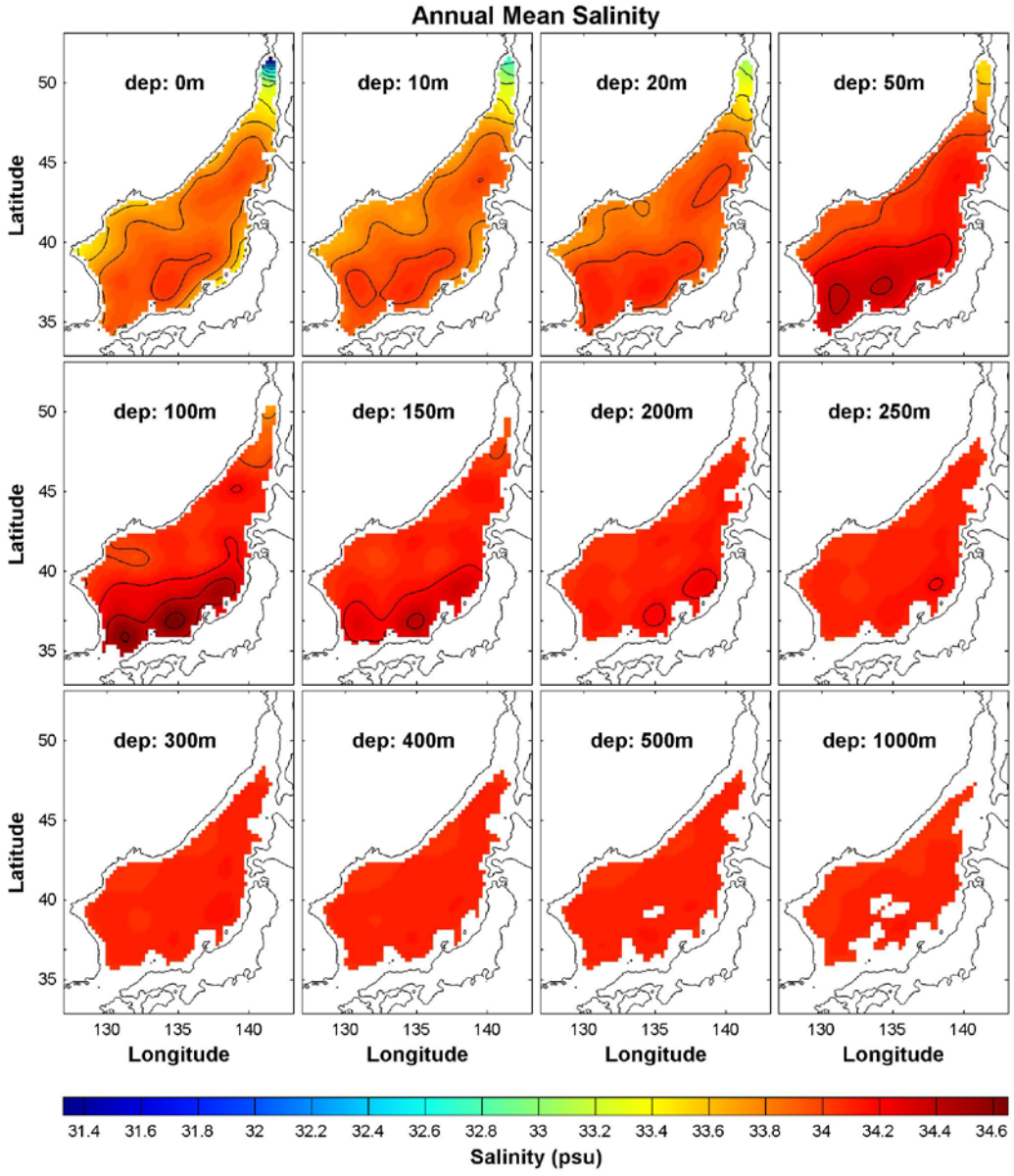

Similar to temperature distribution, salinity is higher in southern region and lower in northern region due to saline TWC inflow through the Korea Strait (see Figure 26). But two different distribution patterns are observed. Salinity is higher from January to June than from July to December and lower salinity is observed near Korea Strait and off Korean peninsula in August and September.

Figure 26. Climatological Monthly Mean Salinity (psu) at the Surface

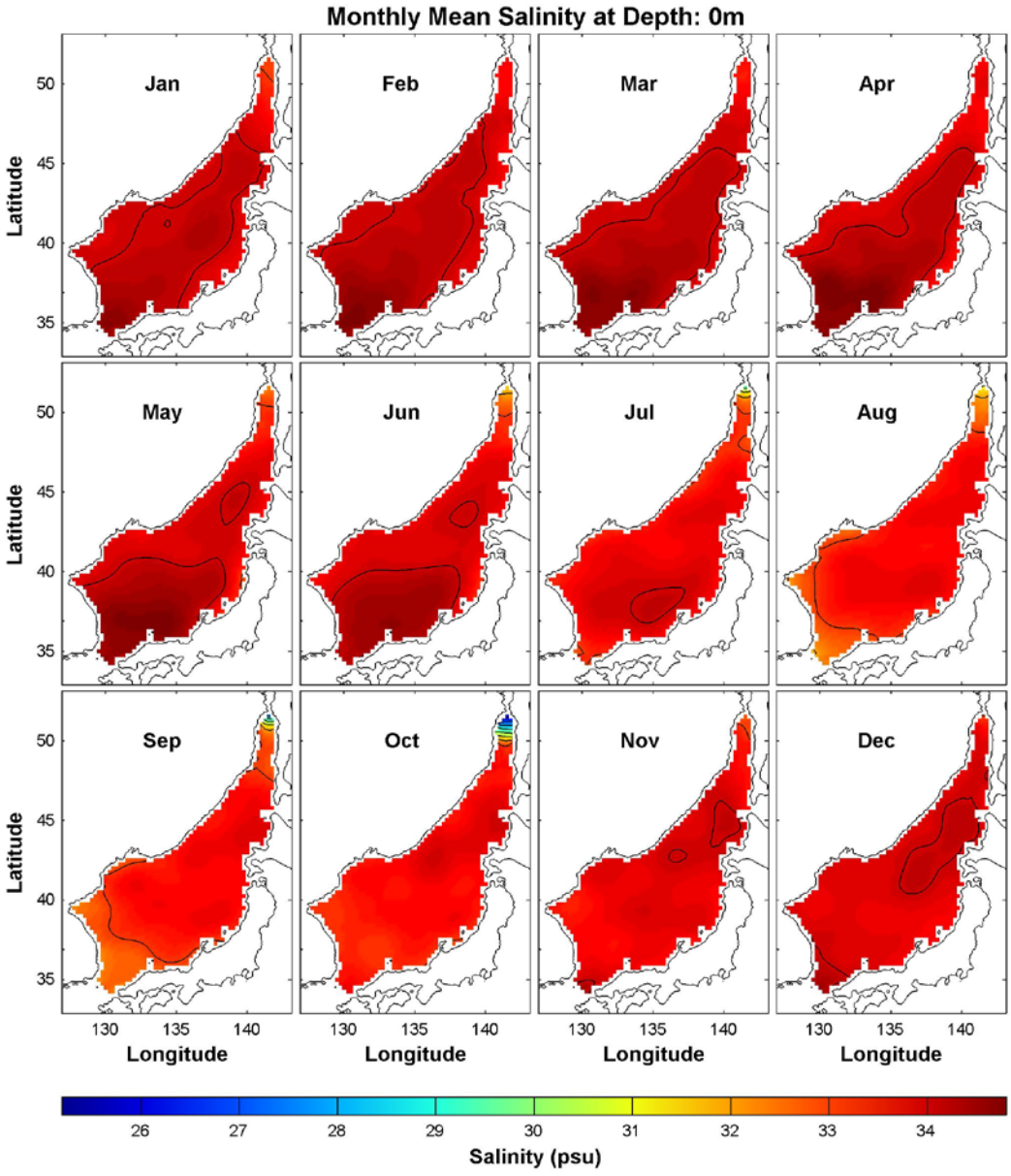

Salinity in surface layer of the ES is influenced by the discharge of the TWC and Chinese coastal waters (National Geographic Information Institute, 2015: The Geography of Dokdo. Accessed 10 December 2015. [Available online at http://www.ngii.go.kr/dokdoen/contents/contentsView.do?rbsIdx=54#none]). Therefore, salinity in surface layer is highly affected by Changjiang river runoff to the East China Sea. The report by Tada et al. also showed "salinity change may have been caused by changes in the discharge rate to the East China Sea (hereafter ECS) of the Changjiang River." (Tada et al., 1999) Changjiang is the longest river in Asia (The World Delta Database 2015: Yangtze River delta, China, Asia. Accessed 10 December 2015. [Available online at http://www.geol.lsu.edu/WDD/ASIAN/YangtzeKiang/yankze.htm]) and it flows into the ECS with maximum discharge in summer, which subsequently extends to the south along the coast of China. This migrated Changjiang water enters the Korea Strait (Beardsley et al., 1985). Thus, the TWC through the Korea Strait becomes less saline in summer.

Inflow through the Tatar Strait is very limited, even negligible, because it is narrow (about 10km) and shallow (about 10m) (Chang et al., 2015) but low salinity near Tatar Strait is strongly related to the freshwater input from Amur River (TALLEY et al., 2006). The Amur River flows through Manchuria and eventually into the Tatar Strait. The discharge of the Amur River has two peak months in a year, May (spring) and September (autumn) (Tachibana et al., 2008). However, a two-month delay after the May peak in July and one-month delay after September peak in October are shown in monthly mean of 54 years, and October has the lowest salinity. Therefore, the September discharge peak is much greater than the May discharge peak.

At 200m depth, relatively higher salinity water flows along the west coast of Honshu just like the warm water at same depth (see Figure 27). With temperature distribution in this region, the TWC route is clearly proved by salinity distribution at 200m depth. However, the difference is not very significant, approximately 1%. The saline water distribution along the west coast of Honshu is also shown at 400m depth, and salinity in summer is higher than in winter (see Figure 28). Freshwater near the Tatar Strait is observed at 400m depth. Again this variation is noticed by range color bar, but

the difference is very small, approximately 0.5%. Almost homogeneous salinity with no seasonal variability was found at 1,000m depth (see Figure 29).

Figure 27. Climatological Monthly Mean Salinity (psu) at 200m Depth

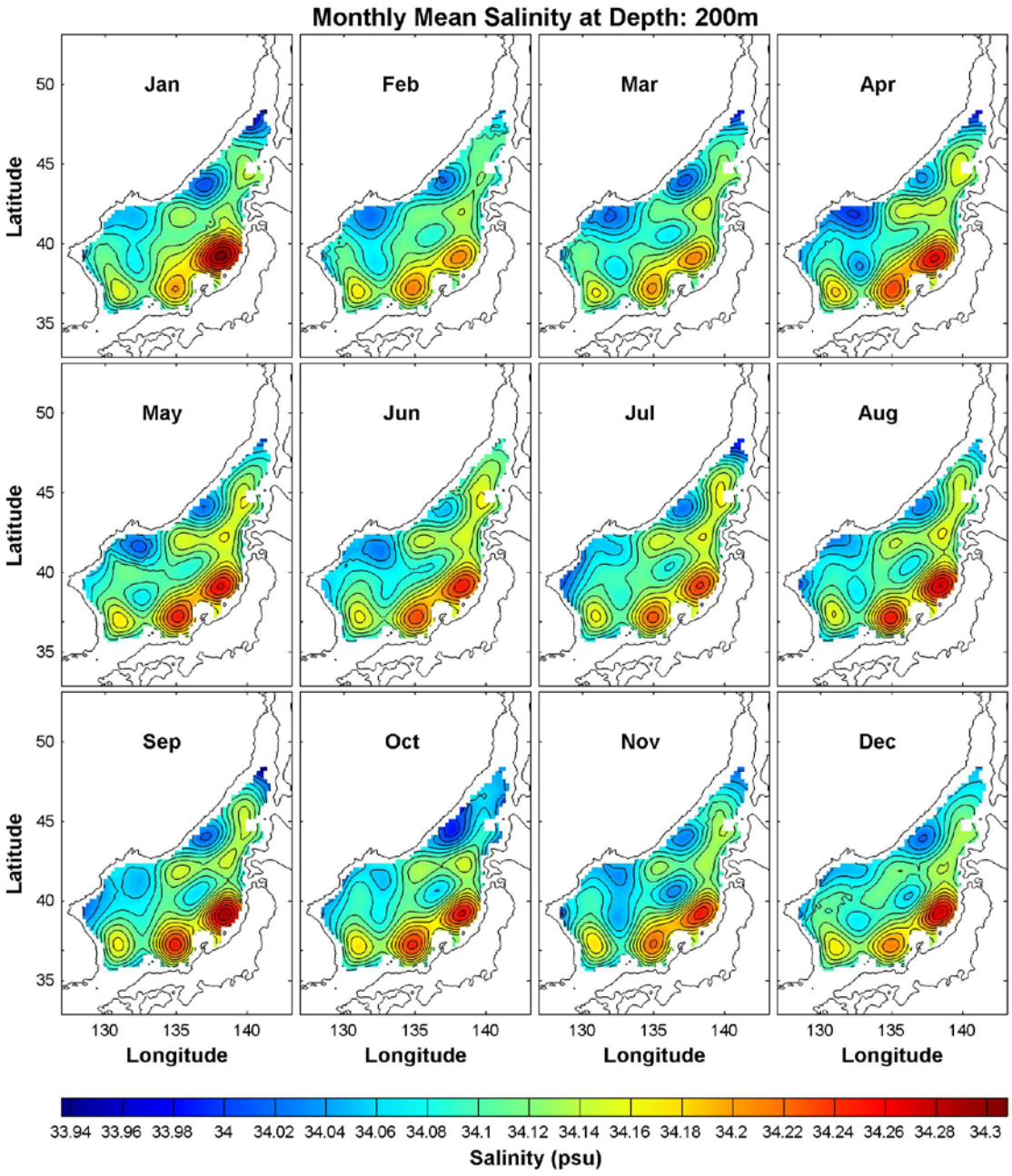

Figure 28. Climatological Monthly Mean Salinity (psu) at 400m Depth

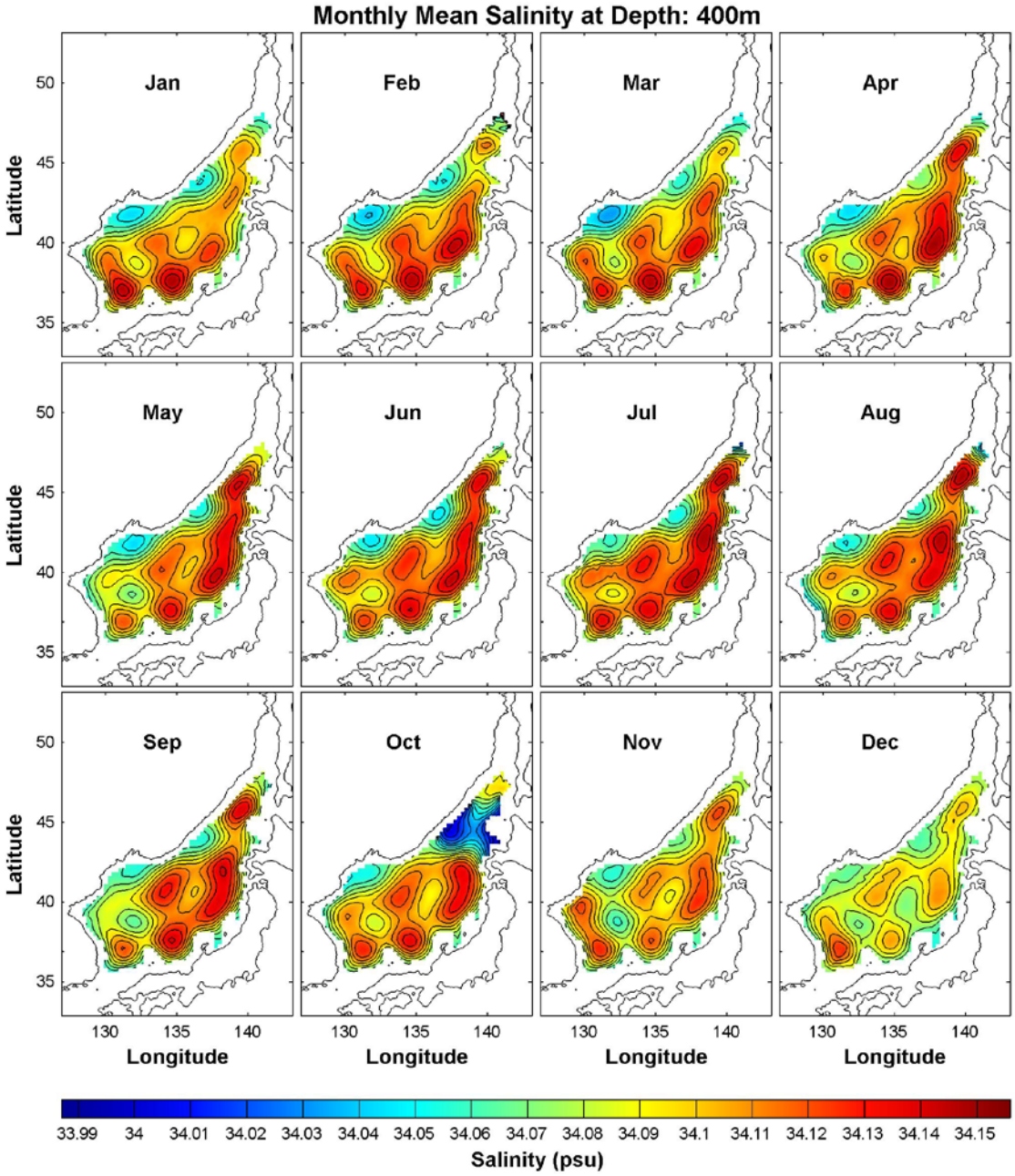

Figure 29. Climatological Monthly Mean Salinity (psu) at 1,000m Depth

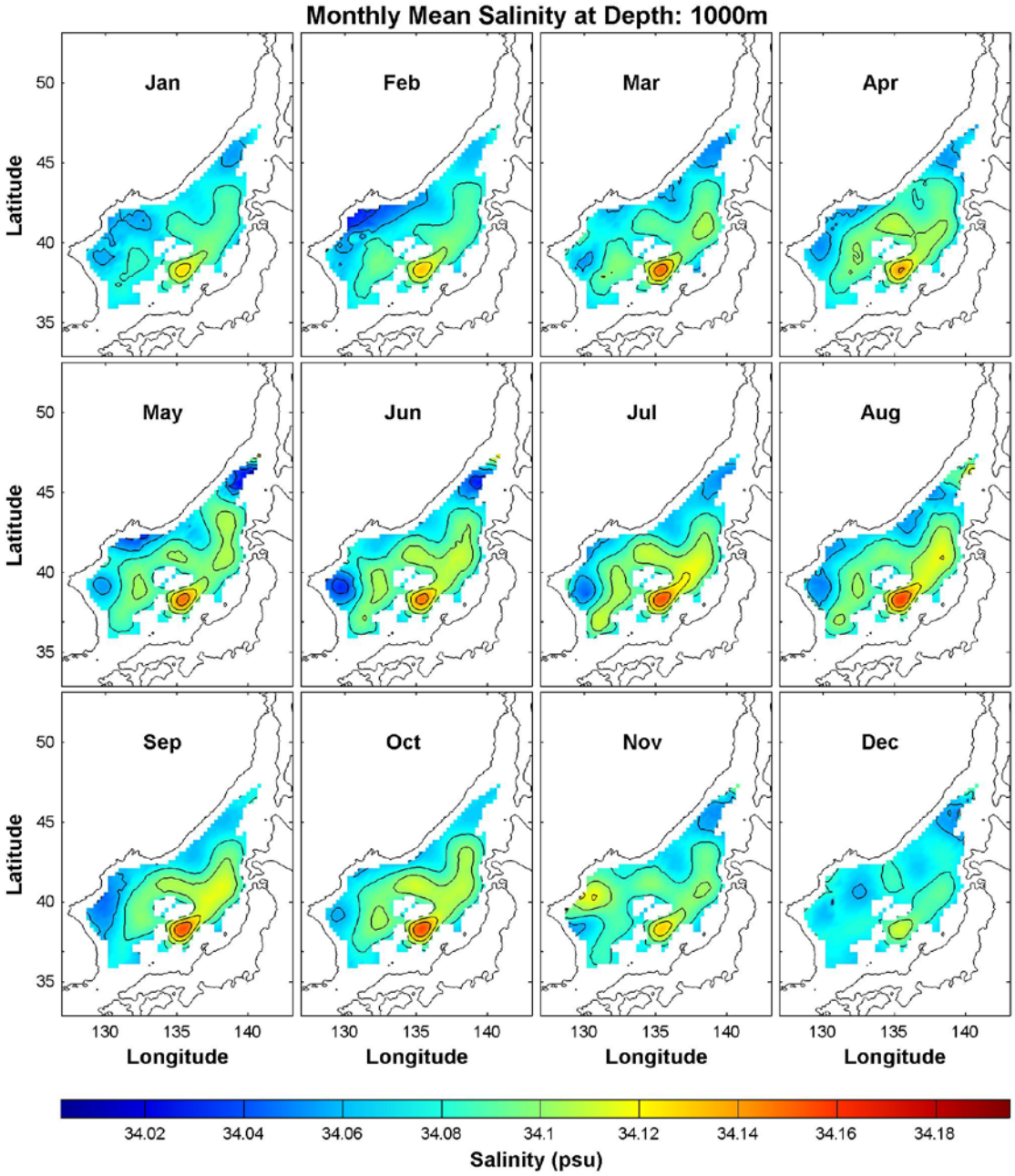

C. ABSOLUTE GEOSTROPHIC VELOCITY FIELD

Absolute geostrophic velocity (u, v) was calculated by utilizing P-vector inverse method. Water speed is higher in the surface layer and decreases by depth (see Figure 30). Inflow through the Korea Strait is shown in the surface layer. Since the Korea Strait is shallow, no significant inflow current was found in intermediate and deep layer.

Figure 30. Total Mean Absolute Geostrophic Velocity (cm/s) at Various Depths Calculated from the (T, S) Data Using the P-Vector Method

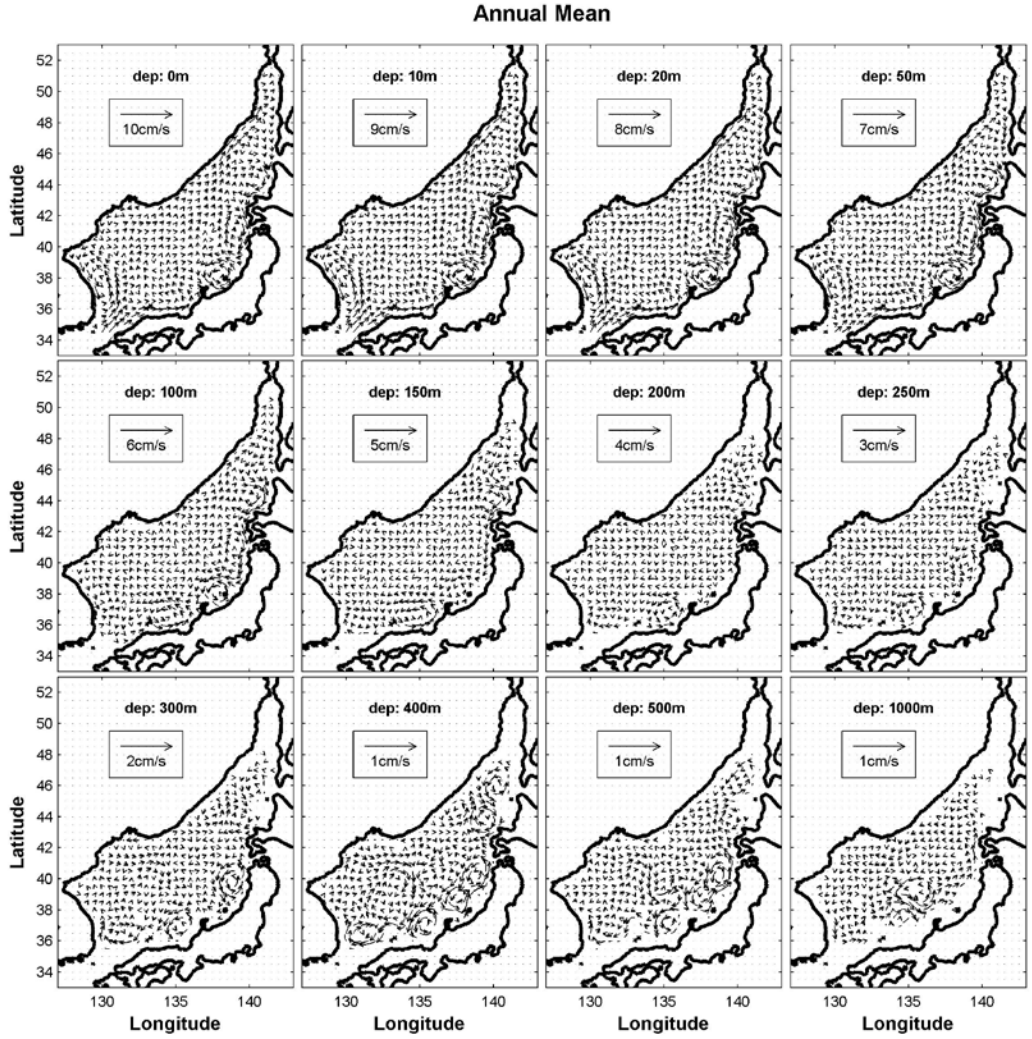

A stronger current through the Korea Strait is observed in summer, which may be related to Changjiang discharge peak causing a sea level rise of the ECS, since the TWC is basically driven by the sea level difference between the ECS and the ES (Watanabe et al., 2006) (see Figure 31).

Figure 31. Climatological Monthly Mean Absolute Geostrophic Velocity (cm/s) at the Surface Calculated from the (T, S) Data Using the P-vector Method

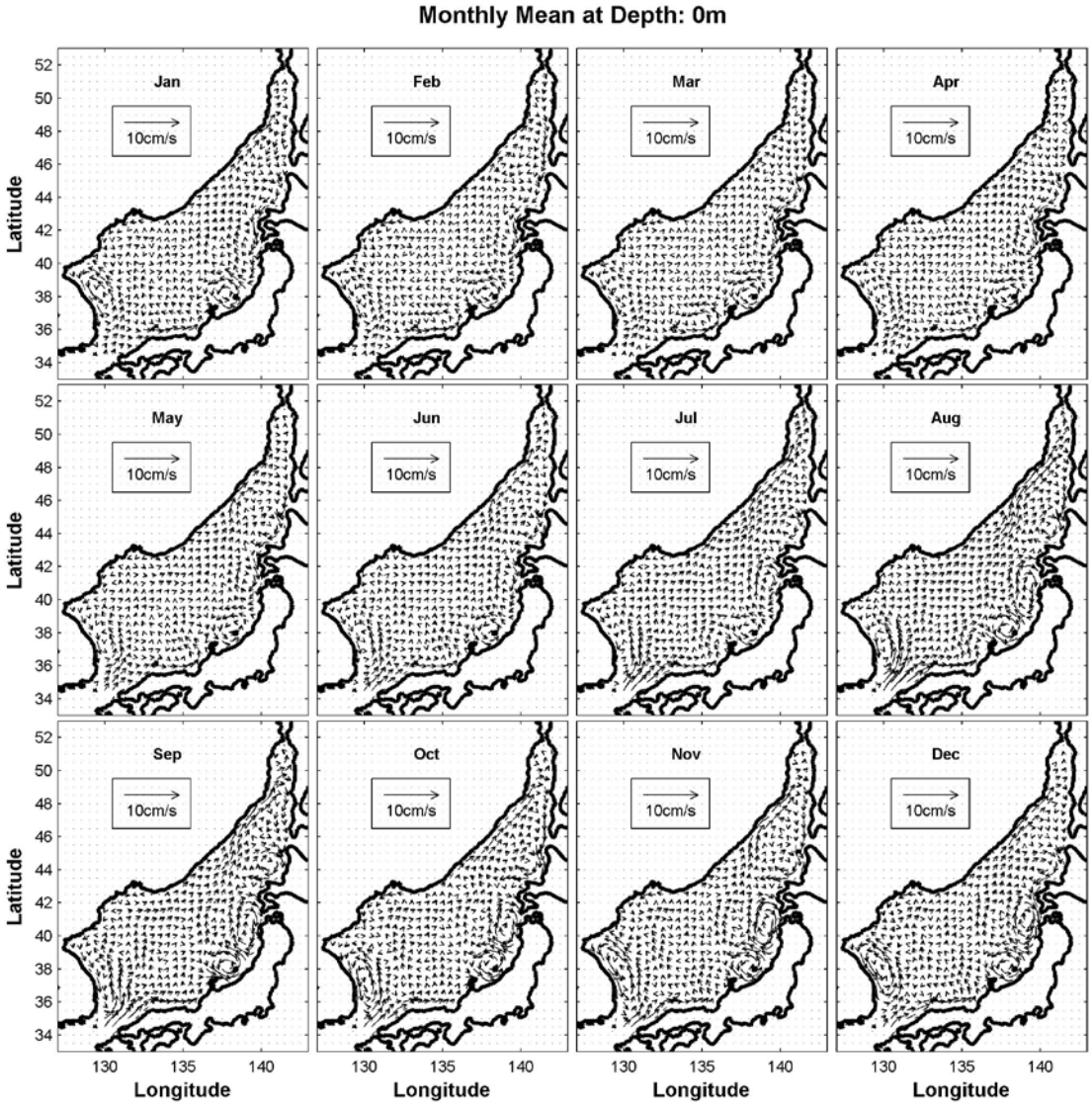

Southward NKCC observed along the northeastern coast of Korea. It became stronger in winter, and thus reaches further south than in summer (Woo-Seok and Watts, 2012). According to monthly mean absolute geostrophic velocity, the NKCC reaches its southernmost point in November and subsequently retreats back to the north.

Circulation patterns are found around the Noto Peninsula (37.2°N 137°E, in the center of the west coast of Honshu) in both the surface and intermediate layers year-round. Due to the complex topography of the continental slope to the north of the Noto Peninsula (Bogdanov, 1984), the topographic affect may cause these circulation patterns.

Figure 32. Climatological Monthly Mean Absolute Geostrophic Velocity (cm/s) at z = 200m Calculated from the (T, S) Data Using the P-Vector Method

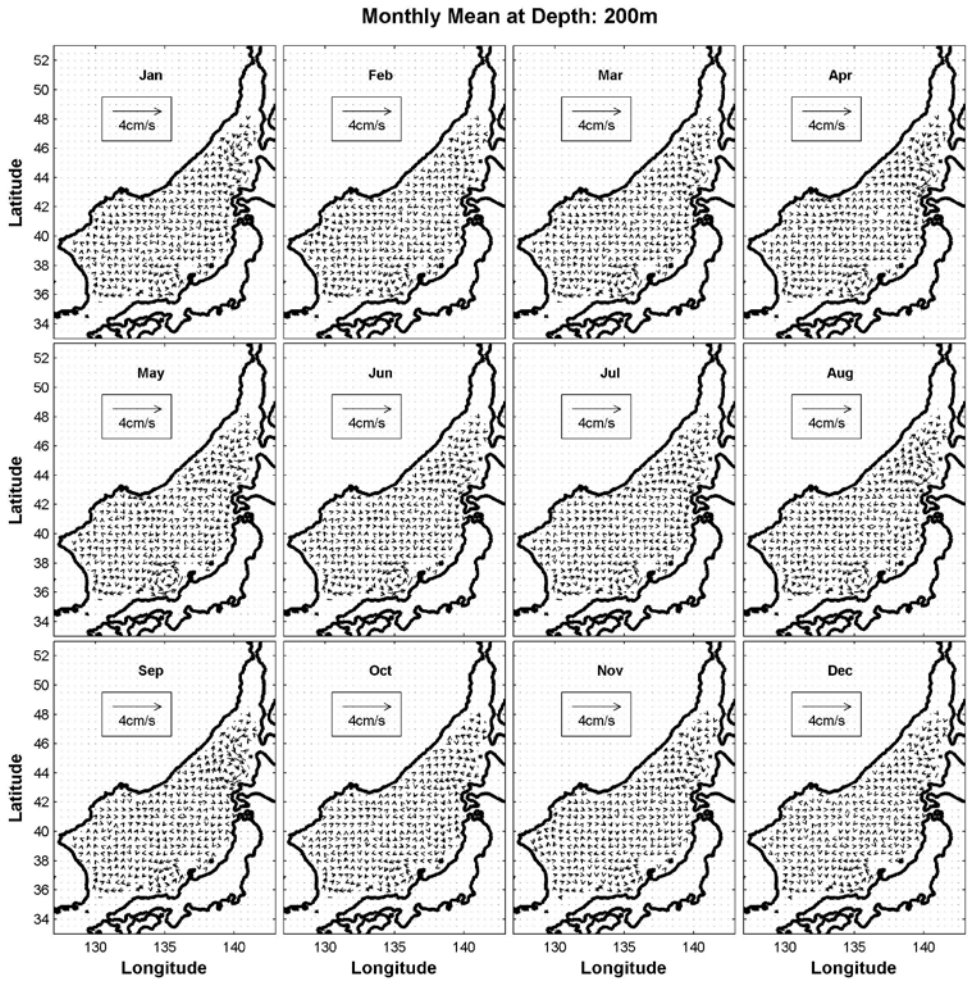

A clockwise pattern in the UB is also observed from 200m to 500m depth year-round (see Figure 32 and 33). The position of this anticyclonic circulation matches with the position of the Ulleung Warm Eddy. Therefore, the clockwise characteristic of the Ulleung Warm Eddy could be learned from the absolute geostrophic velocity field of the intermediate layer.

Figure 33. Climatological Monthly Mean Absolute Geostrophic Velocity (cm/s) at z = 400m Calculated from the (T, S) Data Using the P-Vector Method

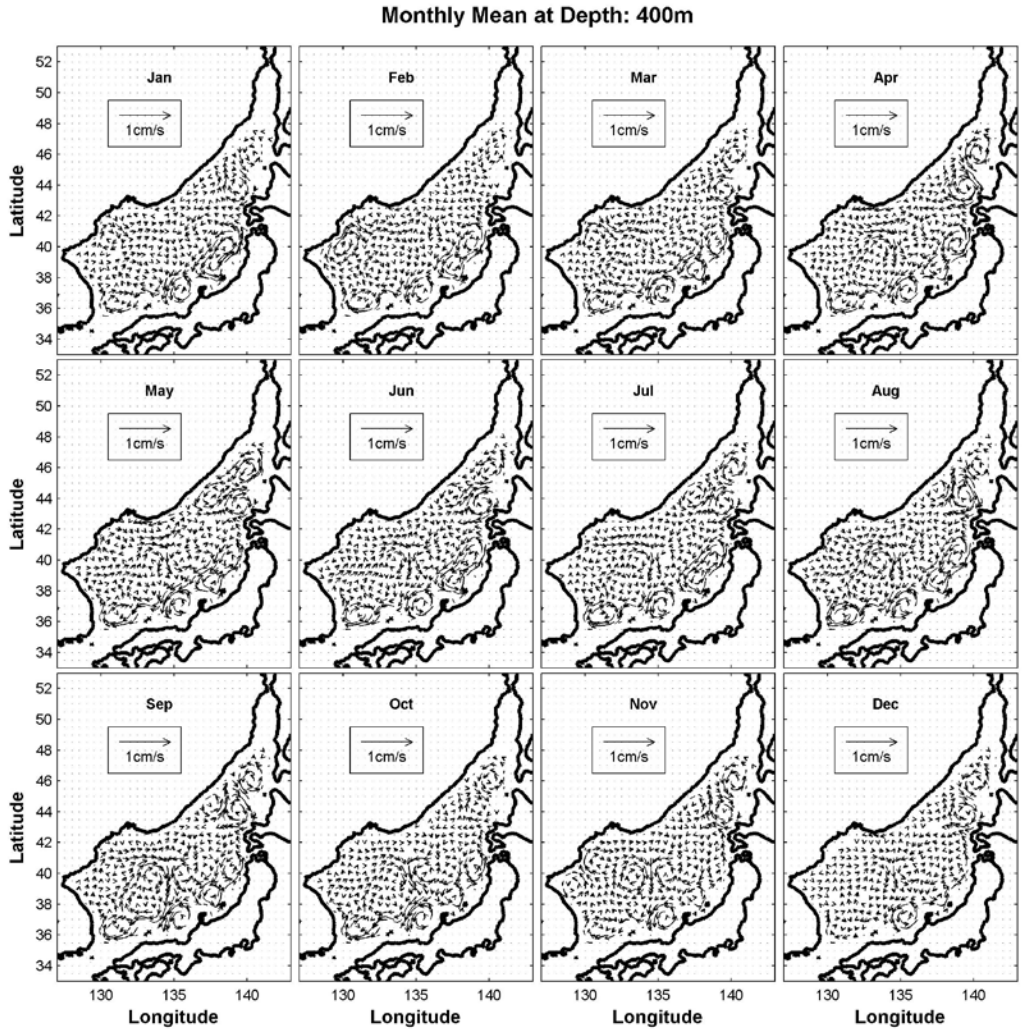

Opposite from the intermediate layer, cyclonic circulation in the UB is found in 1,000m depth (see Figure 34). According to previous research, this circulation may be related to mass transfer between basins in the ES. Deep water's formation in the JB and subsequent inflow to the UB were reported by the trajectory data of ARGO floats (Park et al., 2004b) and a current meter mooring (Senjyu et al., 2005). This deep water flows through the Ulleung Interplain Gap (hereafter UIG) between the Ulleungdo and Dokdo along the western side of the UB and generates cyclonic pattern. "Park et al. (2004) have argued that the flow through is part of an anticyclonic circulation over the Korea Plateau, but Senjyu et al. (2005) have argued that the flow through the UIG joins the flow along the eastern coast of Korea and circulates in the basin cyclonically." (Park et al., 2010) By Senjyu's argument, the flow direction matches with the absolute geostrophic velocity field at 1,000m depth of this thesis. Since the "full report on the structure of the flow has not been given yet" (Park et al., 2010), however, more research is needed to determine flow direction in this area. At this depth, water from the UB to the YB forms a cyclonic pattern and is stronger and bigger from spring to fall, weaker and smaller in winter.

Figure 34. Climatological Monthly Mean Absolute Geostrophic Velocity (cm/s) at z = 1,000m Calculated from the (T, S) Data Using the P-Vector Method

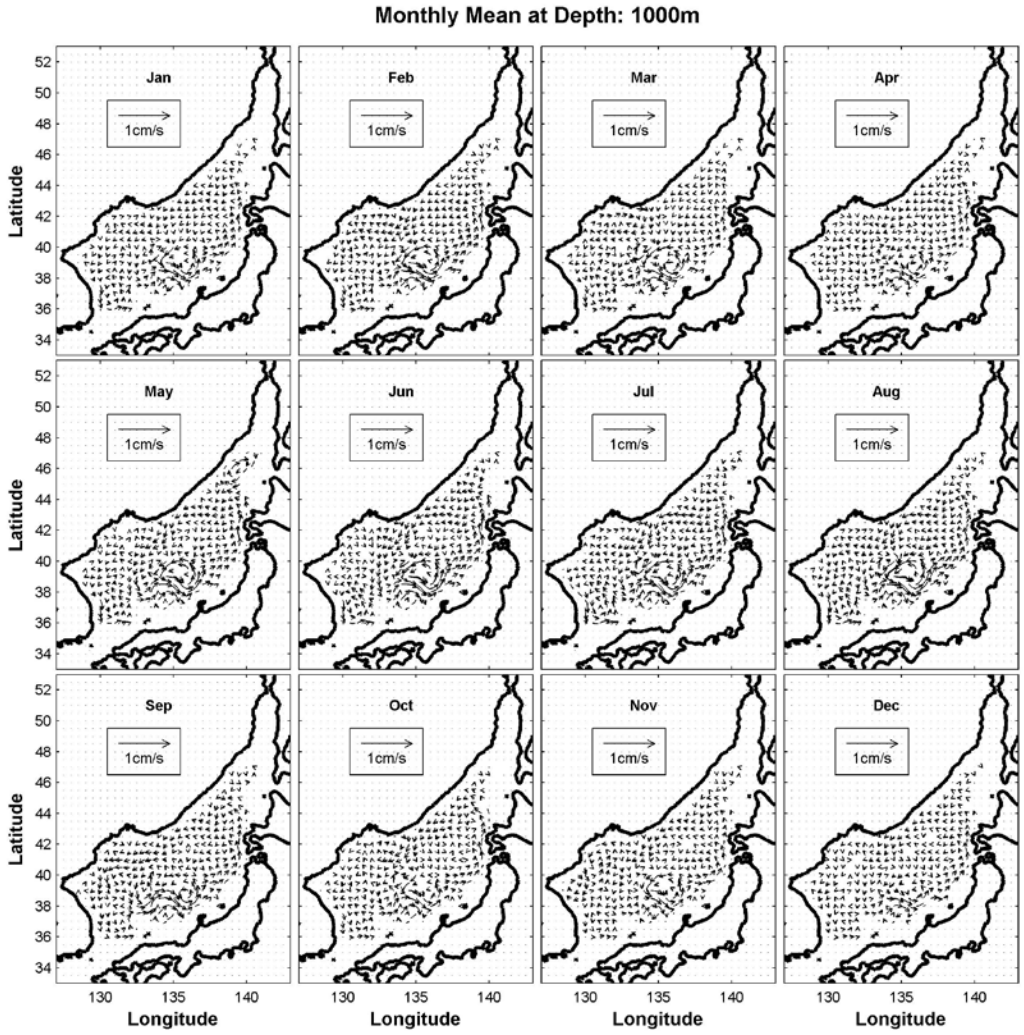

D. HEAT CONTENT

Heat content represents the heat stored in sea water. Heat content was calculated in each layer by (29).

$$HC = \int_{-h_2}^{-h_1} \rho c T dz \qquad (29)$$

which is decomposed into climatological monthly mean and anomaly (representing inter-annual variability) HC. Heat content in surface layer clearly shows seasonal variability. The surface layer retains heat from June to December and loses heat from January to May (see Figure 35).

Figure 35. Monthly Variability of Heat Content (J/m^2) in Surface Layer

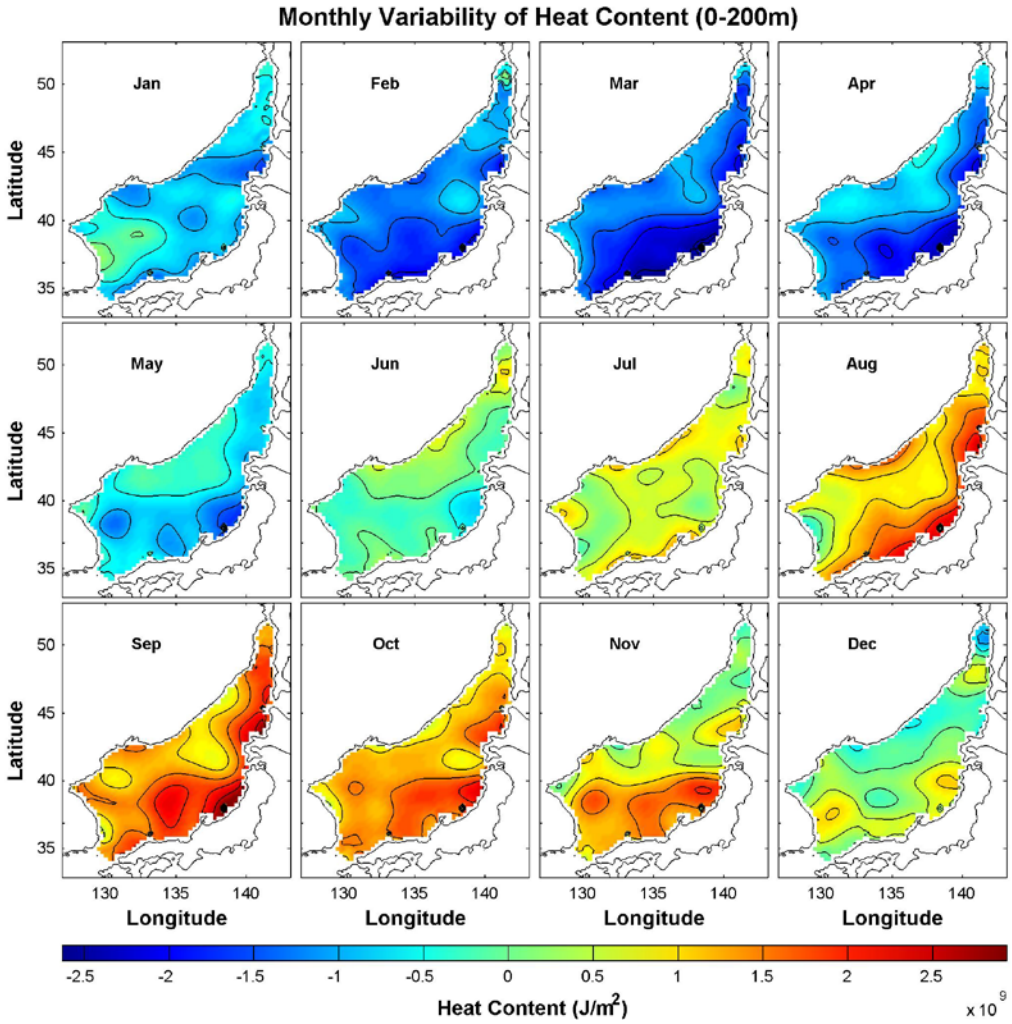

More dynamic changes of heat content were found along the west coast of Honshu than in other areas. The range of heat content change is approximately five times less in the intermediate layer. From October to December, heat loss along the west coast of Honshu was observed, and from December to February, heat content increase near the Tatar Strait was observed (see Figure 36).

Figure 36. Monthly Variability of Heat Content (J/m^2) in Intermediate Layer

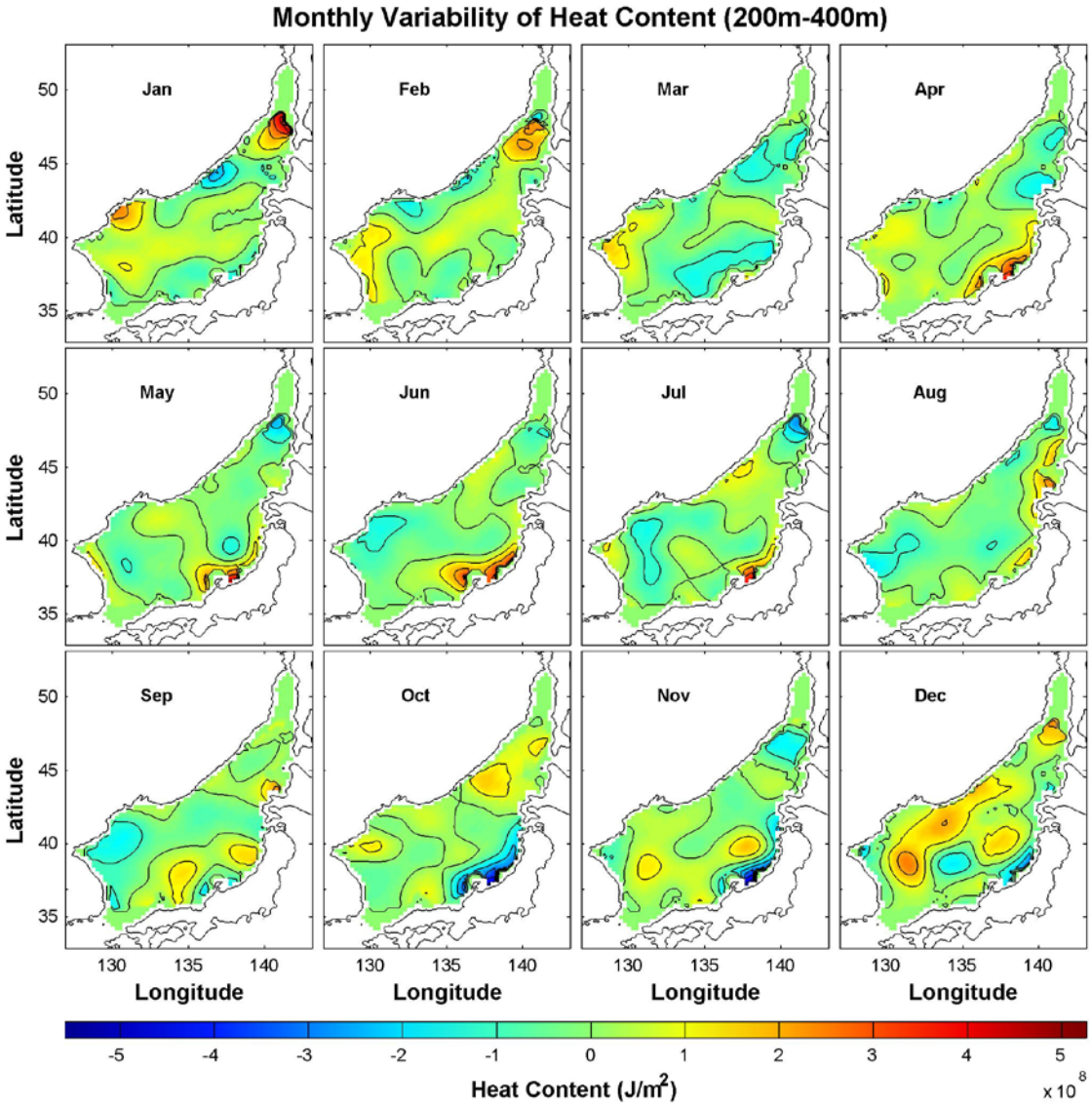

No significant heat content change was observed in deep layer except rising heat content in a wide area of the northeastern ES in January and February (see Figure 37).

This area loses heat from March to August. But an exceptional heat gain in June was observed between the Soya Strait and Russian coast.

Figure 37. Monthly Variability of Heat Content (J/m^2) in Deep Layer

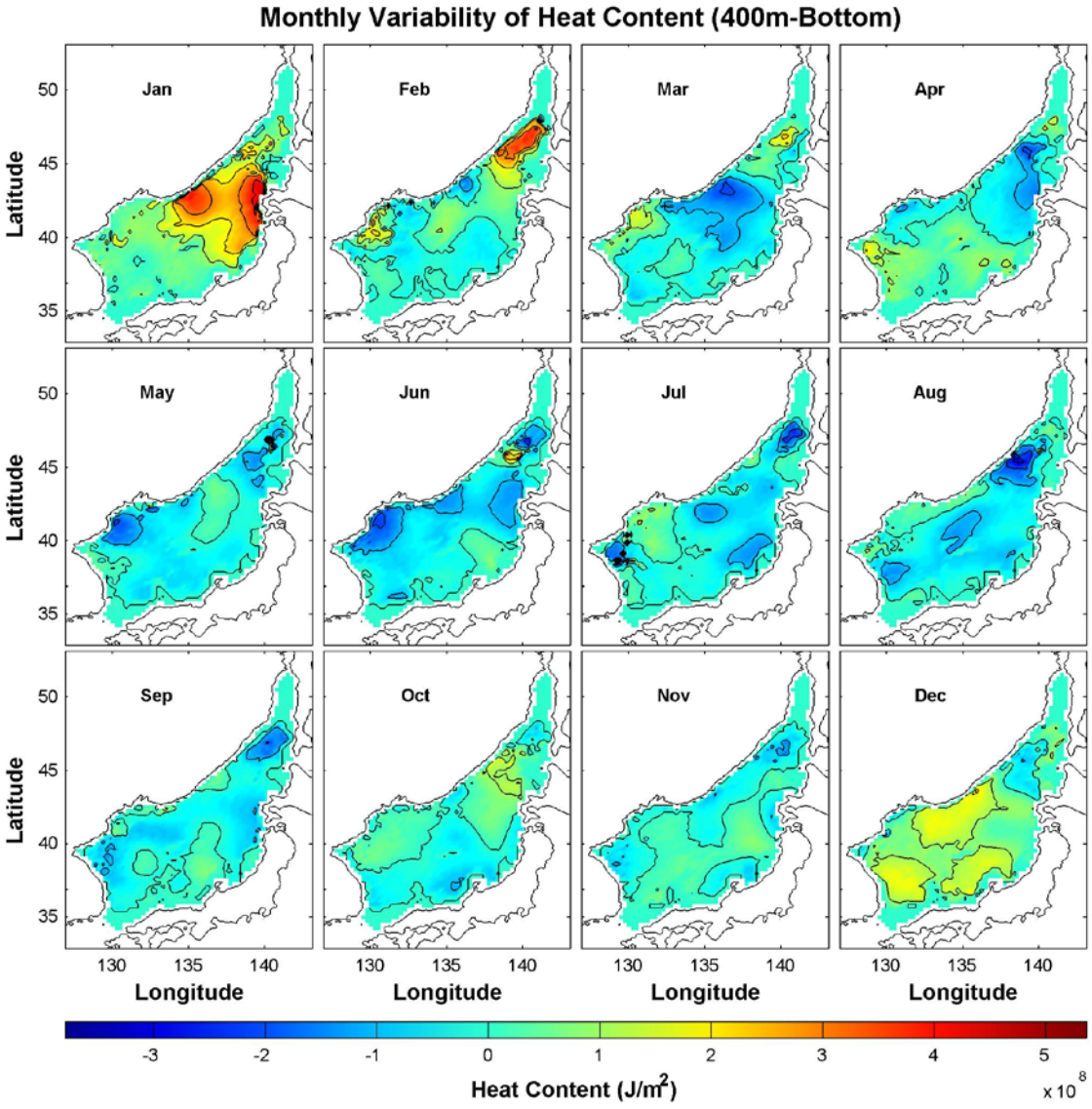

E. INTER-ANNUAL HEAT CONTENT CHANGE

Figure 38 and 39 shows the heat stored in the ES had significantly increased since 1985, especially with a very high rate in the intermediate layer. Large heat content in surface layer was observed in 1960s, but it gradually decreased until the 1980s and roughly 3×10^{15}J of heat content increased for the last 30 years. In the intermediate layer in same period, a 2×10^{15}J increase was observed. An increase in heat content was also observed in all layers since 1990.

Numerous evidence about warming was reported in last several years. Kim et al. (2001) reported "temperature has gone up as much as 0.1 ~ 0.5 °C in the upper 1,000m and by 0.01°C below 2,000m for the last 30 years, increasing the heat content per unit area below 500m at a rate of 0.54 W/m^2." (Kim et al., 2001) Sea level rise is also reported as evidence of warming. "According to the analysis of satellite altimeter data, the rate of the sea level rise surrounding Dokdo and Ulleungdo is similar to the rate derived from coastal tide data." (Kang et al. 2005) Research by Kang et al. (2005), shows the sea level rise rate of Ulleungdo and Dokdo for last nine years (6.5mm per year) was more than twice the rate for last 30 years (3.2mm per year). Temperature increase in the ES is estimated by this remarkable sea level rise rate change and larger temperature increase in the ES than global ocean temperature increase is also estimated since sea level rise in the ES is twice the global mean. (National Geographic Information Institute, 2015: The Geography of Dokdo. Accessed 10 December 2015. [Available online at http://www.ngii.go.kr/dokdoen/contents/contentsView.do?rbsIdx=54#none])

This significant heat content rate change in the intermediate layer may cause a need for redefining the water mass of the ES. According to report of the Korea National Geographic Information Institute (http://dokdo.ngii.go.kr/dokdo/contents/contentsView.do?rbsIdx=48#none), water which used to sink to the deep layer in the northern part of the ES is reduced and reaches only to intermediate layer because not enough cooling was made, due to a rise in surface water temperature. Therefore, the volume of the deep layer may decrease, and the volume of the intermediate layer may increase in the future.

Figure 38. Temporally Varying Horizontally Integrated ES Heat Content (Joules) of the Three Layers Without Seasonal Variability

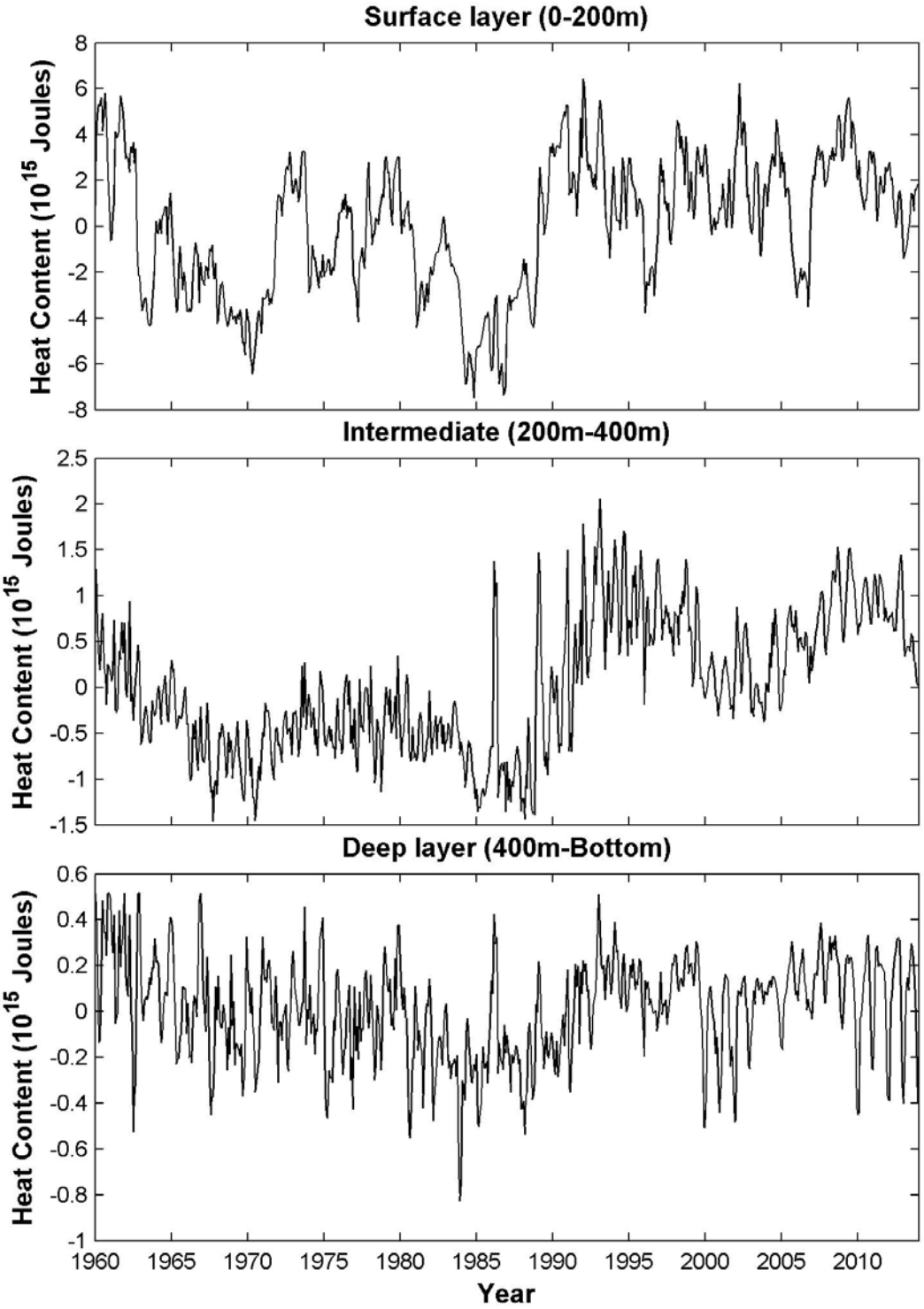

(a) surface layer (0 ~ 200 m), (b) intermediate layer (200 ~ 400 m), and deep layer (400 m ~ bottom).

Figure 39. Temporally Varying Horizontally Integrated ES Heat Content (Joules) of the All Layer Without Seasonal Variability

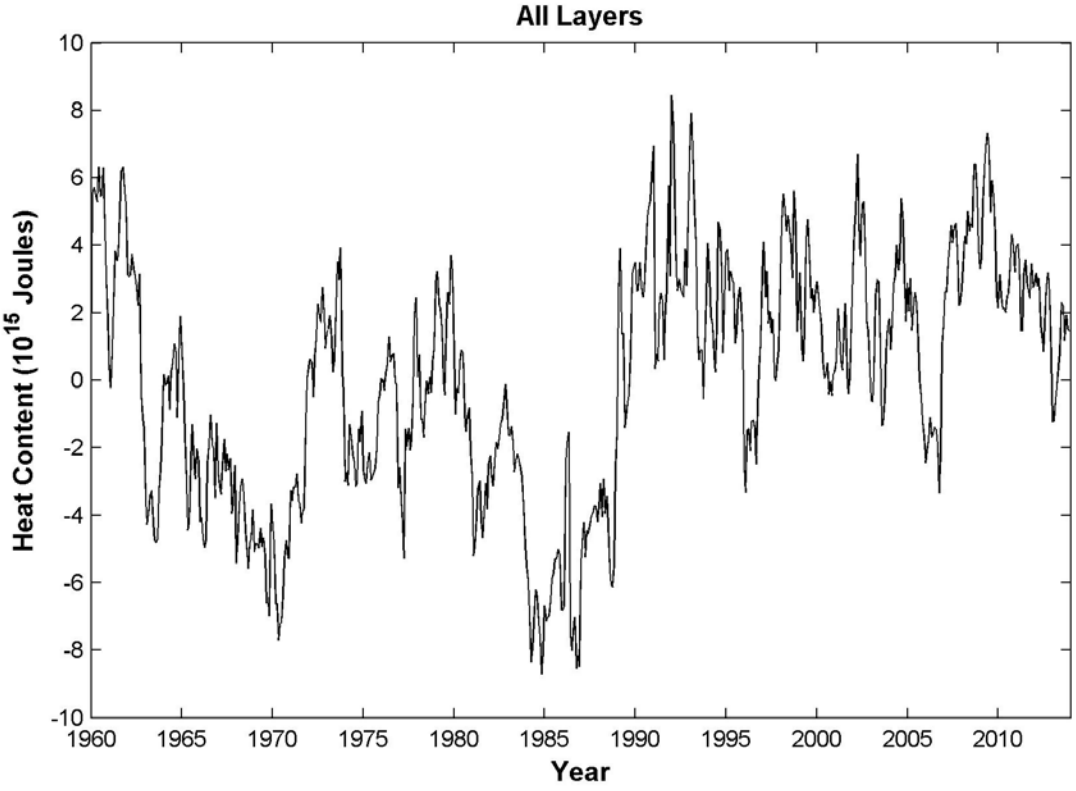

F. FRESHWATER CONTENT

Freshwater content represents the freshwater stored in sea water. Freshwater content was calculated in each layer in (30) where S_{ref} represents salinity reference. 40 psu was used for S_{ref} in this calculation.

$$\mathrm{FWC} = \int_{-h_2}^{-h_1} \frac{S_{ref} - S}{S_{ref}} dz \qquad (30)$$

which is decomposed into climatological monthly mean and anomaly (representing inter-annual variability) FWC.

Figure 40. Monthly Variability of Freshwater Content (m) in Surface Layer

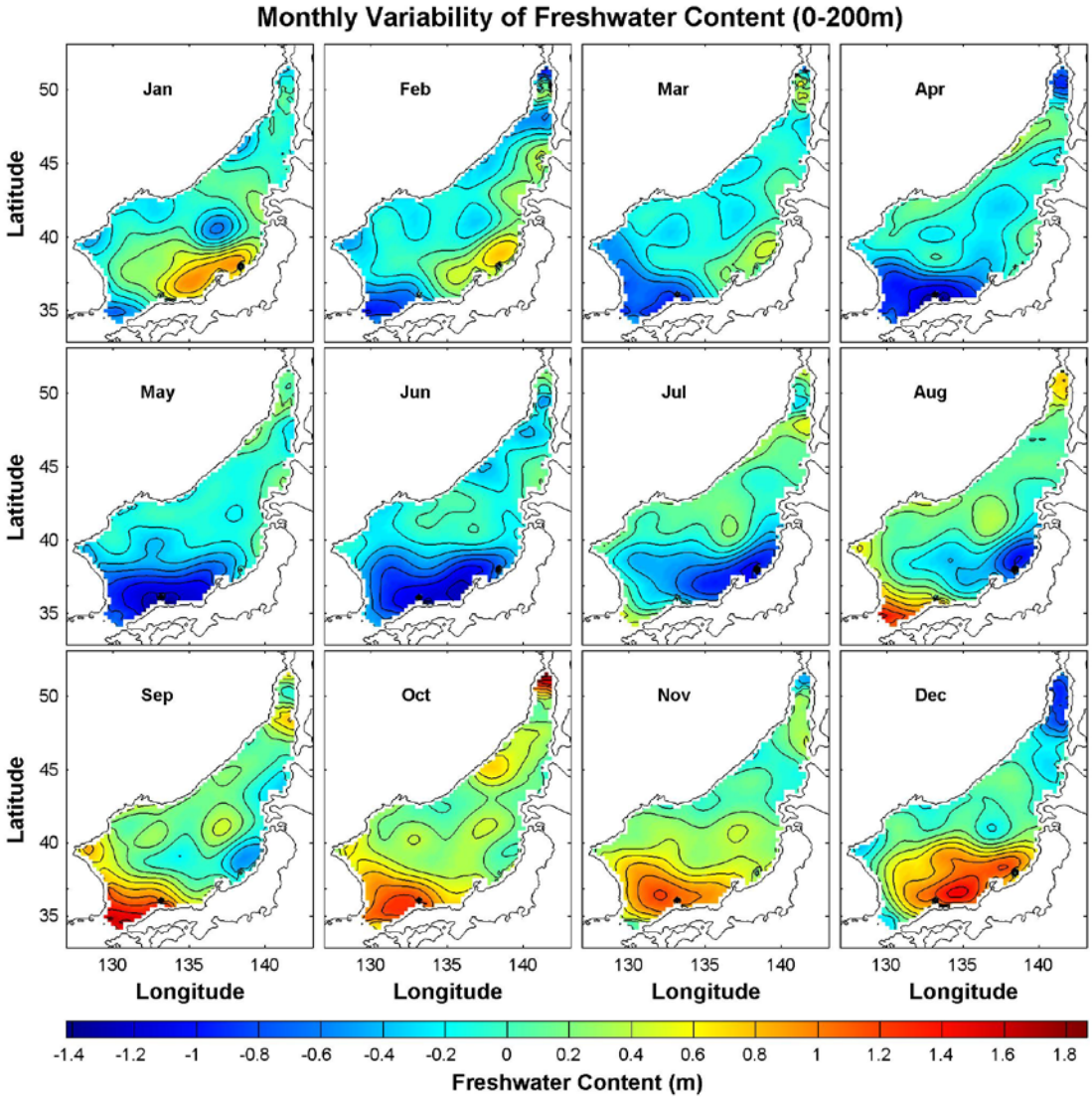

The freshwater content of the surface layer increased from August to January (see Figure 40); this freshwater increase comes through the Korea Strait. From February to July, there is a decrease through the Korea Strait. Another freshwater increase is observed near the Tatar Strait in October. These freshwater content changes match with low salinity due to discharge from the Amur River and Changjiang River explained in Figure 26.

Figure 41. Monthly Variability of Freshwater Content (m) in Intermediate Layer

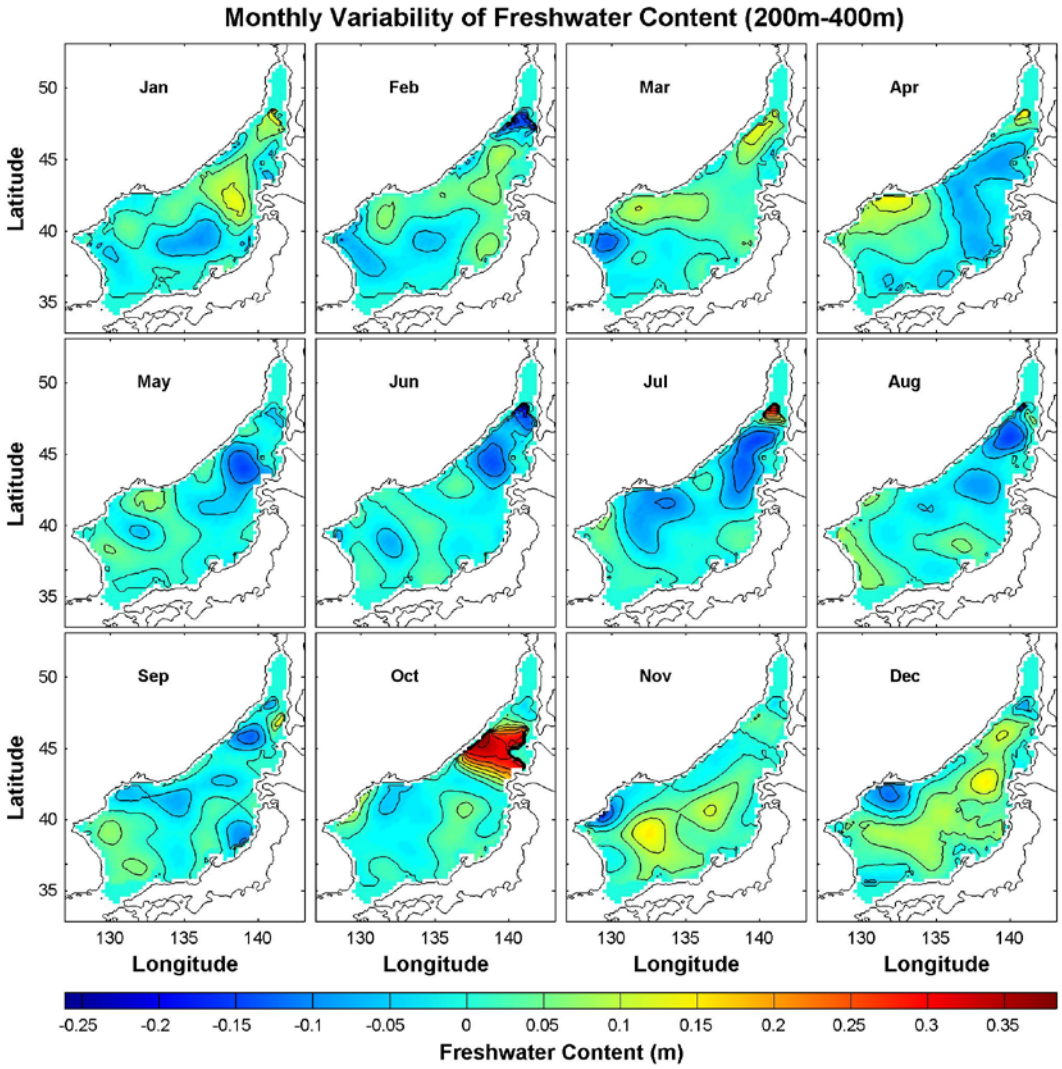

No significant freshwater variation was observed in the intermediate layer except for a large freshwater increase between the Russian coast and Hokkaido in October (see Figure 41). This freshwater may have originated in the Amur River discharge, but it is wider than the freshwater of the surface layer. Another freshwater increase near the Tatar Strait was found in July, but it is smaller than October's increase.

Figure 42. Monthly Variability of Freshwater Content (m) in Deep Layer

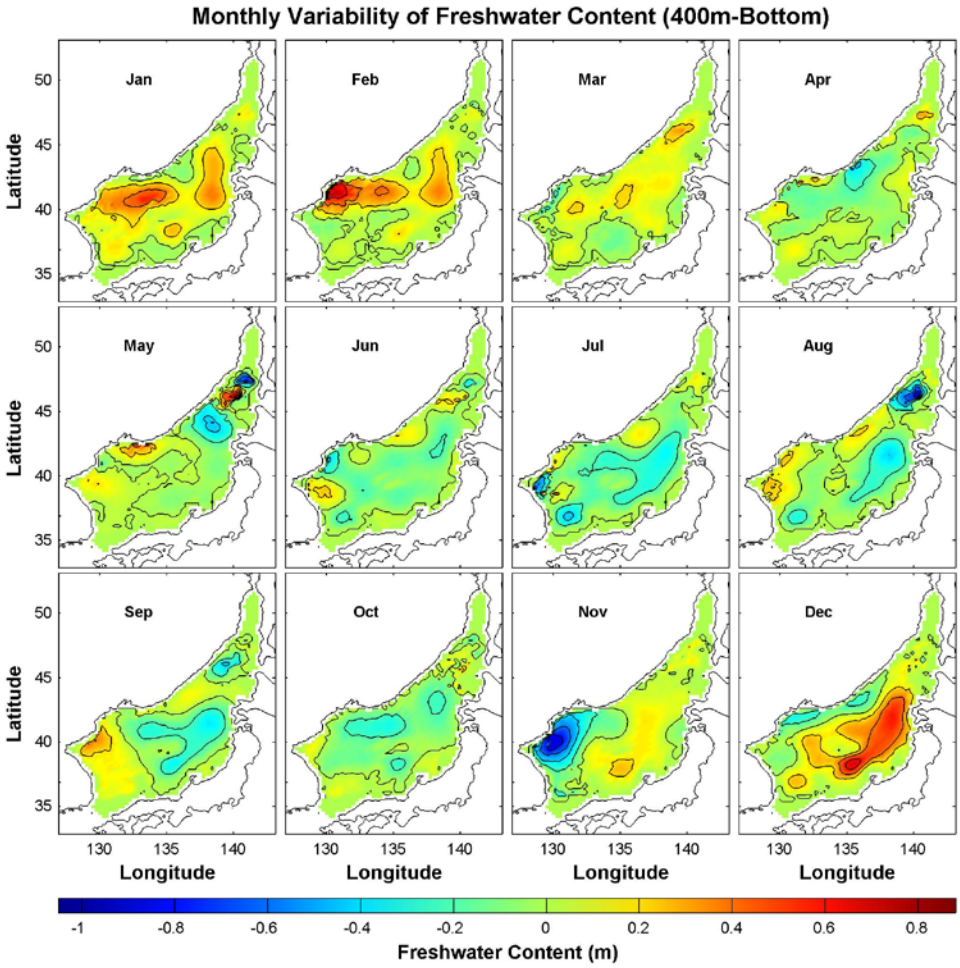

Freshwater content increase due to river discharge is not found in the deep layer (see Figure 42). However, freshwater content has been drastically changed along the North Korean coast and south of Vladivostok from November to February. Wide increase of freshwater is also found in the YB in December.

THIS PAGE INTENTIONALLY LEFT BLANK

V. INTER-ANNUAL VARIABILITY

Inter-annual variability analysis allows for understanding anomalies in the variables. In this chapter, the EOF is shown from mode1 to mode4. Each EOF is plotted by each layer. The EOF represents the spatial variation of each layer, and the PC represents temporal variation of 54 years. The percentage of retained energy decreases by mode; thus EOF-1 has the largest percentage. Due to the largest percentage of retained energy in the first mode, the tendency of each variable in each layer is most accurately represented in EOF-1.

A. FIRST THREE EOFS OF HEAT CONTENT ANOMALY FOR THE THREE LAYERS

The surface layer's heat content range is approximately five times larger than the intermediate layer's, and the intermediate layer's heat content range is also approximately five times larger than the deep layer's (see Figure 43). Therefore, the surface layer's heat content inter-annual variability has most strength. Multiplying the PC and the EOF shows heat content contribution.

For example, the highest heat content point of the surface layer (0.06) × PC of 1960 ($25 \times 10^9 J/m^2$) = $1.5 \times 10^9 J/m^2$. If the sign of the PC is negative, the heat content contribution is also negative, such as highest heat content point of the surface layer (0.06) × PC of 1985 ($-25 \times 10^9 J/m^2$) = $-1.5 \times 10^9 J/m^2$. The changing heat content would be determined with these calculations. Horizontal inhomogeneity in heat content is more significant in the surface layer for all modes (see Figure 44 and 45).

For the most part, PC_1 stays positive after 1990. Since most EOF_1 is positive in most areas, a broad heat content increase may be estimated. This pattern is very similar to horizontally integrated ES heat content of all layers (see Figure 39): decreasing heat content after 1960 and a significant increase in 1990s. The EOF is positive in most parts of all layers; thus, heat content has been raised in all layers since 1990.

Figure 43. EOF-1 And PC_1 of the Surface Layer (0~200m), Intermediate Layer (200~400m) and Deep Layer (400m~Bottom) Heat Content Anomaly (J/m^2)

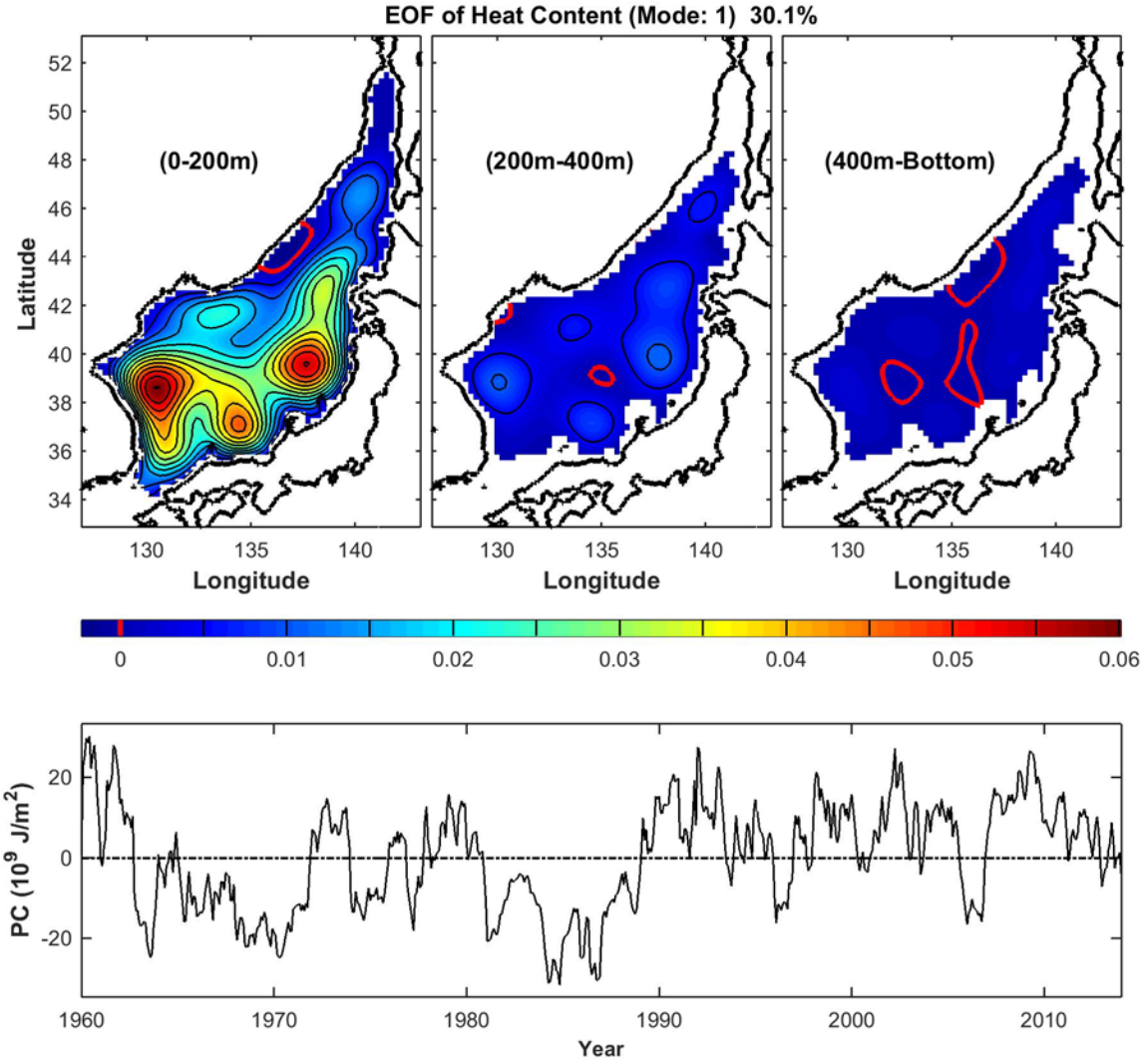

Figure 44. EOF-2 And PC_2 of the Surface Layer (0~200m), Intermediate Layer (200~400m) and Deep Layer (400m~Bottom) Heat Content Anomaly (J/m^2)

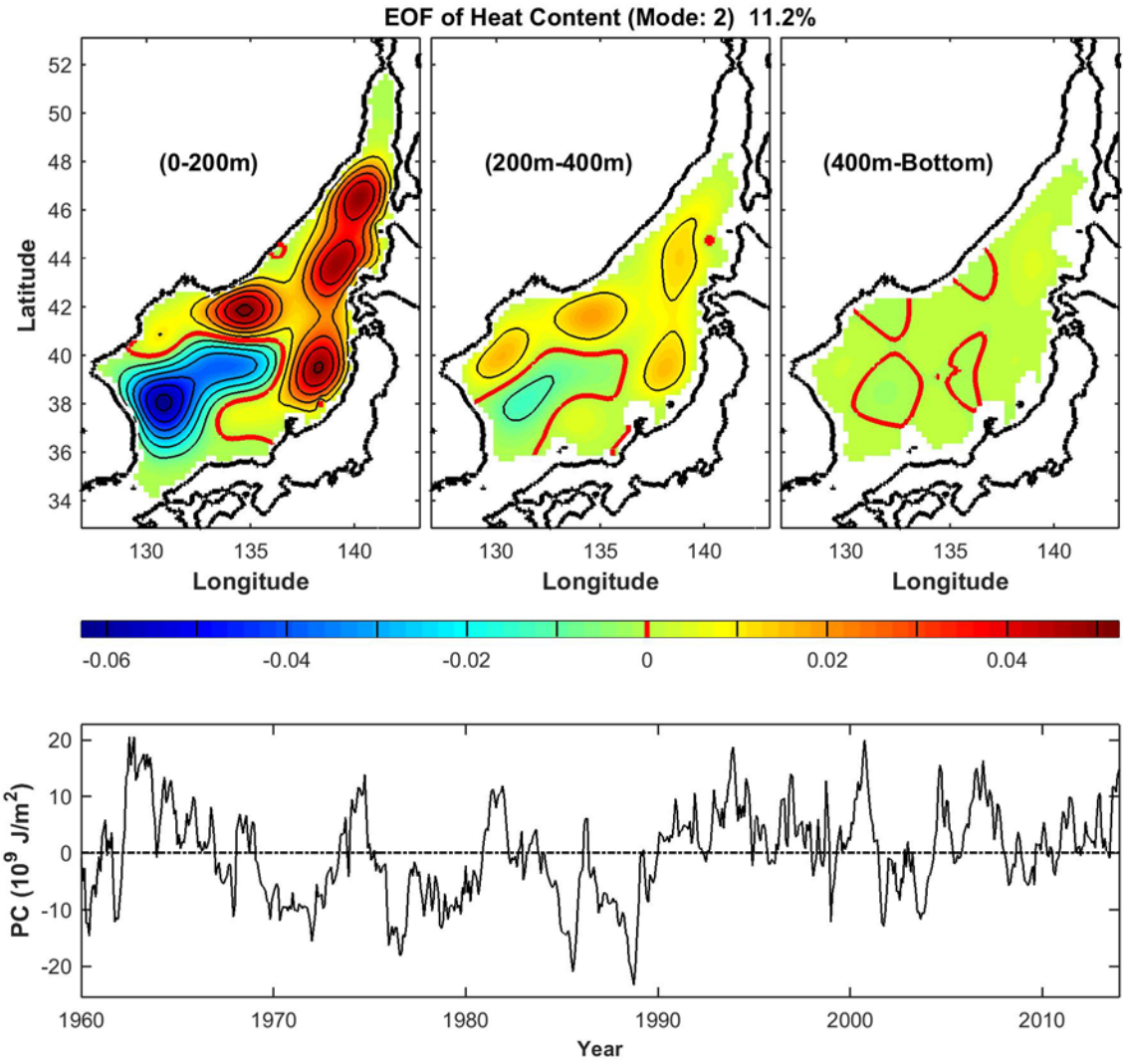

Figure 45. EOF-3 And PC_3 of the Surface Layer (0~200m), Intermediate Layer (200~400m) and Deep Layer (400m~Bottom) Heat Content Anomaly (J/m^2)

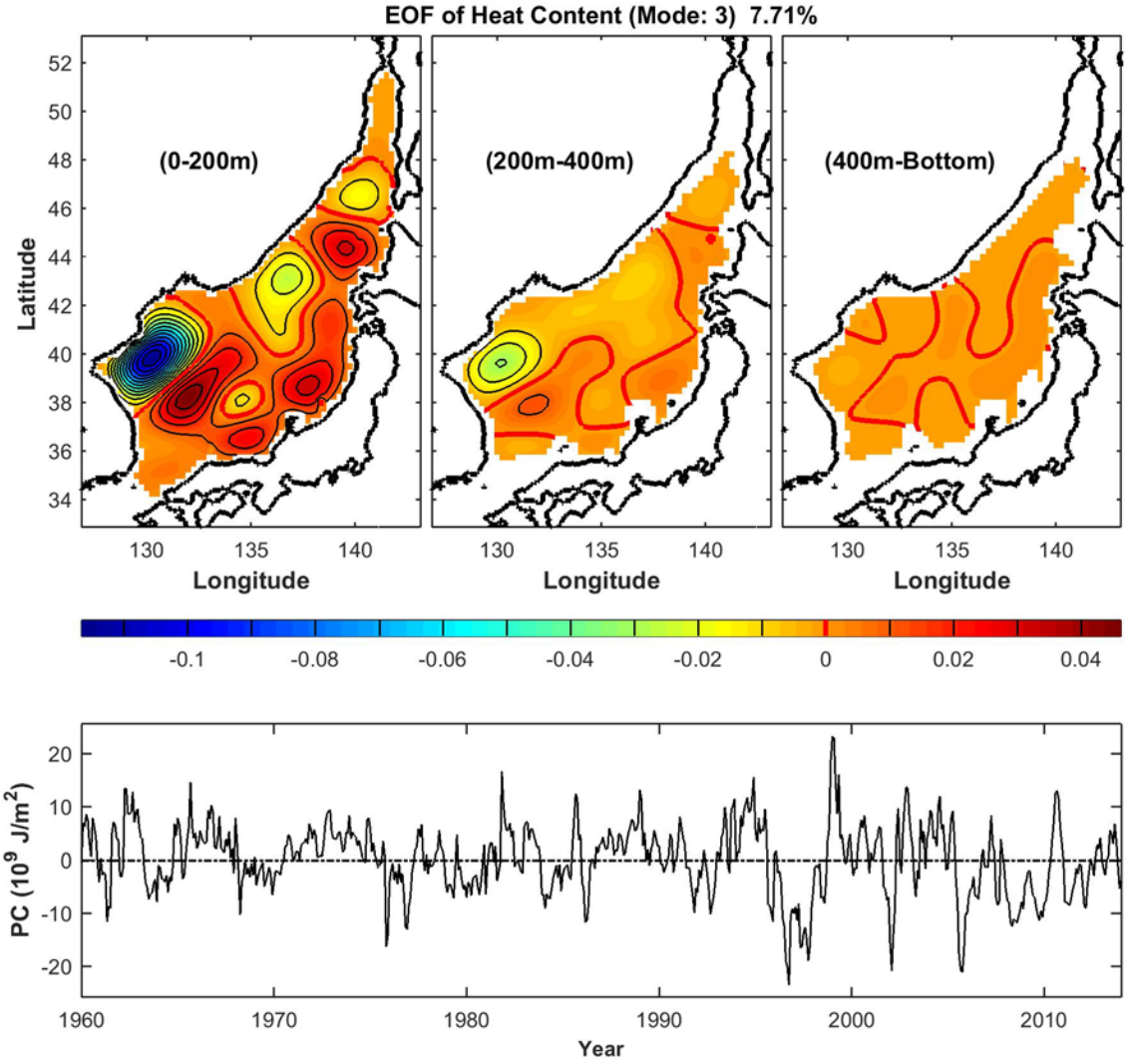

B. FIRST THREE EOFS OF FRSHWATER CONTENT ANOMALIES FOR THE THREE LAYERS

The PC_1 stays positive for most part since the mid-1990s when the sign was opposite before the mid-1990s (see Figure 46). Therefore, a significant salinity change is estimated, especially for increasing salinity in deep layer in the mid-1990s. For example, in the deep layer in 1995, the YB was saltier with the index of -0.07 × 25m = -1.75m, while south of Vladivostok was fresher with an index of 0.02 × 25m = 0.5m.

Figure 46. EOF-1 and PC_1 of the Surface Layer (0~200m), Intermediate Layer (200~400m) and Deep Layer (400m~Bottom) Freshwater Content Anomaly (m)

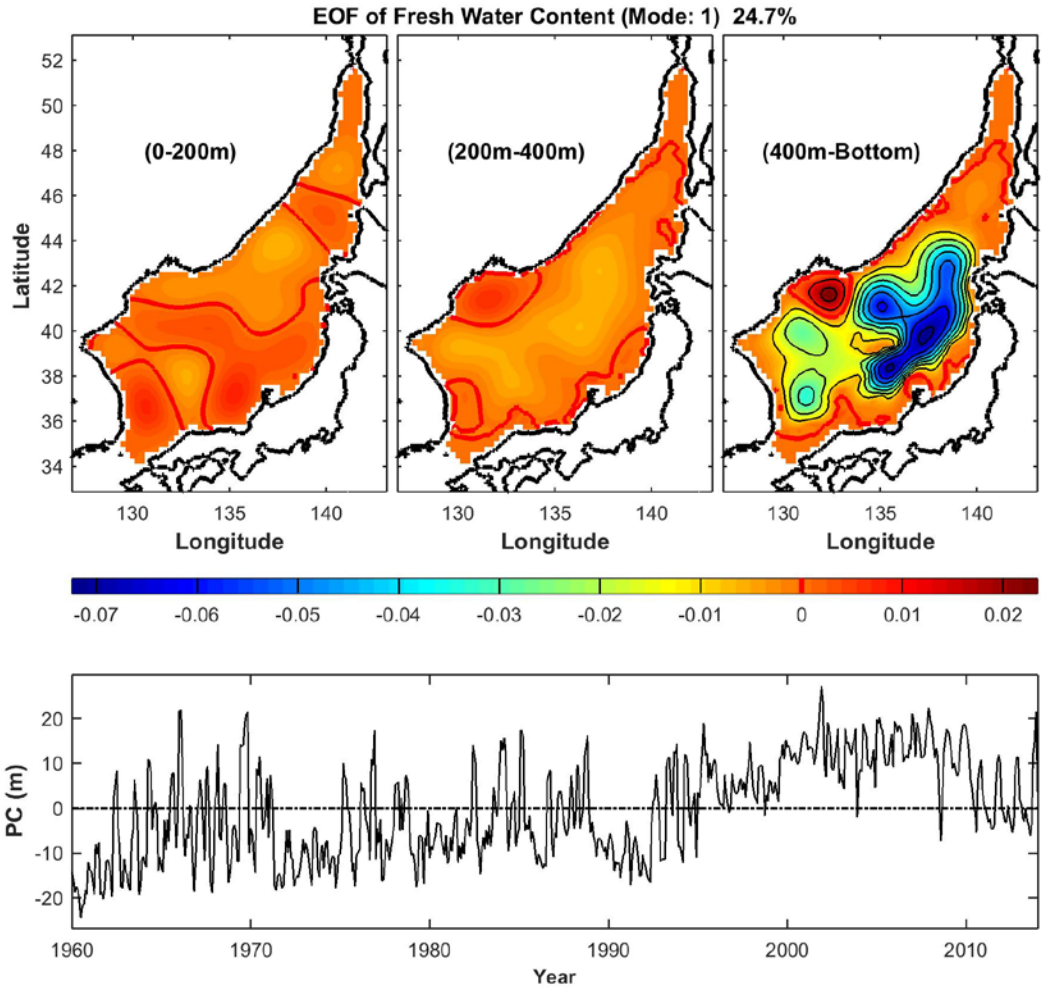

At the same time, other layers had less variation. Index range difference was approximately 0.09 in the deep layer, but it was approximately 0.01 in both the surface and the intermediate layers. This calculation shows that the deep layer had more change in freshwater content. Various freshwater content range differences are found in the deep layer for all modes (see Figure 47 and 48); thus, the difference in freshwater content according to area is more significant in the deep layer.

Figure 47. EOF-2 and PC_2 of the Surface Layer (0~200m), Intermediate Layer (200~400m) and Deep Layer (400m~Bottom) Freshwater Content Anomaly (m)

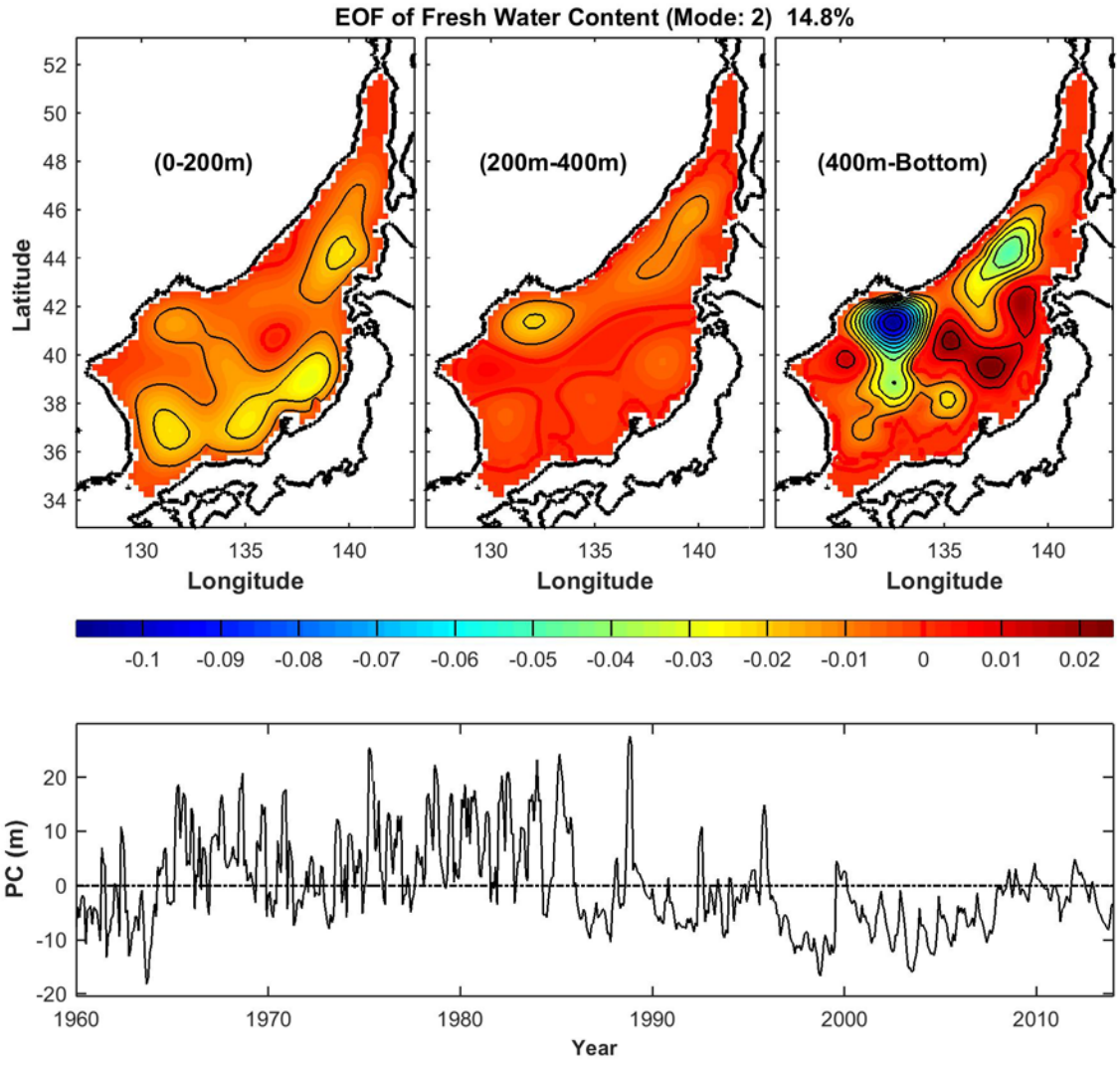

Figure 48. EOF-3 and PC_3 of the Surface Layer (0~200m), Intermediate Layer (200~400m) and Deep Layer (400m~Bottom) Freshwater Content Anomaly (m)

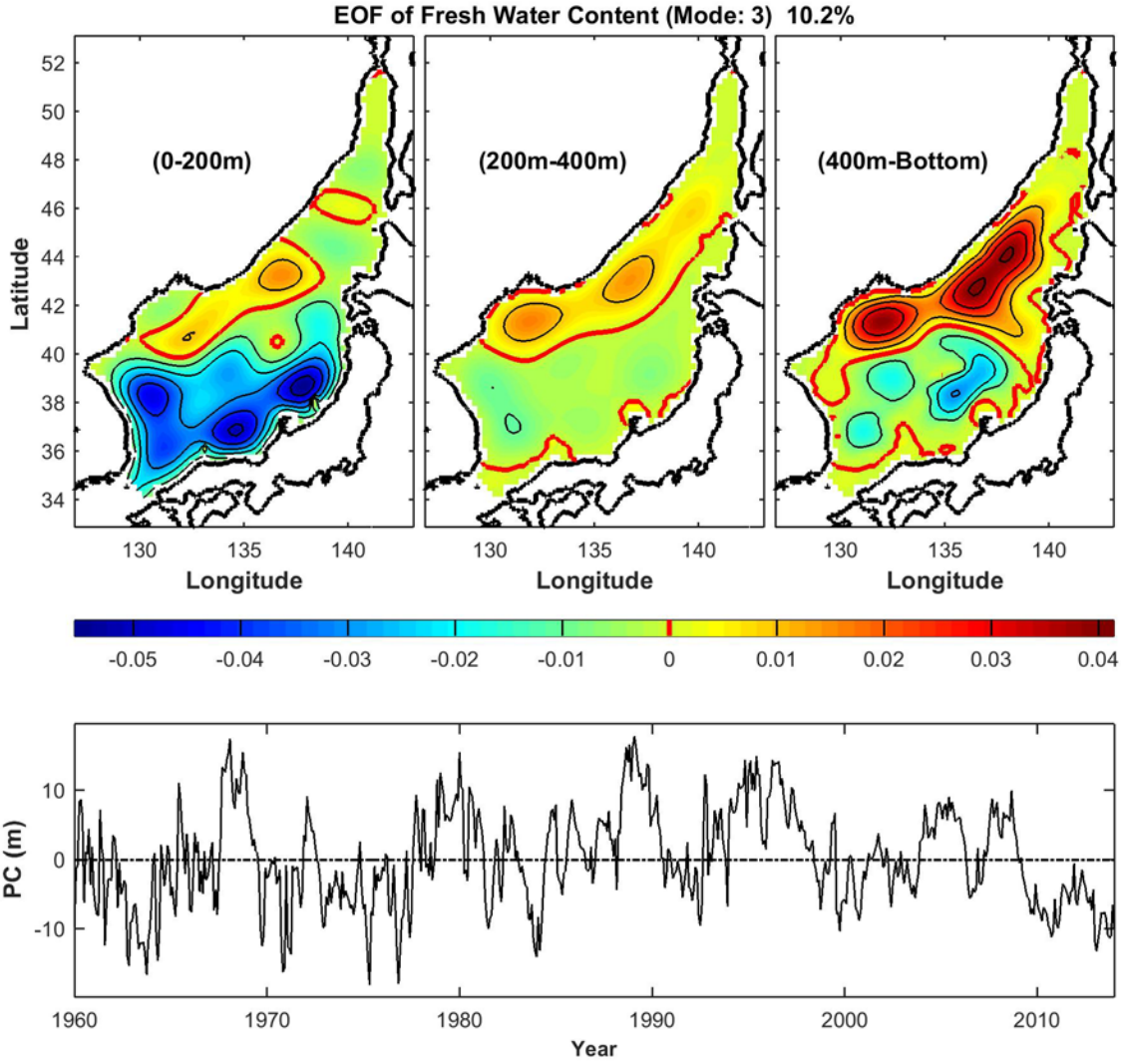

THIS PAGE INTENTIONALLY LEFT BLANK

VI. CONCLUSIONS AND FUTURE RECOMMENDATIONS

A. CONCLUSIONS

Synoptic monthly varying 3-D gridded temperature and salinity data were established in this thesis for the East Sea (January 1960 to December 2013) with $0.25^{o}\times0.25^{o}$ horizontal resolution and 57 vertical levels as World Ocean Atlas 2009 from 342,617 temperature and 163,502 salinity profiles using the optimal spectral decomposition for naval/oceanographic research.

In temperature distribution, delays of SST seasonal peaks after summer seasonal wind peaks in June and winter seasonal wind peaks in January were found. Comparison of the monthly mean temperature for 54 years in this research with monthly mean temperature for 21 years by KHOA data shows that the month of the highest SST was September in both studies but different months displayed the lowest SST. In the 54-year data set's mean, the lowest SST is in February, with a one-month delay after winter wind peak, but the mean for the 21-year data set was January. At 400m depth, the colder water in basins enlarged in summer and shrunk in winter.

In salinity distribution, a low salinity effect caused by Amur River discharge into the Tatar Strait and one-month delay after maximum discharge in September was noticed. Another low salinity effect through the Korea Strait via Changjiang River discharge into the ECS was found. Like the temperature distribution, the salinity distribution along the coast of Honshu also matches the nearshore branch of the TWC.

By absolute geostrophic velocity distribution, a strong inflow in the surface layer through the Korea Strait in summer was observed when low salinity near Korea Strait was caused by Changjiang River discharge. An anticyclonic pattern of Ulleung Warm Eddy in intermediate layer and opposite pattern in deep layer was noticed.

Inter-annual variability by EOF analysis shows that the heat content difference according to area is more significant in the surface layer and the freshwater content difference according to area is more significant in the deep layer. By temporal analysis, increase of heat content in all area and layers since 1990 and decrease of freshwater in

deep layer since mid-1990s were identified. It may link to climate change and global warming.

B. FUTURE RESEARCH

The existence of shorter and stronger Siberian winter wind in recent decades is estimated, due to differences in the lowest month of SST in 21 years mean and 54 years mean, but this is not scientifically proved. Detailed study with atmospheric data and numerical modeling could be worth for air-ocean interaction by changing pattern of seasonal wind.

Freshwater inflow by Amur River discharge peak was found from surface to 400m depth; therefore, the sinking of freshwater can be good source for study of the salinity distribution near the Tatar Strait.

Since the Changjiang discharge peak strongly influenced less saline water inflow through the Korea Strait in summer, a study of the temporal relation between discharge peak month of Changjiang and low salinity month of the Korea Strait is suggested. This study may be extended to inflow volume through the Korea Strait due to sea level rise of the ECS.

Cyclonic circulation in the UB at 1,000m matches with Senjyu's study in 2005, but more research is needed to determine the flow direction in this area since a full report of flow direction is not cleared yet.

APPENDIX A. MONTHLY MEAN BY DEPTH

A. TEMPERATURE

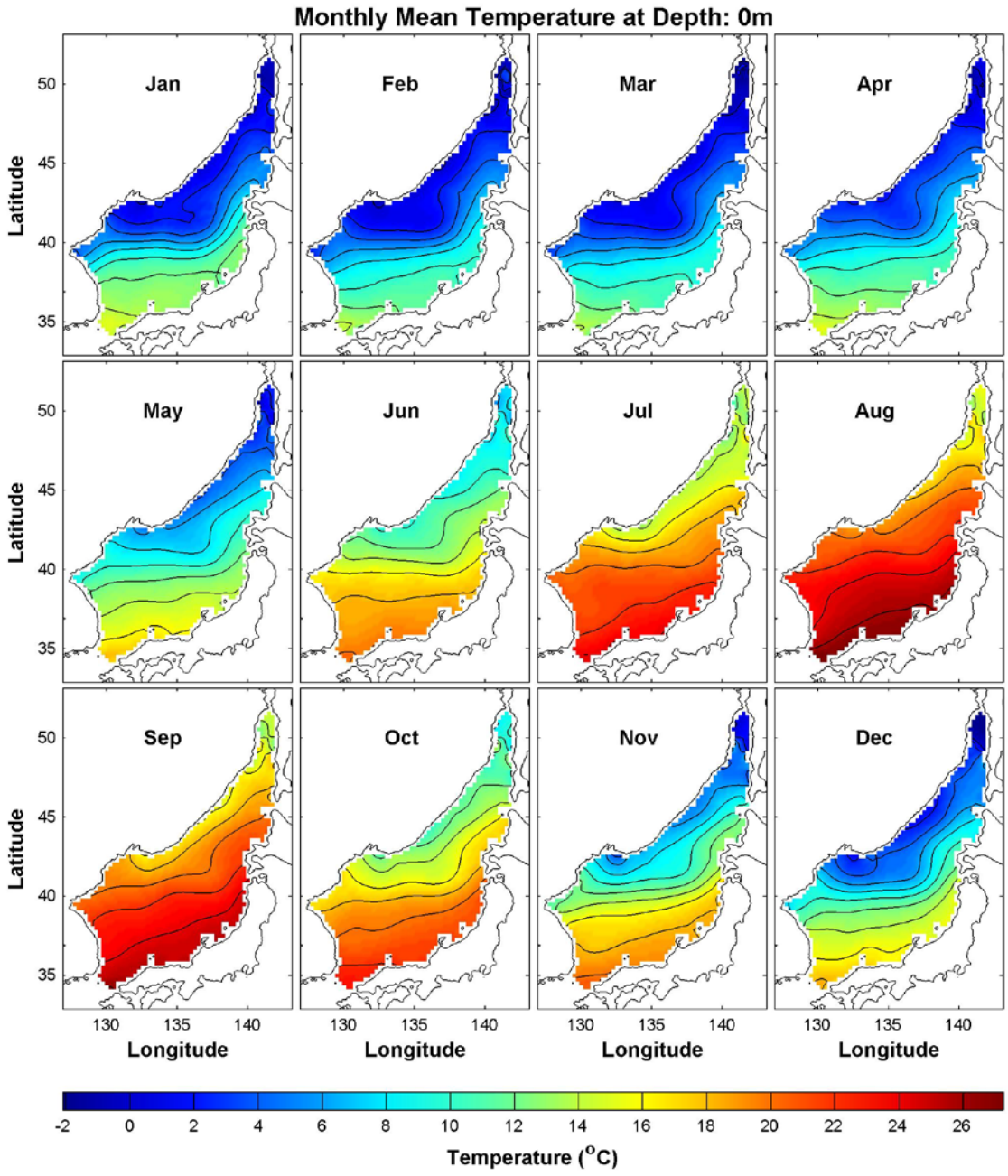

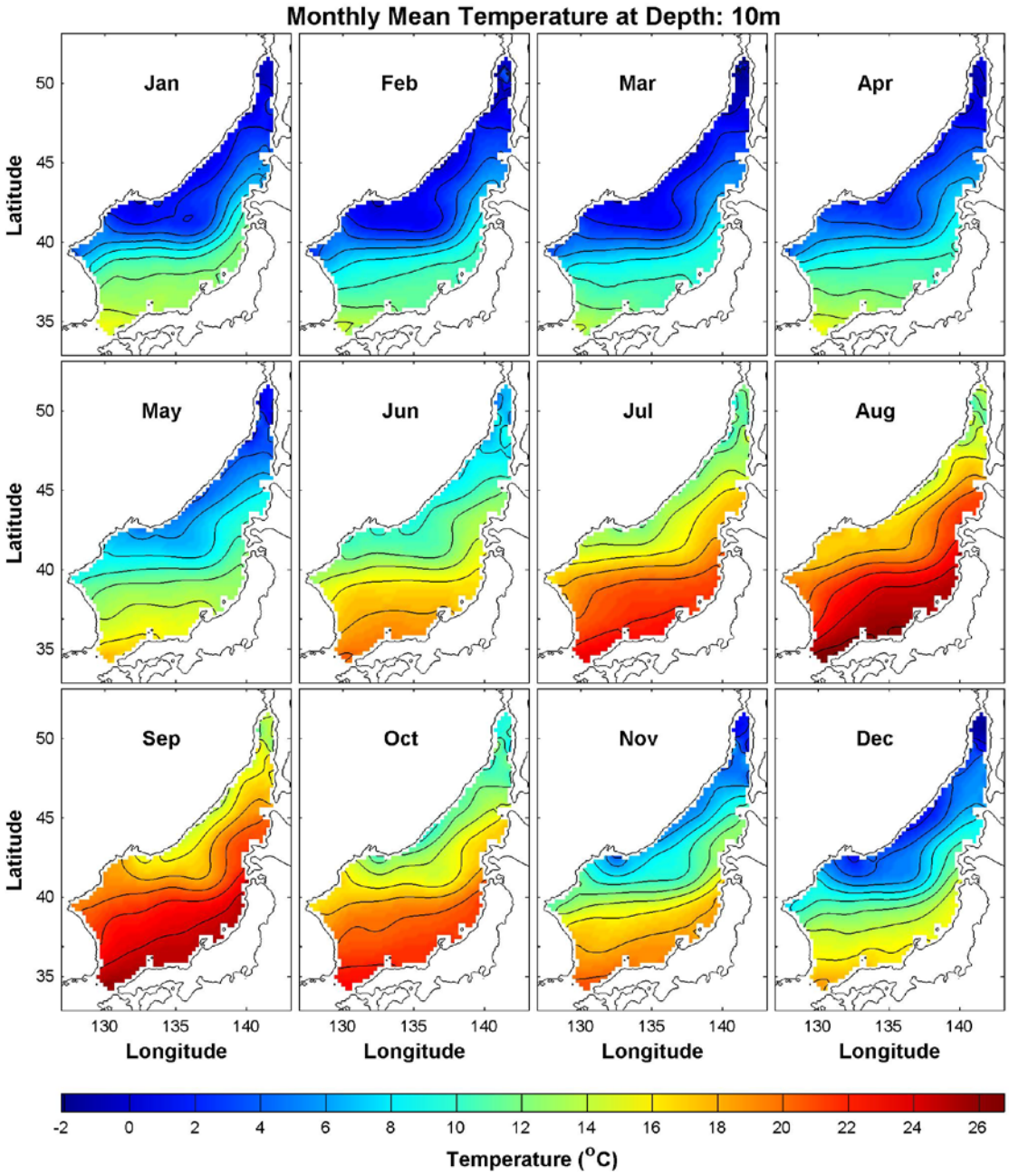
Monthly Mean Temperature at Depth: 10m
Jan
Feb
Mar
Apr
May
Jun
Jul
Aug
Sep
Oct
Nov
Dec
Latitude
Longitude
50
45
40
35
130
135
140
-2
0
2
4
6
8
10
12
14
16
18
20
22
24
26
Temperature (°C)

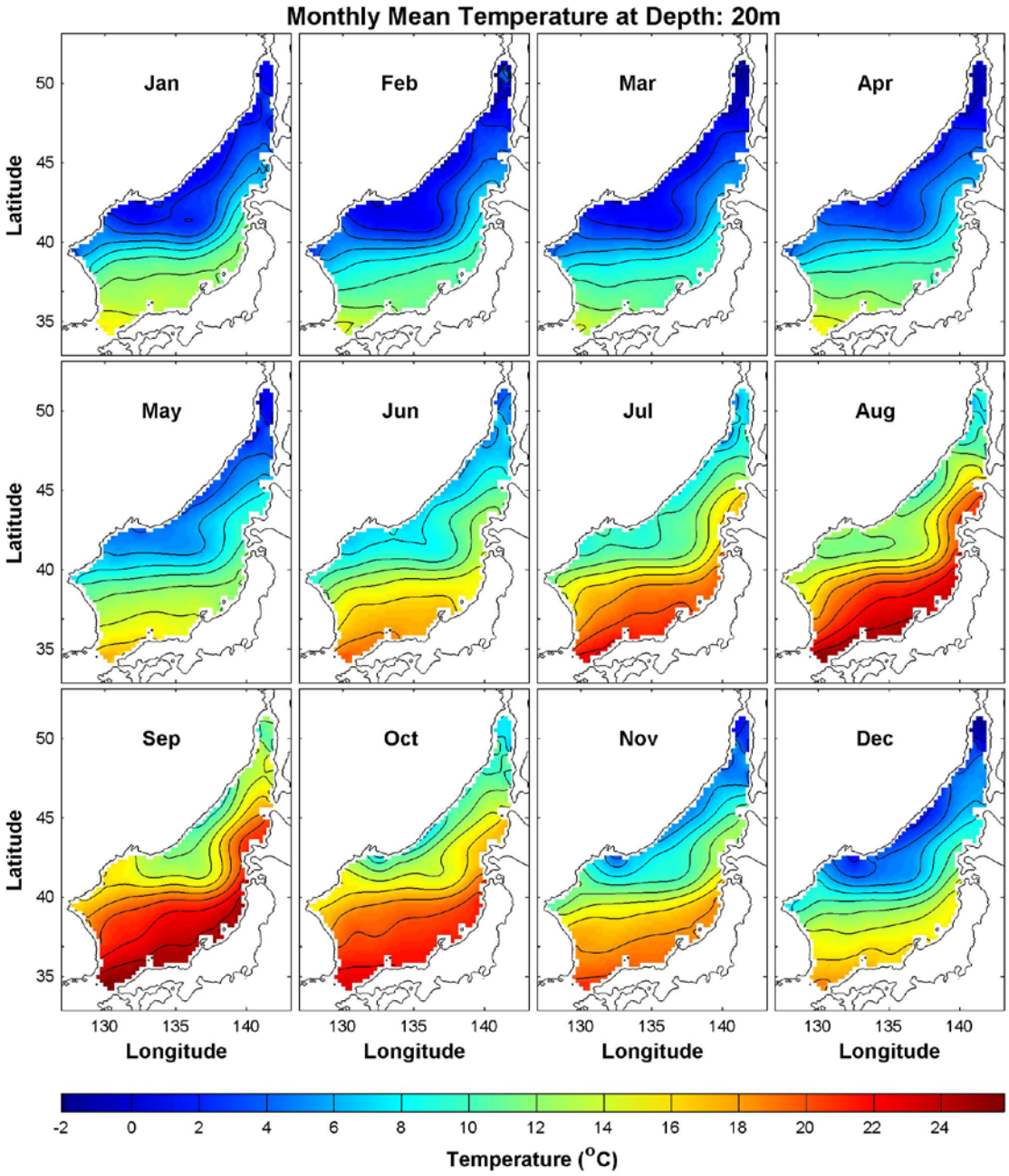
Monthly Mean Temperature at Depth: 20m
Jan
Feb
Mar
Apr
May
Jun
Jul
Aug
Sep
Oct
Nov
Dec
Latitude
Longitude
50
45
40
35
130
135
140
-2
0
2
4
6
8
10
12
14
16
18
20
22
24
Temperature (°C)

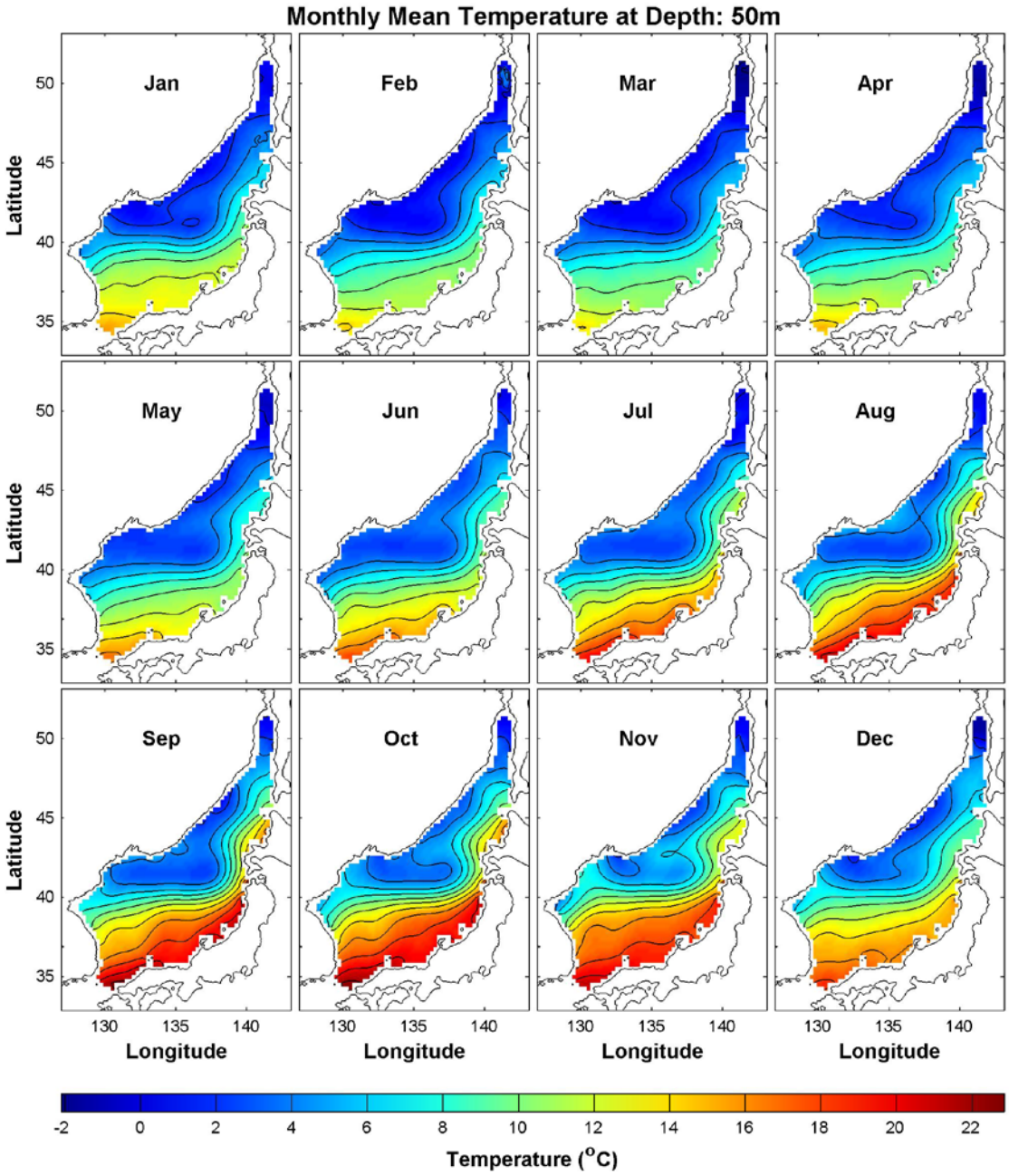
Monthly Mean Temperature at Depth: 50m
Jan
Feb
Mar
Apr
May
Jun
Jul
Aug
Sep
Oct
Nov
Dec
Latitude
Longitude
50
45
40
35
130
135
140
-2
0
2
4
6
8
10
12
14
16
18
20
22
Temperature (°C)

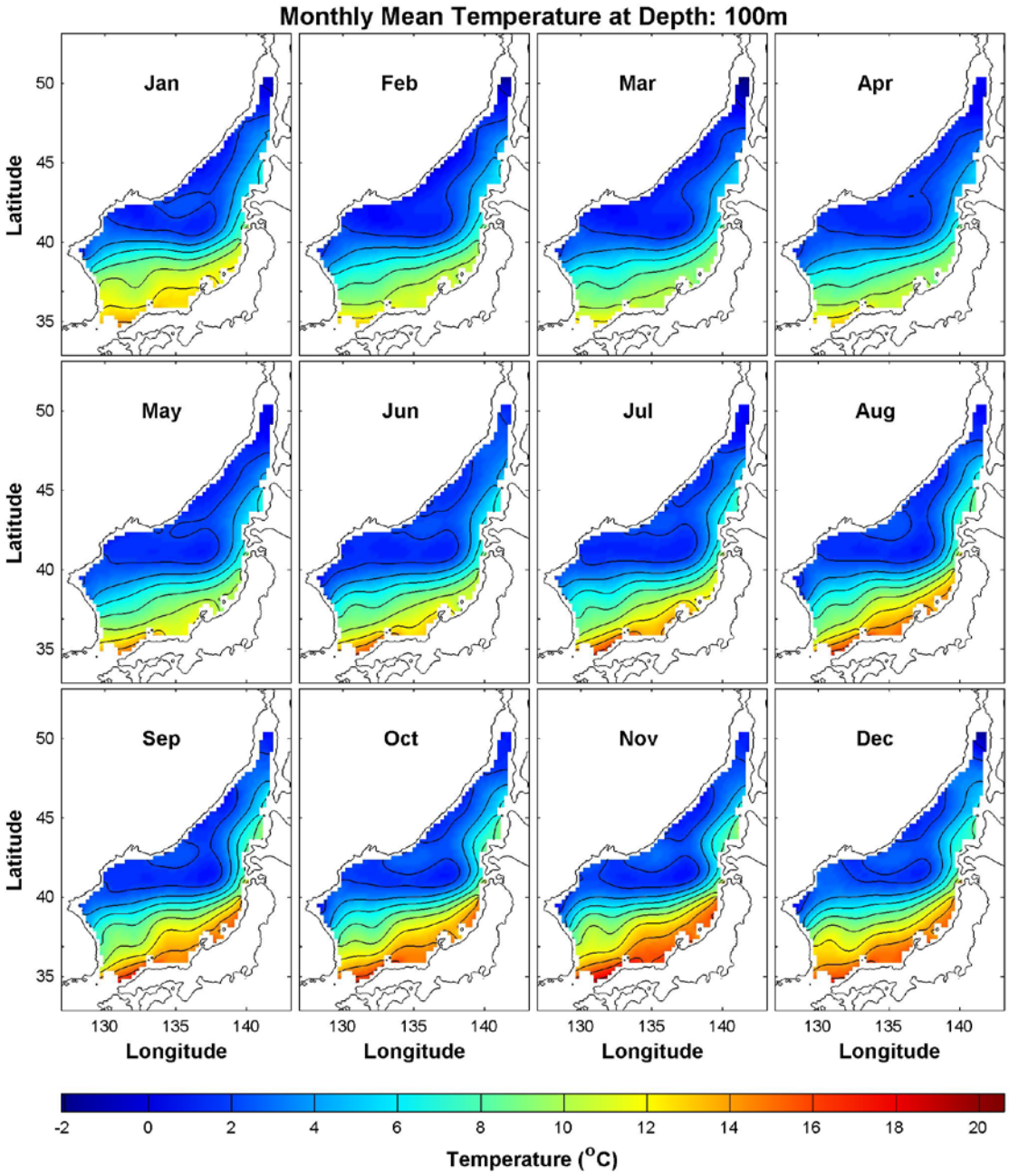
Monthly Mean Temperature at Depth: 100m
Jan
Feb
Mar
Apr
May
Jun
Jul
Aug
Sep
Oct
Nov
Dec
Latitude
Longitude
50
45
40
35
130
135
140
-2
0
2
4
6
8
10
12
14
16
18
20
Temperature (°C)

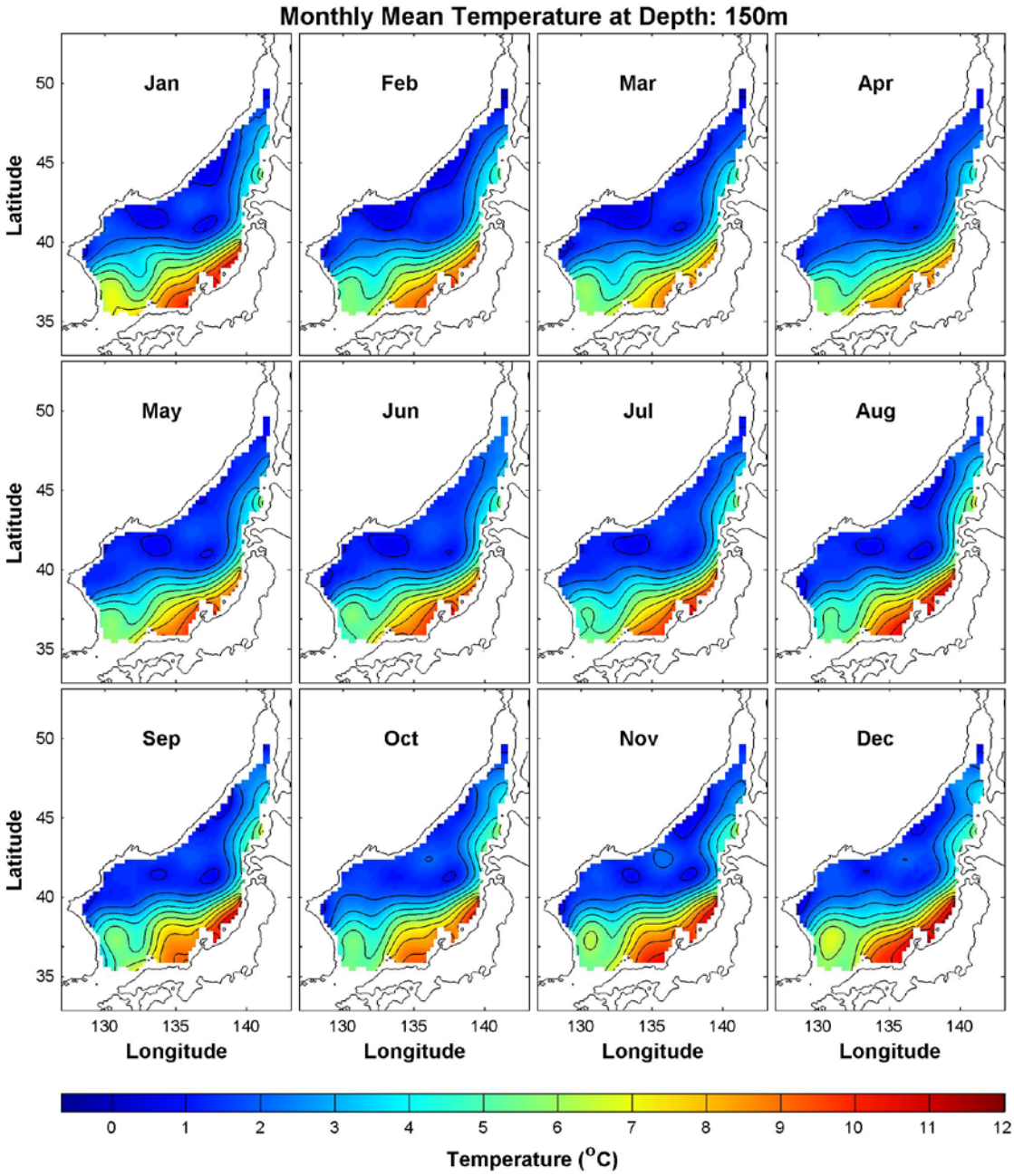
Monthly Mean Temperature at Depth: 150m
Jan
Feb
Mar
Apr
May
Jun
Jul
Aug
Sep
Oct
Nov
Dec
Latitude
Longitude
50
45
40
35
130
135
140
0
1
2
3
4
5
6
7
8
9
10
11
12
Temperature (°C)

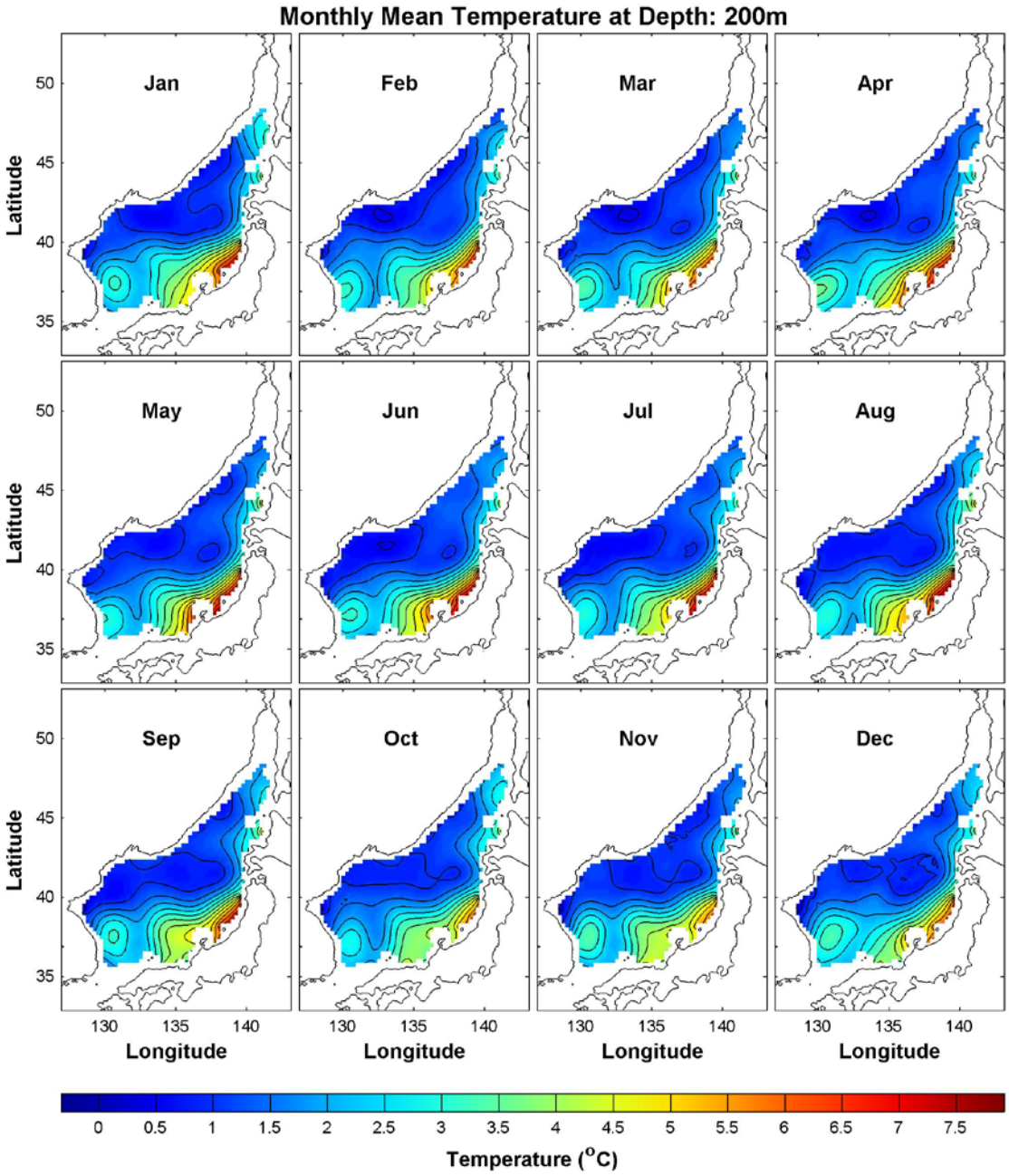
Monthly Mean Temperature at Depth: 200m
Jan
Feb
Mar
Apr
May
Jun
Jul
Aug
Sep
Oct
Nov
Dec
Latitude
Longitude
50
45
40
35
130
135
140
0
0.5
1
1.5
2
2.5
3
3.5
4
4.5
5
5.5
6
6.5
7
7.5
Temperature (°C)

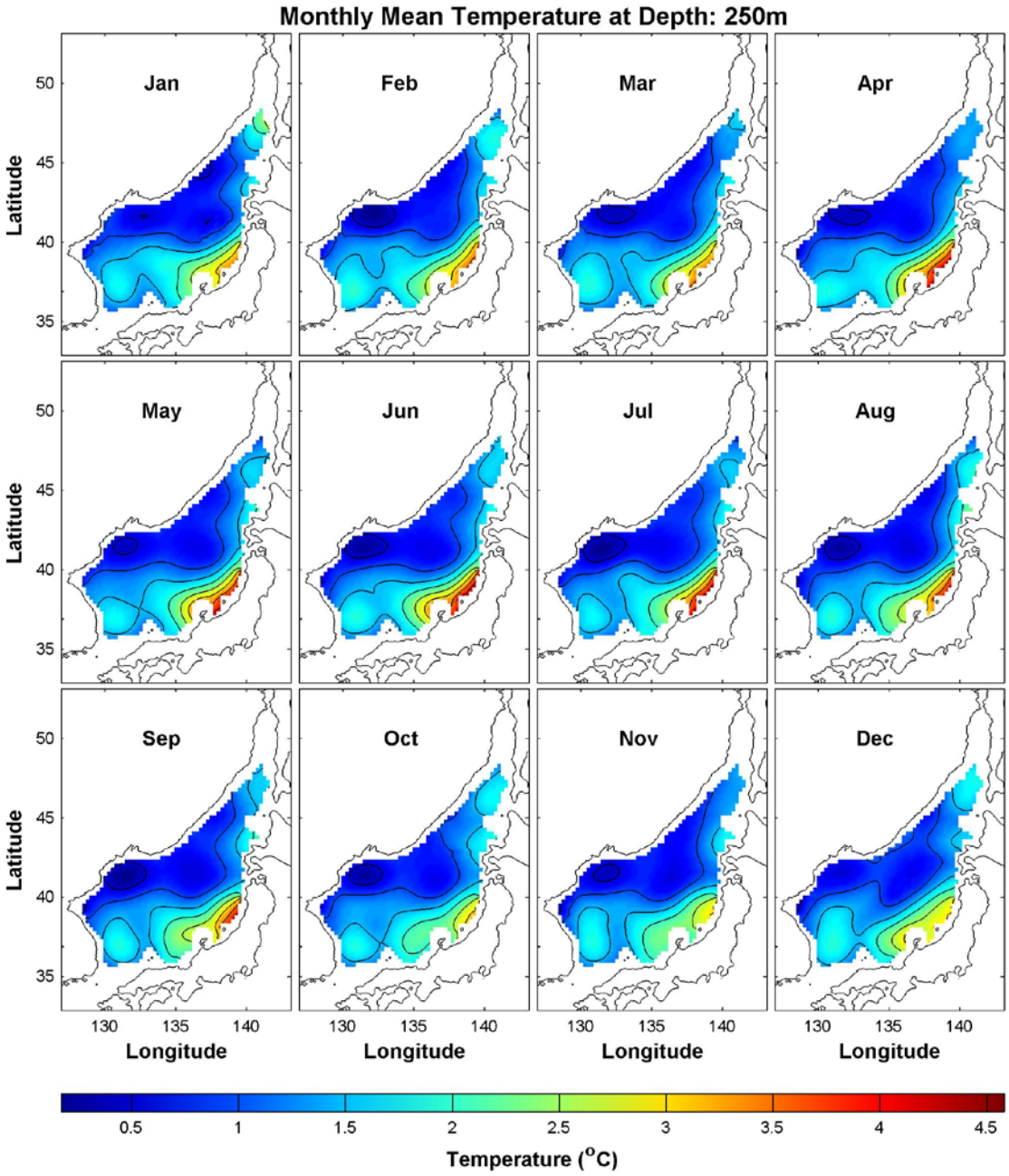
Monthly Mean Temperature at Depth: 250m
Jan
Feb
Mar
Apr
May
Jun
Jul
Aug
Sep
Oct
Nov
Dec
Latitude
Longitude
50
45
40
35
130
135
140
0.5
1
1.5
2
2.5
3
3.5
4
4.5
Temperature (°C)

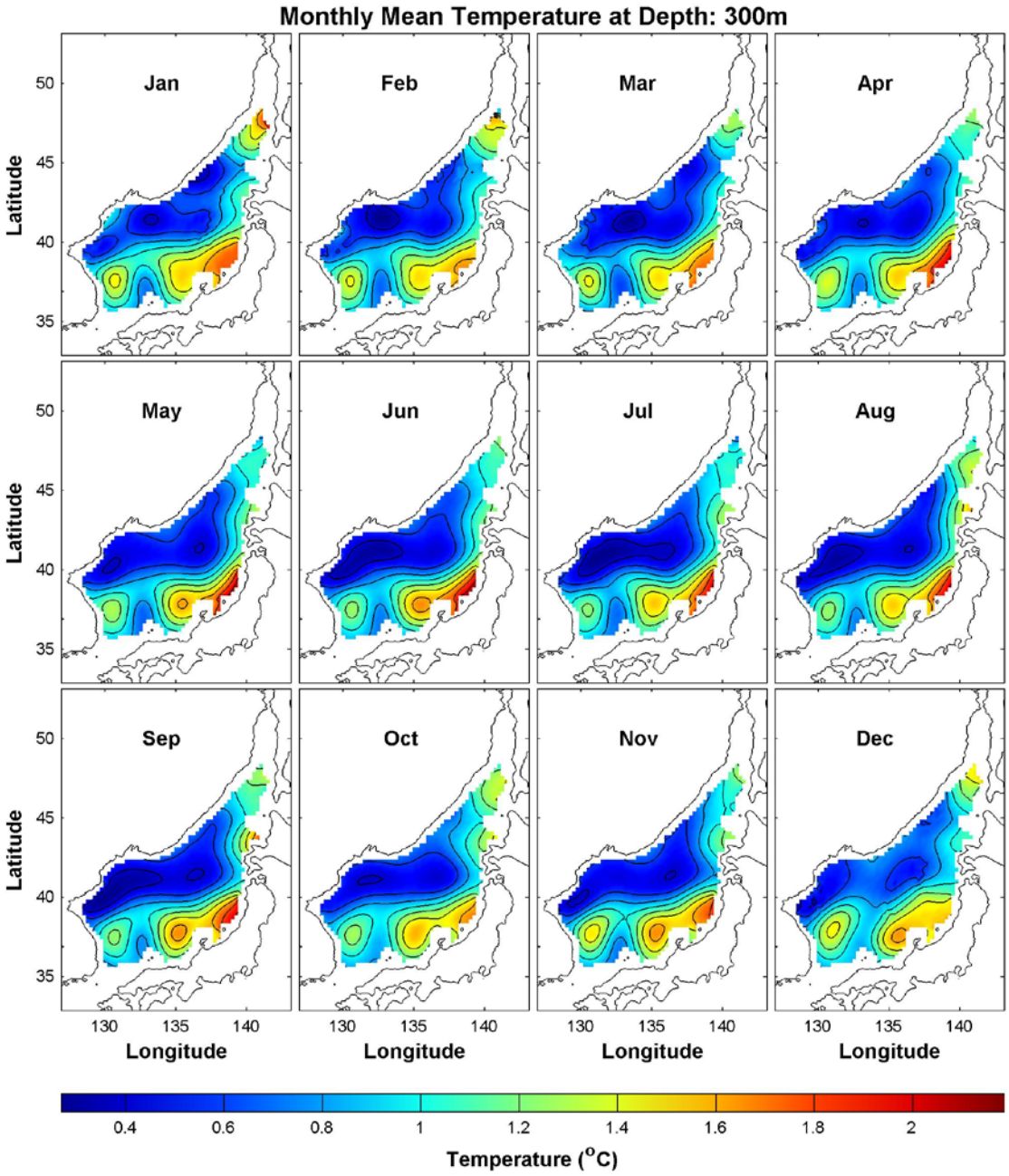
Monthly Mean Temperature at Depth: 300m
Jan
Feb
Mar
Apr
May
Jun
Jul
Aug
Sep
Oct
Nov
Dec
Latitude
Longitude
50
45
40
35
130
135
140
0.4
0.6
0.8
1
1.2
1.4
1.6
1.8
2
Temperature (°C)

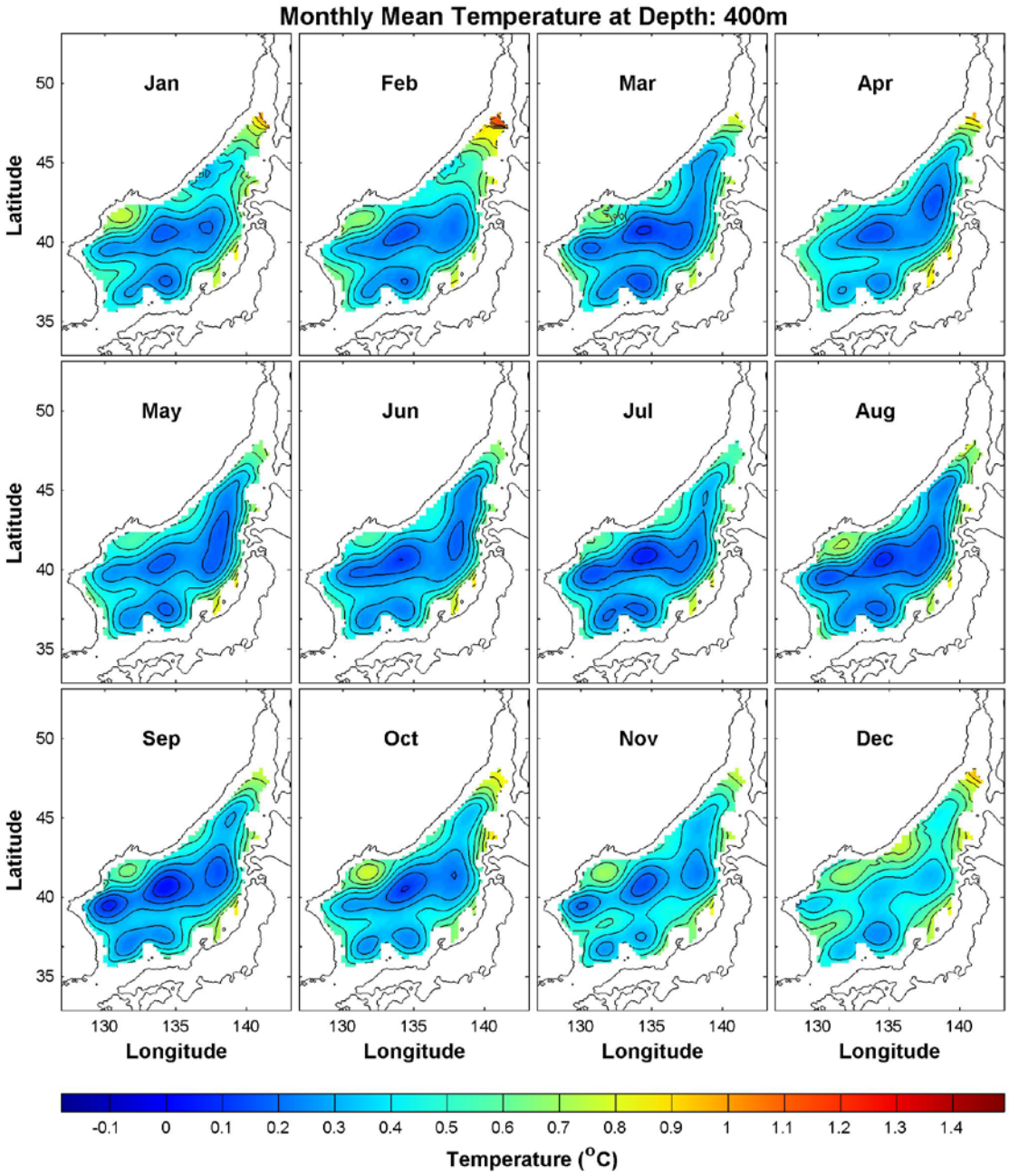
Monthly Mean Temperature at Depth: 400m
Jan
Feb
Mar
Apr
May
Jun
Jul
Aug
Sep
Oct
Nov
Dec
Latitude
Longitude
50
45
40
35
130
135
140
-0.1
0
0.1
0.2
0.3
0.4
0.5
0.6
0.7
0.8
0.9
1
1.1
1.2
1.3
1.4
Temperature (°C)

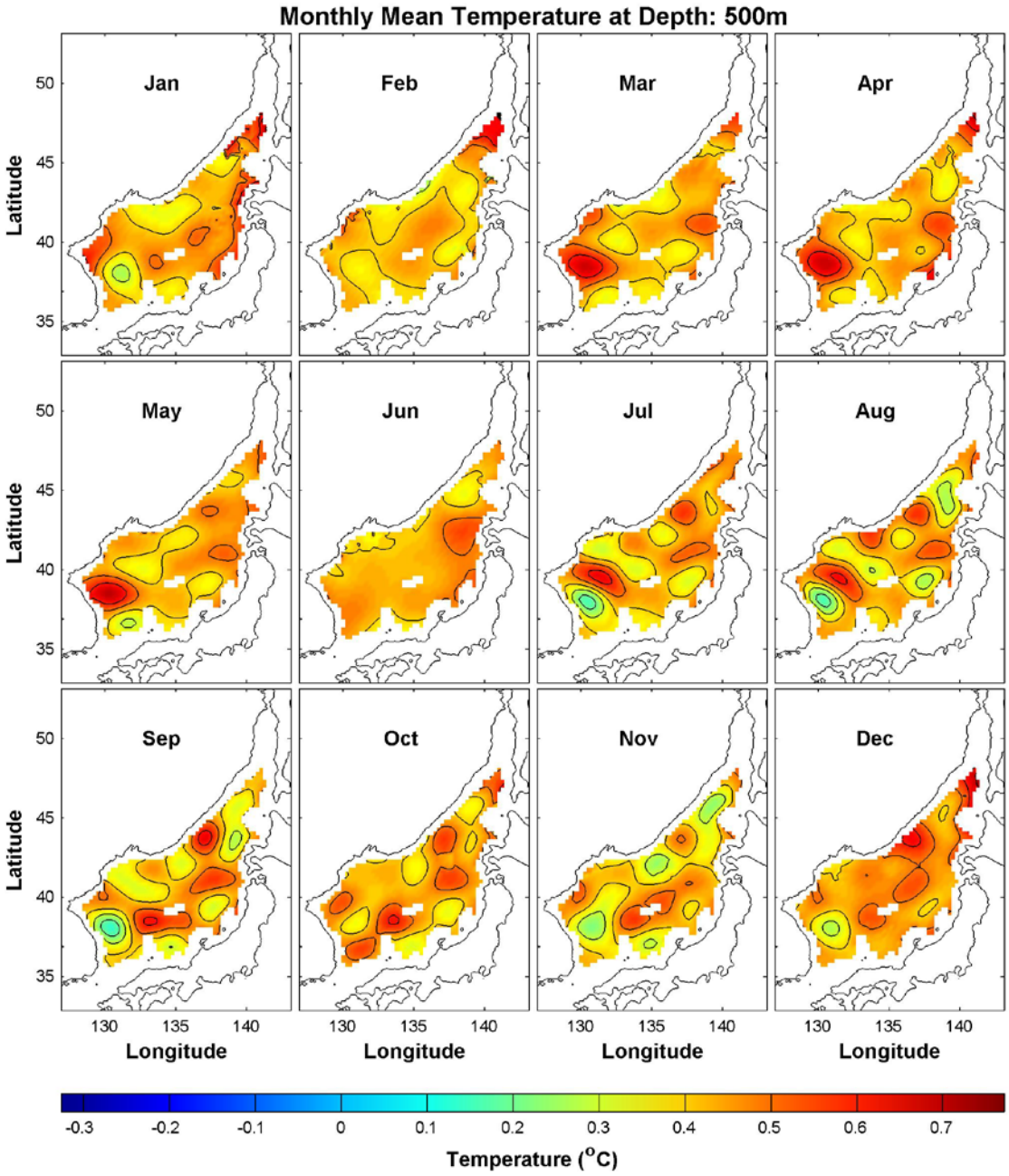
Monthly Mean Temperature at Depth: 500m
Jan
Feb
Mar
Apr
May
Jun
Jul
Aug
Sep
Oct
Nov
Dec
Latitude
Longitude
50
45
40
35
130
135
140
-0.3
-0.2
-0.1
0
0.1
0.2
0.3
0.4
0.5
0.6
0.7
Temperature (°C)

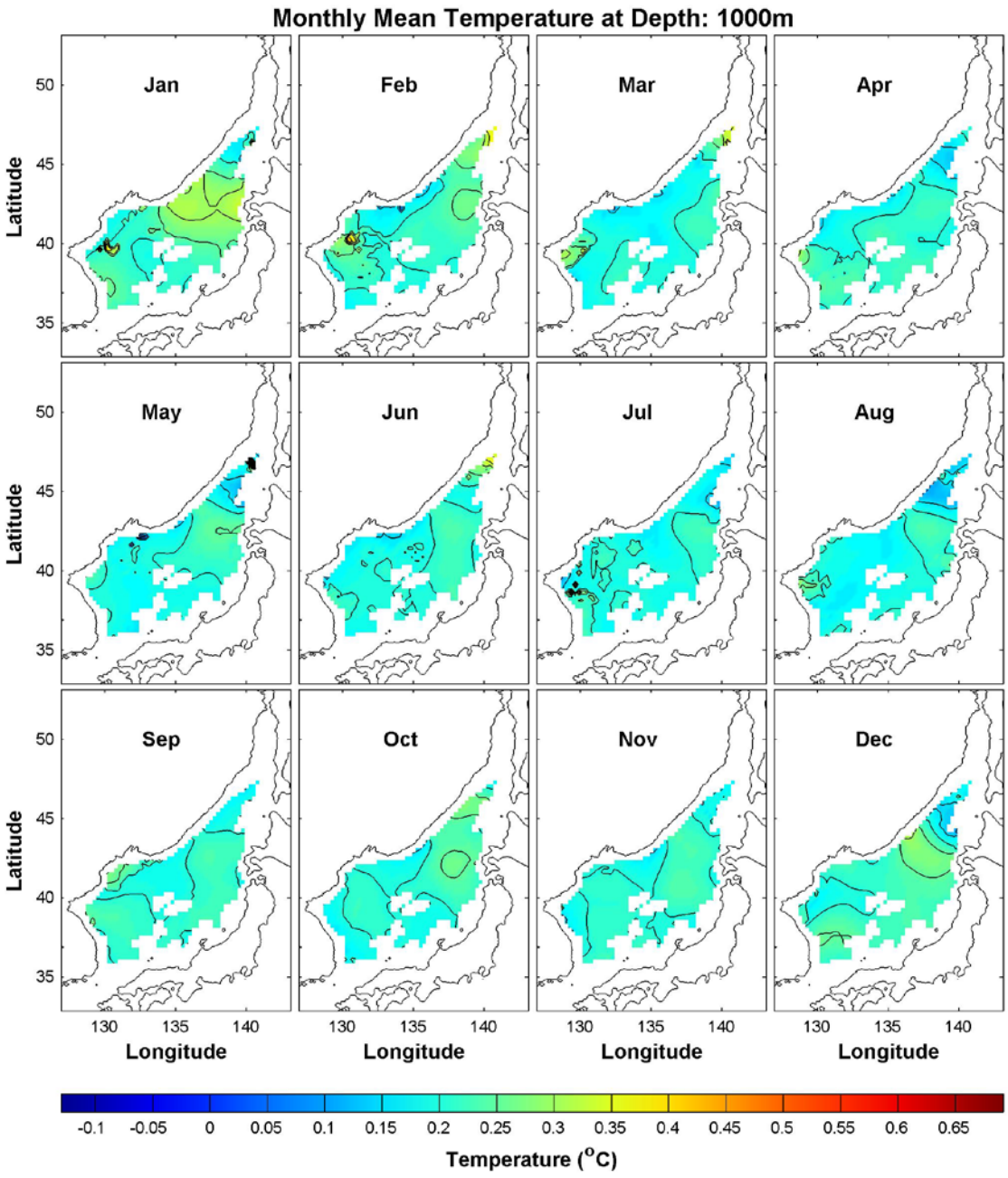
Monthly Mean Temperature at Depth: 1000m
Jan
Feb
Mar
Apr
May
Jun
Jul
Aug
Sep
Oct
Nov
Dec
Latitude
Longitude
50
45
40
35
130
135
140
-0.1
-0.05
0
0.05
0.1
0.15
0.2
0.25
0.3
0.35
0.4
0.45
0.5
0.55
0.6
0.65
Temperature (°C)

B. SALINITY

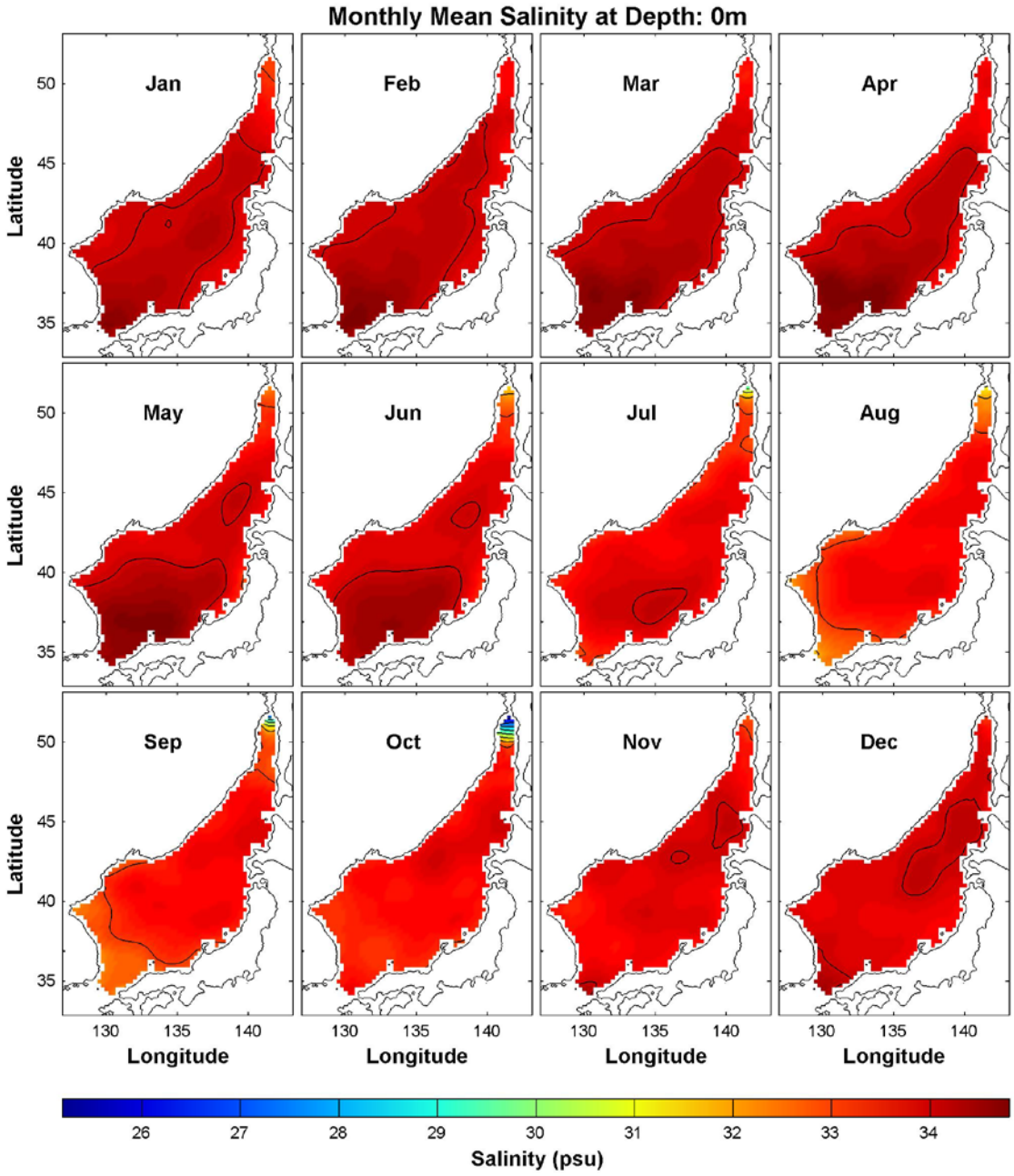
Monthly Mean Salinity at Depth: 0m
Jan
Feb
Mar
Apr
May
Jun
Jul
Aug
Sep
Oct
Nov
Dec
Latitude
Longitude
50
45
40
35
130
135
140
26
27
28
29
30
31
32
33
34
Salinity (psu)

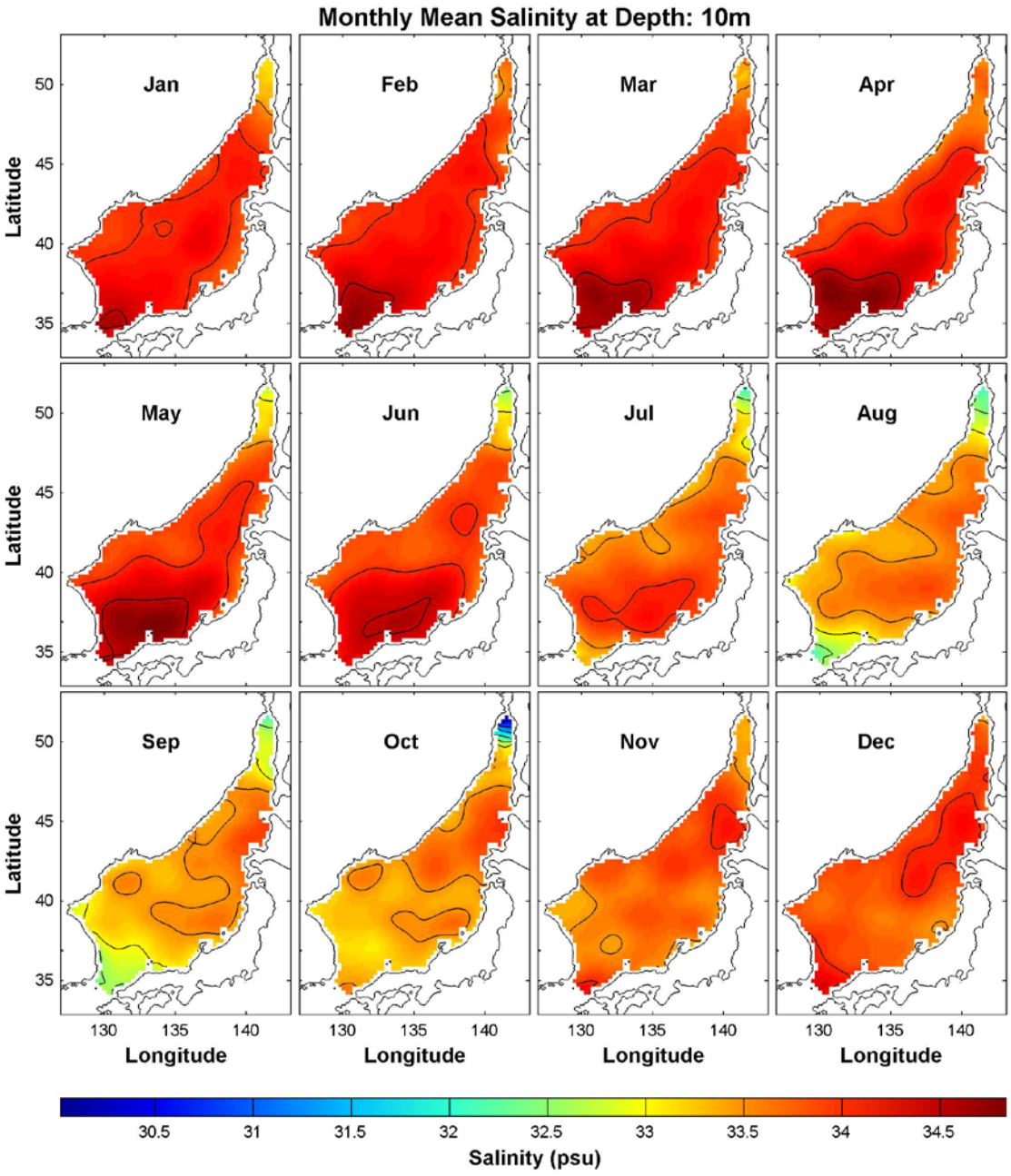
Monthly Mean Salinity at Depth: 10m
Jan
Feb
Mar
Apr
May
Jun
Jul
Aug
Sep
Oct
Nov
Dec
Latitude
Longitude
50
45
40
35
130
135
140
30.5
31
31.5
32
32.5
33
33.5
34
34.5
Salinity (psu)

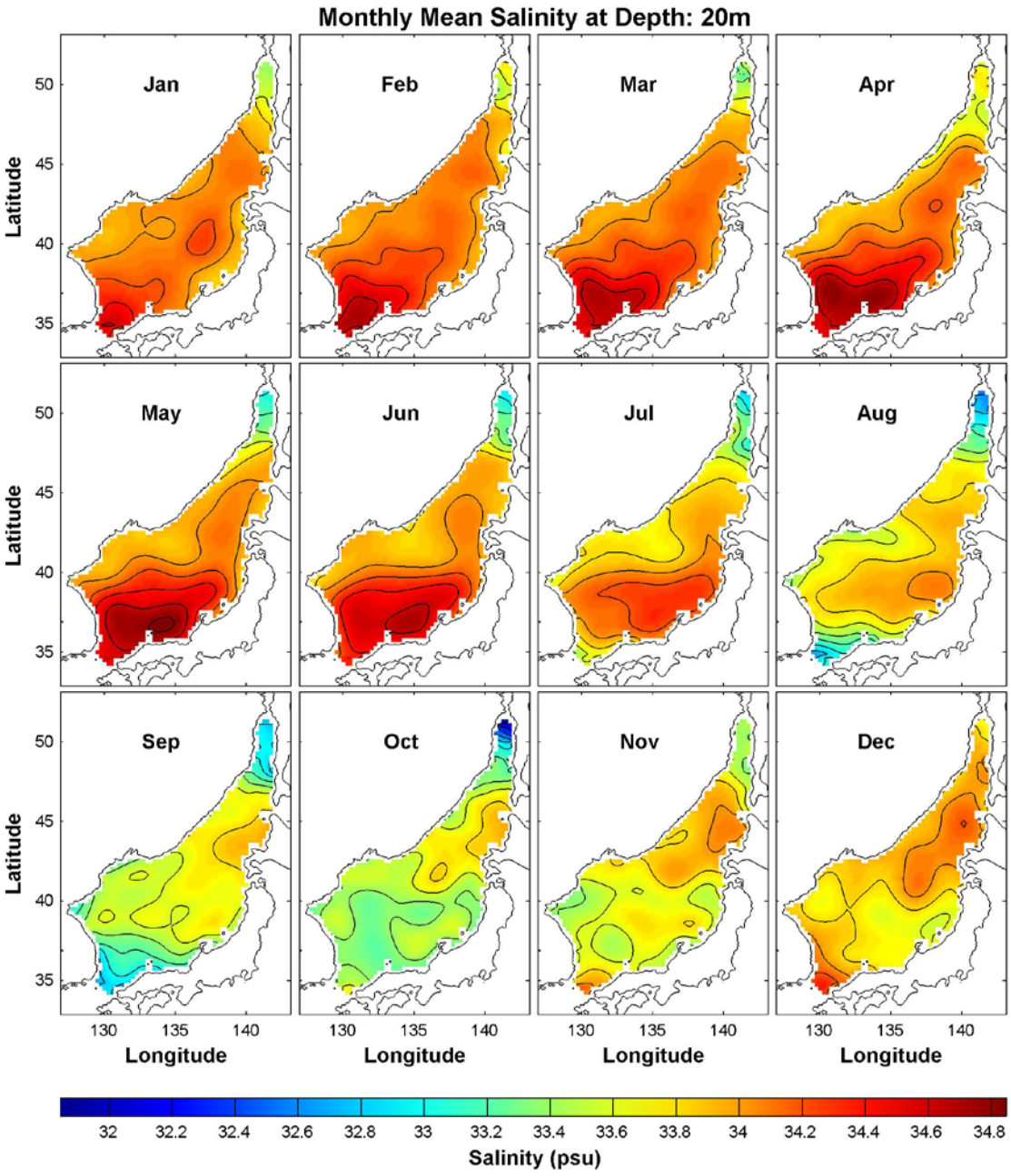
Monthly Mean Salinity at Depth: 20m
Jan
Feb
Mar
Apr
May
Jun
Jul
Aug
Sep
Oct
Nov
Dec
Latitude
Longitude
50
45
40
35
130
135
140
32
32.2
32.4
32.6
32.8
33
33.2
33.4
33.6
33.8
34
34.2
34.4
34.6
34.8
Salinity (psu)

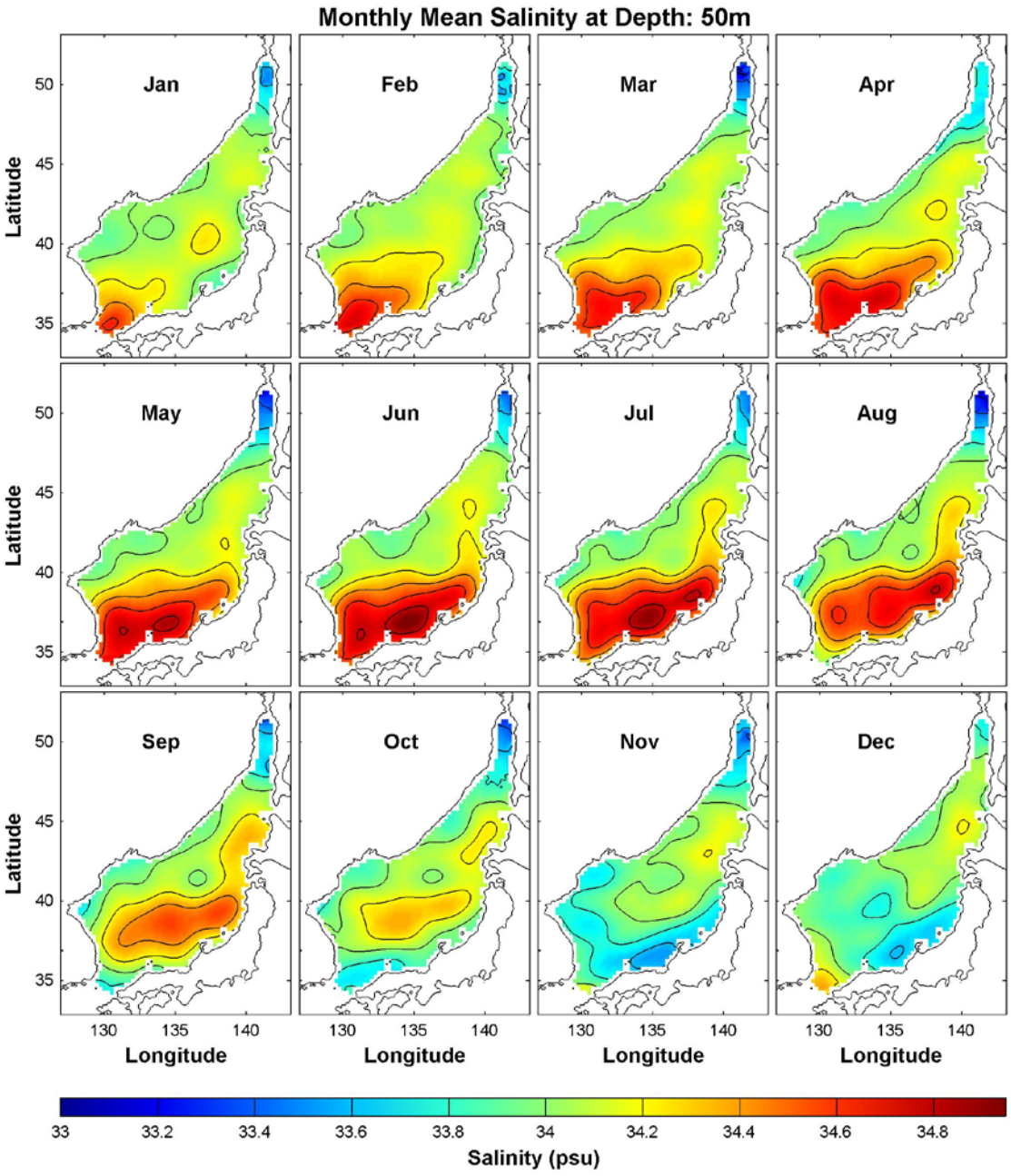
Monthly Mean Salinity at Depth: 50m
Jan
Feb
Mar
Apr
May
Jun
Jul
Aug
Sep
Oct
Nov
Dec
Latitude
Longitude
50
45
40
35
130
135
140
33
33.2
33.4
33.6
33.8
34
34.2
34.4
34.6
34.8
Salinity (psu)

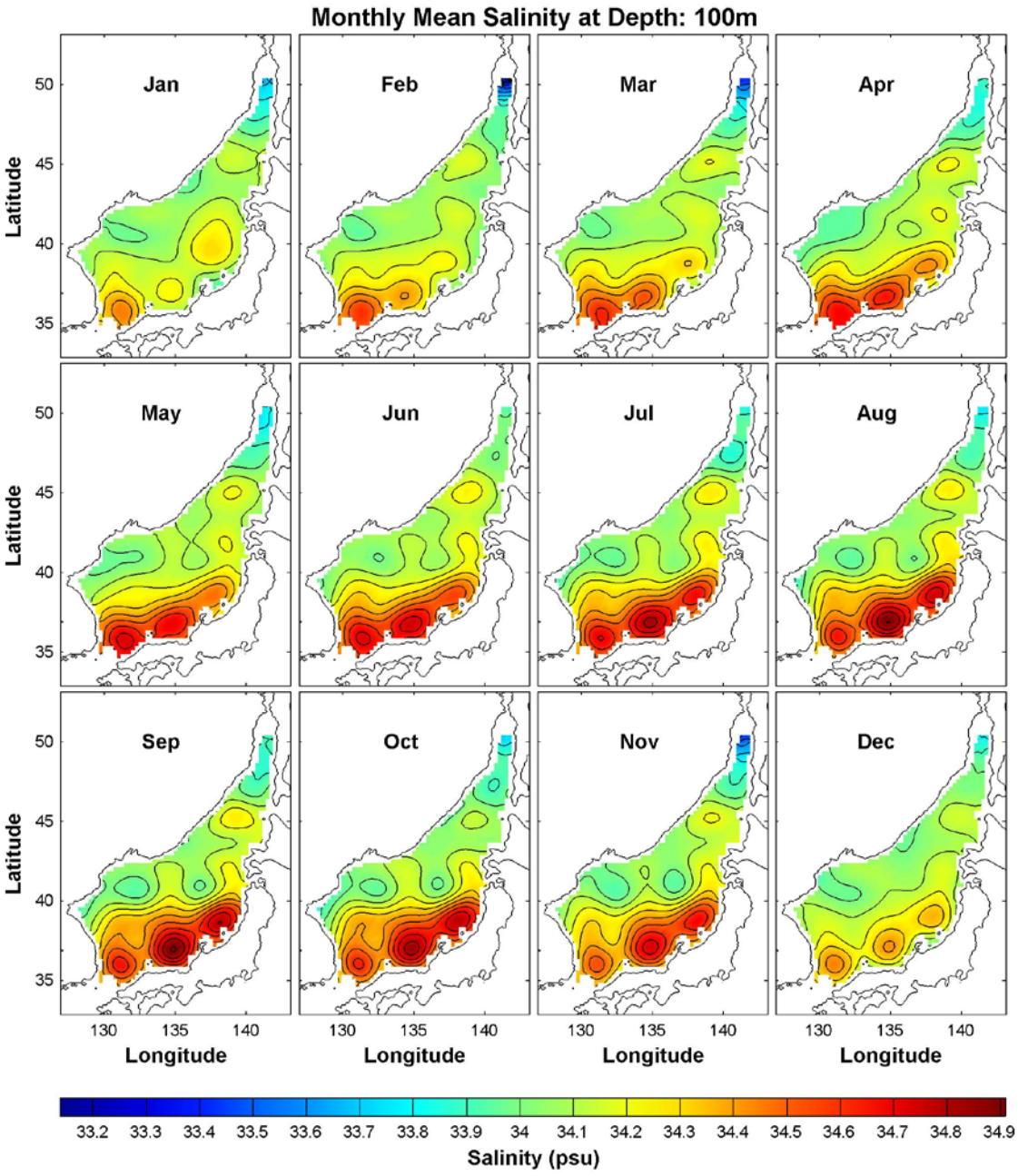
Monthly Mean Salinity at Depth: 100m
Jan
Feb
Mar
Apr
May
Jun
Jul
Aug
Sep
Oct
Nov
Dec
Latitude
Longitude
50
45
40
35
130
135
140
33.2
33.3
33.4
33.5
33.6
33.7
33.8
33.9
34
34.1
34.2
34.3
34.4
34.5
34.6
34.7
34.8
34.9
Salinity (psu)

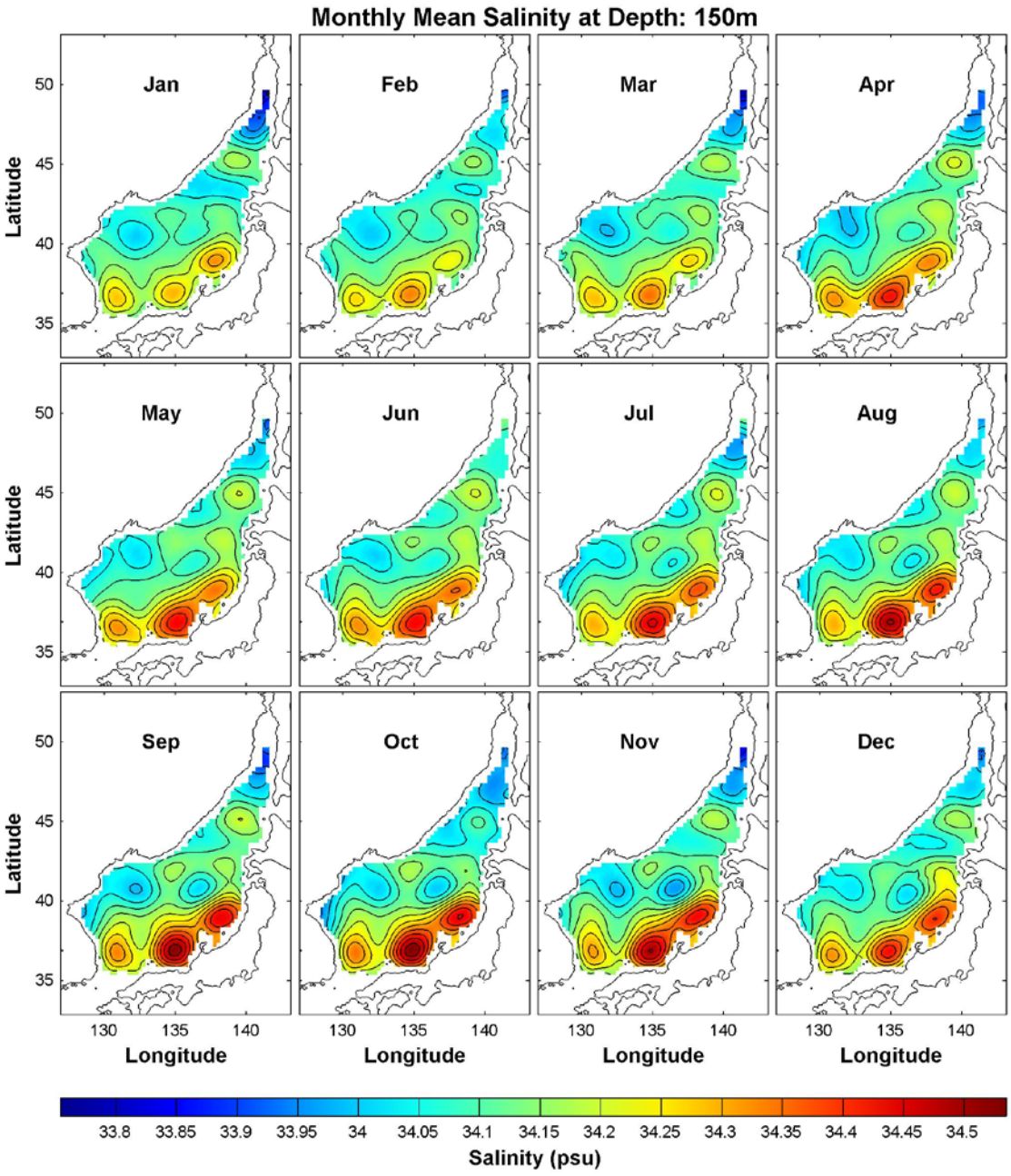
Monthly Mean Salinity at Depth: 150m
Jan
Feb
Mar
Apr
May
Jun
Jul
Aug
Sep
Oct
Nov
Dec
Latitude
Longitude
50
45
40
35
130
135
140
33.8
33.85
33.9
33.95
34
34.05
34.1
34.15
34.2
34.25
34.3
34.35
34.4
34.45
34.5
Salinity (psu)

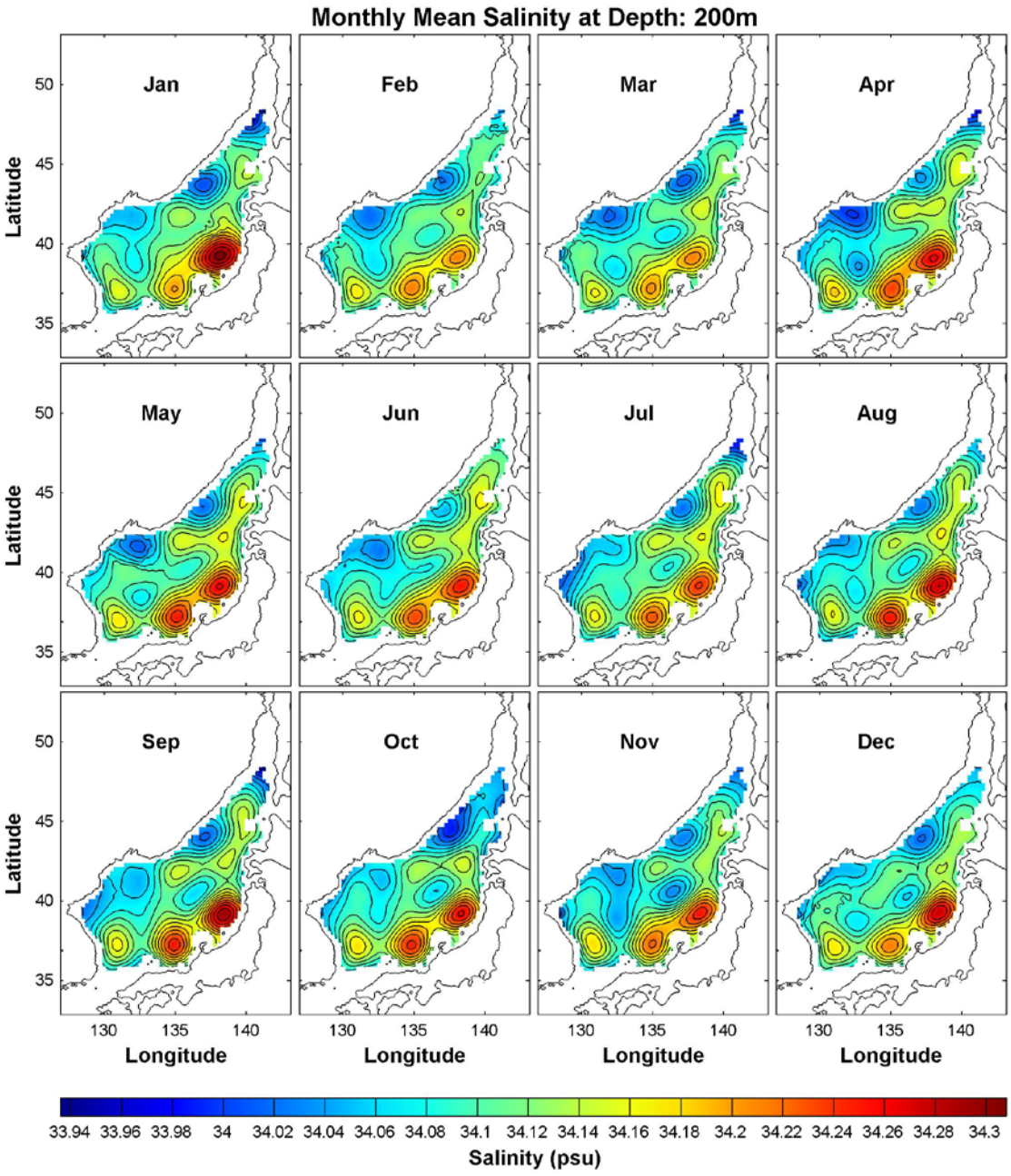
Monthly Mean Salinity at Depth: 200m
Jan
Feb
Mar
Apr
May
Jun
Jul
Aug
Sep
Oct
Nov
Dec
Latitude
Longitude
50
45
40
35
130
135
140
33.94 33.96 33.98 34 34.02 34.04 34.06 34.08 34.1 34.12 34.14 34.16 34.18 34.2 34.22 34.24 34.26 34.28 34.3
Salinity (psu)

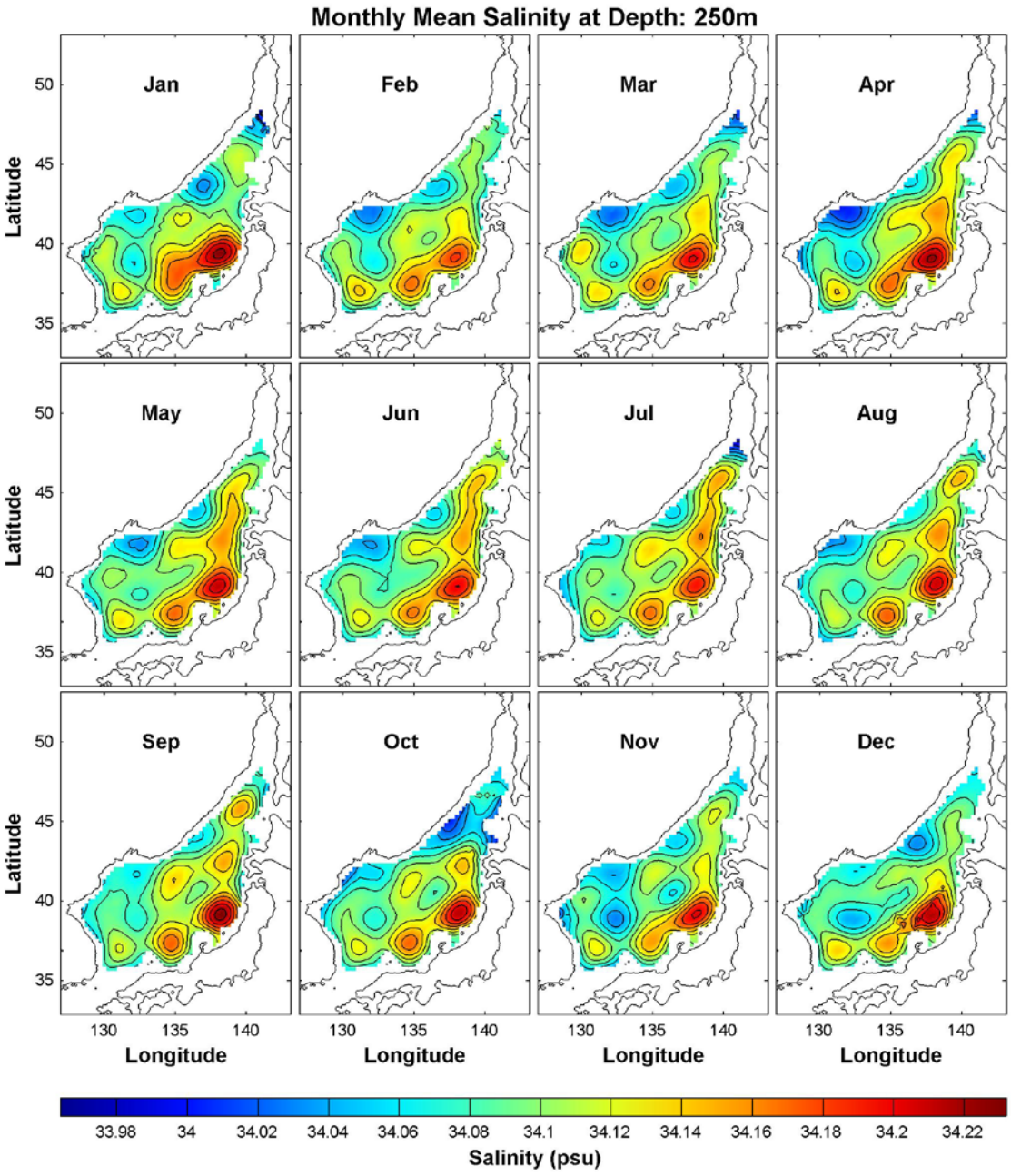
Monthly Mean Salinity at Depth: 250m
Jan
Feb
Mar
Apr
May
Jun
Jul
Aug
Sep
Oct
Nov
Dec
Latitude
Longitude
50
45
40
35
130
135
140
33.98
34
34.02
34.04
34.06
34.08
34.1
34.12
34.14
34.16
34.18
34.2
34.22
Salinity (psu)

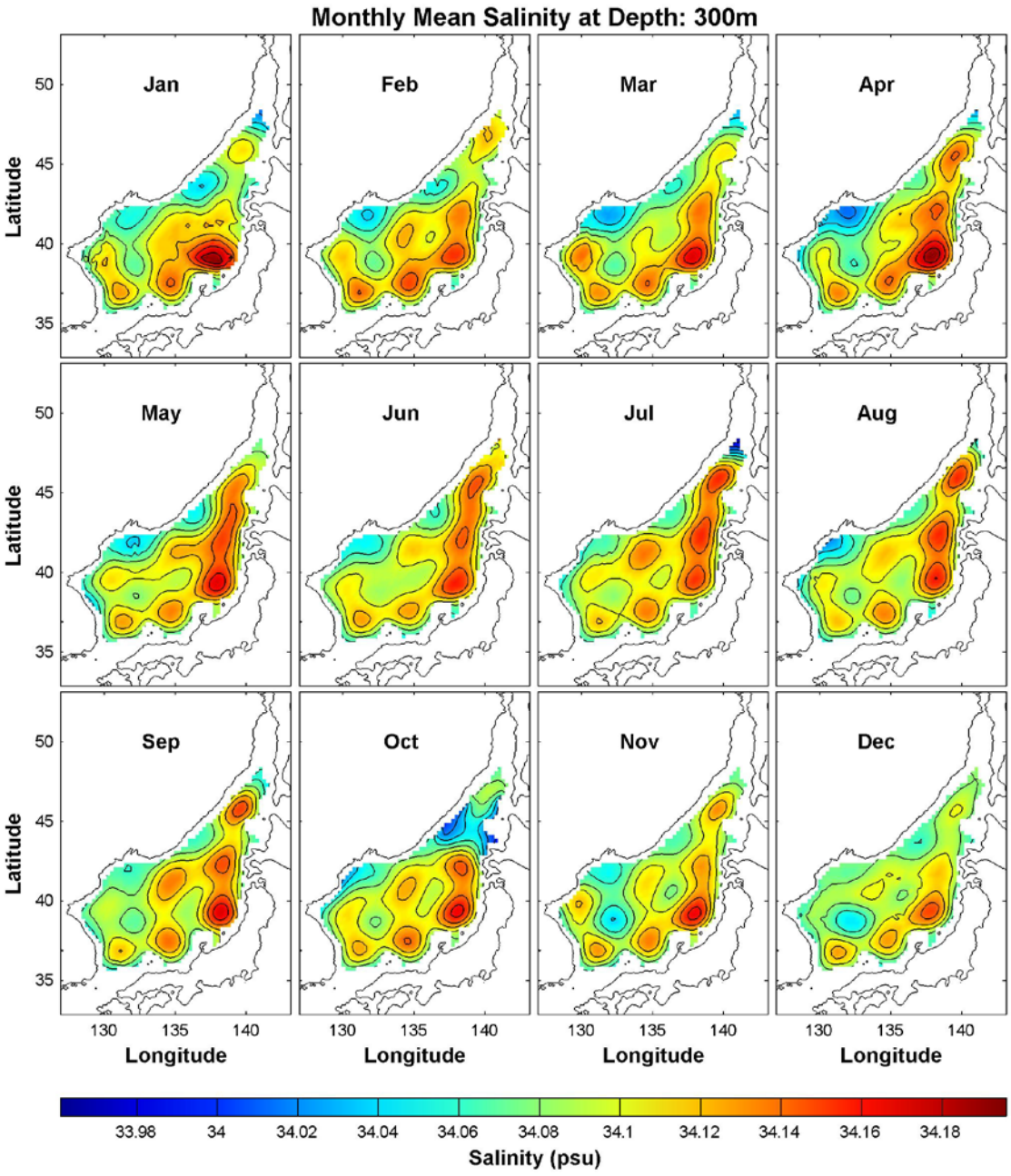
Monthly Mean Salinity at Depth: 300m
Jan
Feb
Mar
Apr
May
Jun
Jul
Aug
Sep
Oct
Nov
Dec
Latitude
Longitude
50
45
40
35
130
135
140
33.98
34
34.02
34.04
34.06
34.08
34.1
34.12
34.14
34.16
34.18
Salinity (psu)

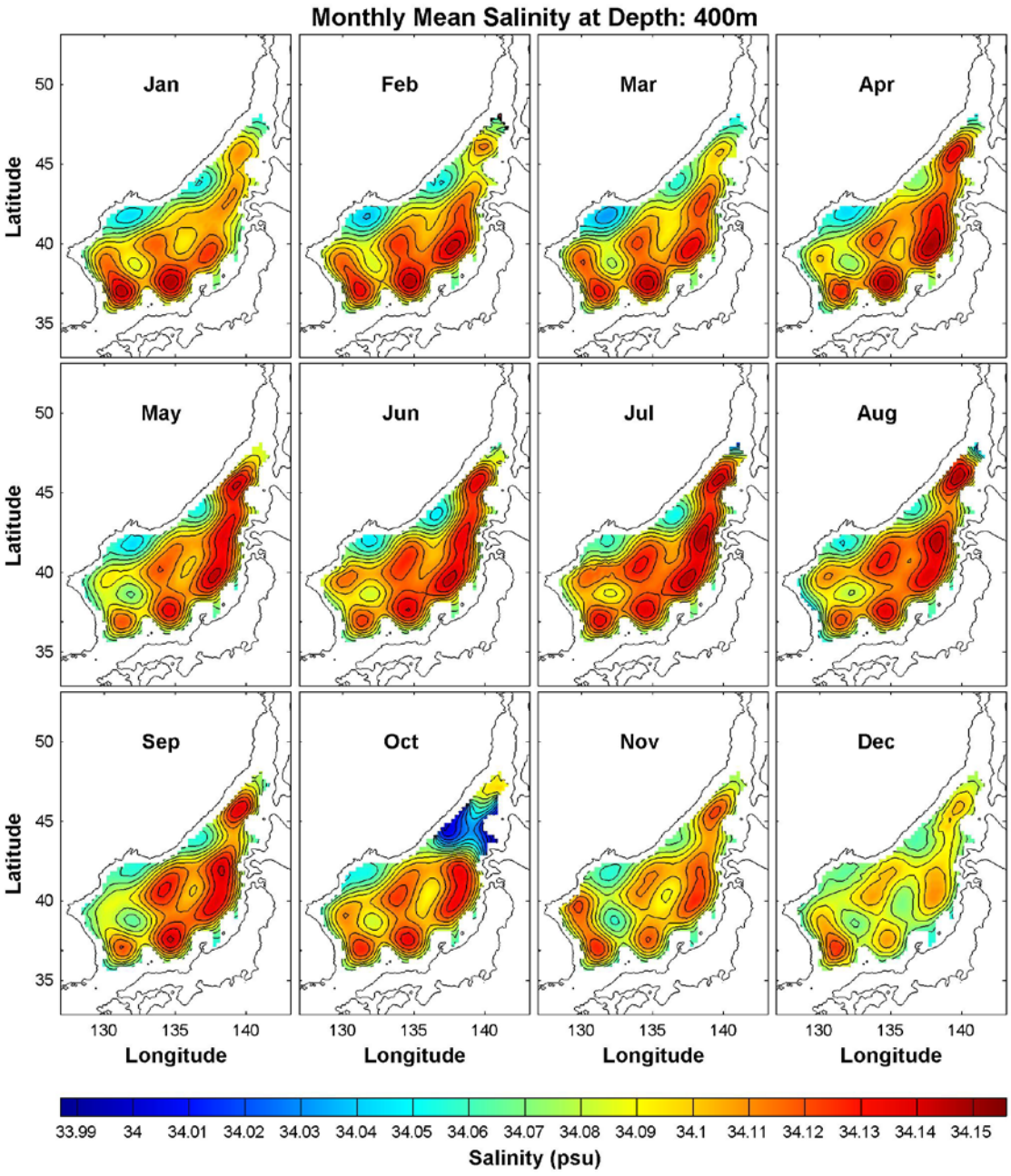
Monthly Mean Salinity at Depth: 400m
Jan
Feb
Mar
Apr
May
Jun
Jul
Aug
Sep
Oct
Nov
Dec
Latitude
Longitude
50
45
40
35
130
135
140
33.99
34
34.01
34.02
34.03
34.04
34.05
34.06
34.07
34.08
34.09
34.1
34.11
34.12
34.13
34.14
34.15
Salinity (psu)

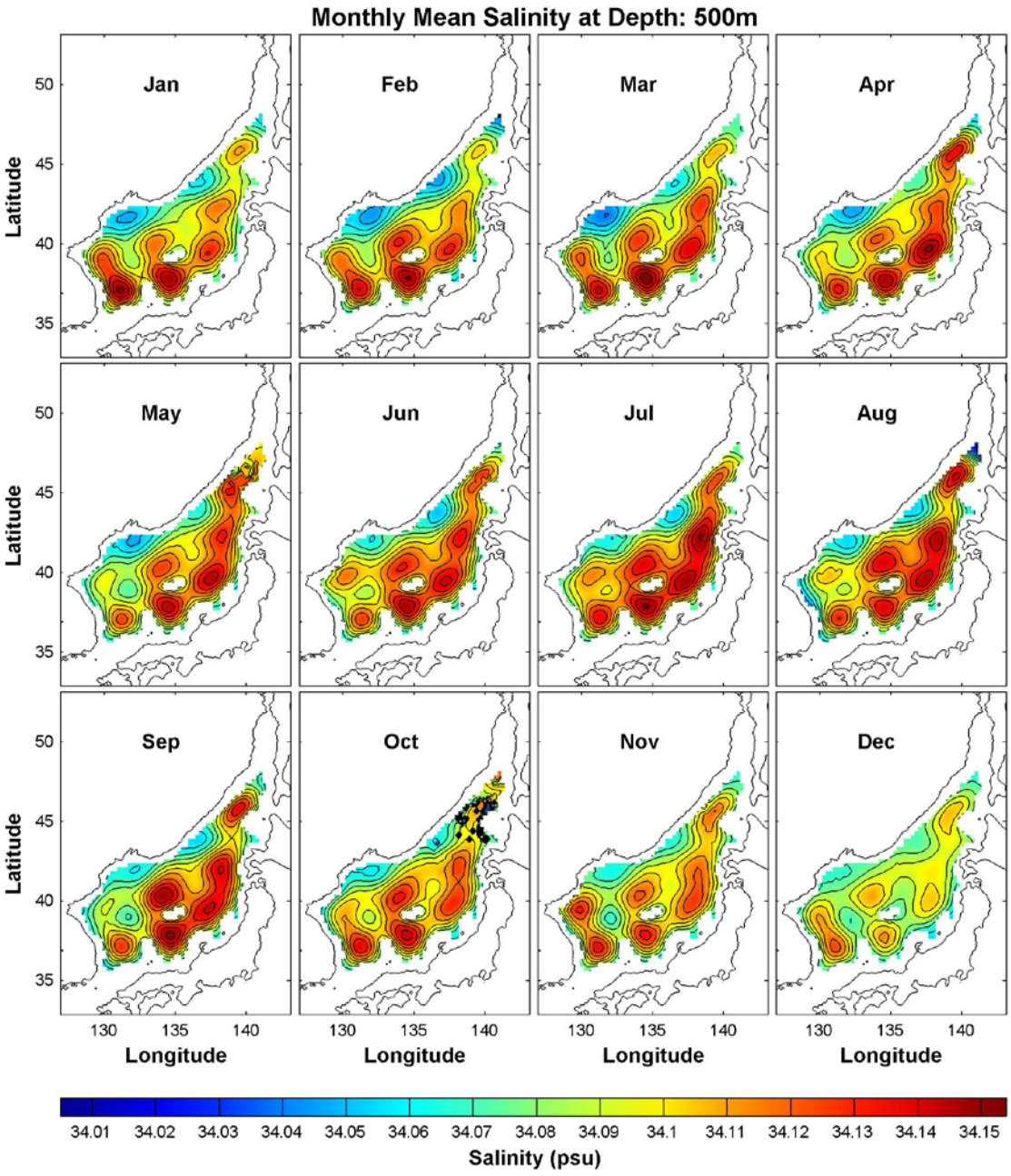
Monthly Mean Salinity at Depth: 500m
Jan
Feb
Mar
Apr
May
Jun
Jul
Aug
Sep
Oct
Nov
Dec
Latitude
Longitude
50
45
40
35
130
135
140
34.01
34.02
34.03
34.04
34.05
34.06
34.07
34.08
34.09
34.1
34.11
34.12
34.13
34.14
34.15
Salinity (psu)

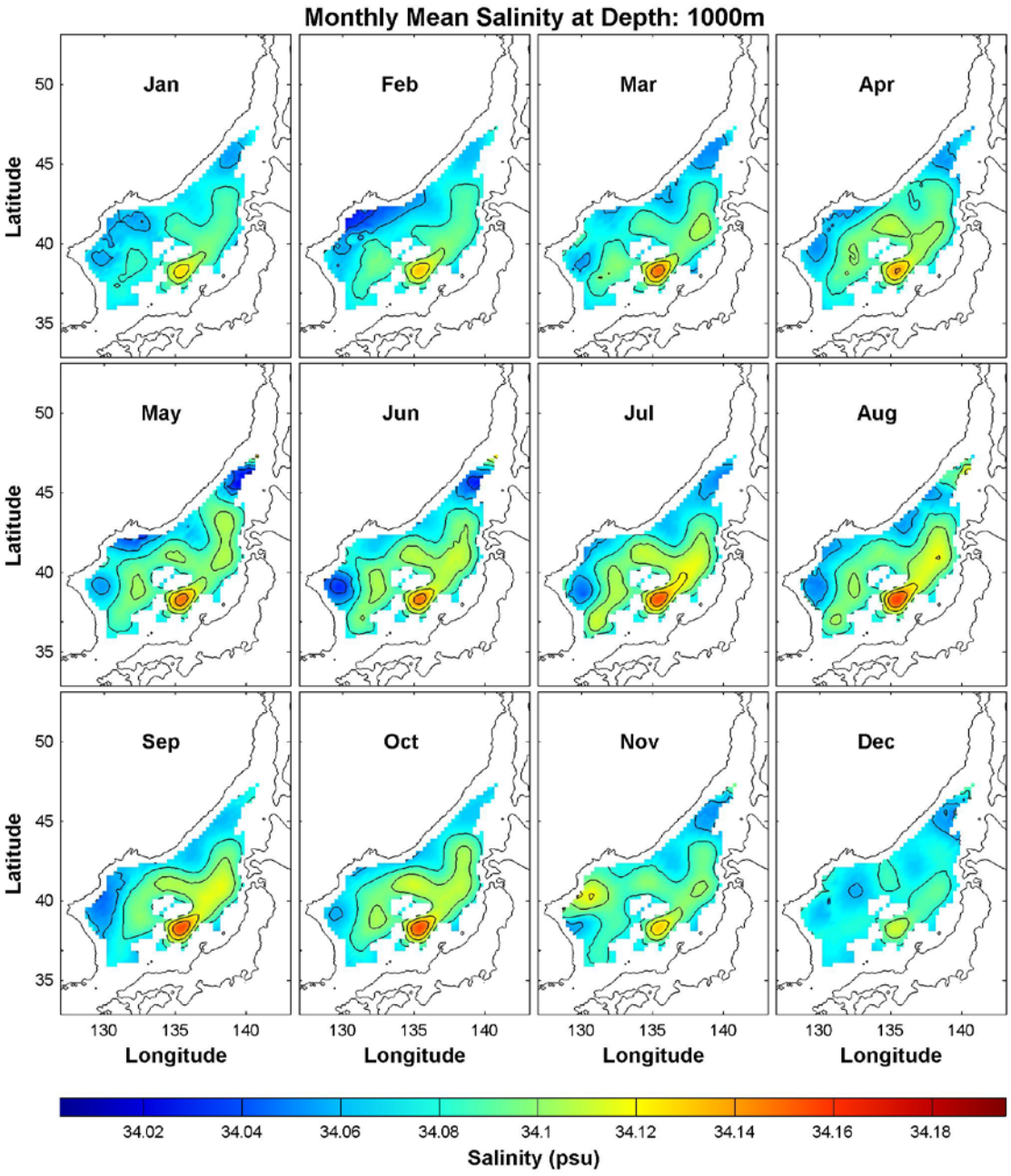
Monthly Mean Salinity at Depth: 1000m
Jan
Feb
Mar
Apr
May
Jun
Jul
Aug
Sep
Oct
Nov
Dec
Latitude
Longitude
50
45
40
35
130
135
140
34.02
34.04
34.06
34.08
34.1
34.12
34.14
34.16
34.18
Salinity (psu)

C. INTEGRATED ABSOLUTE GEOSTROPHIC VELOCITY (U,V)

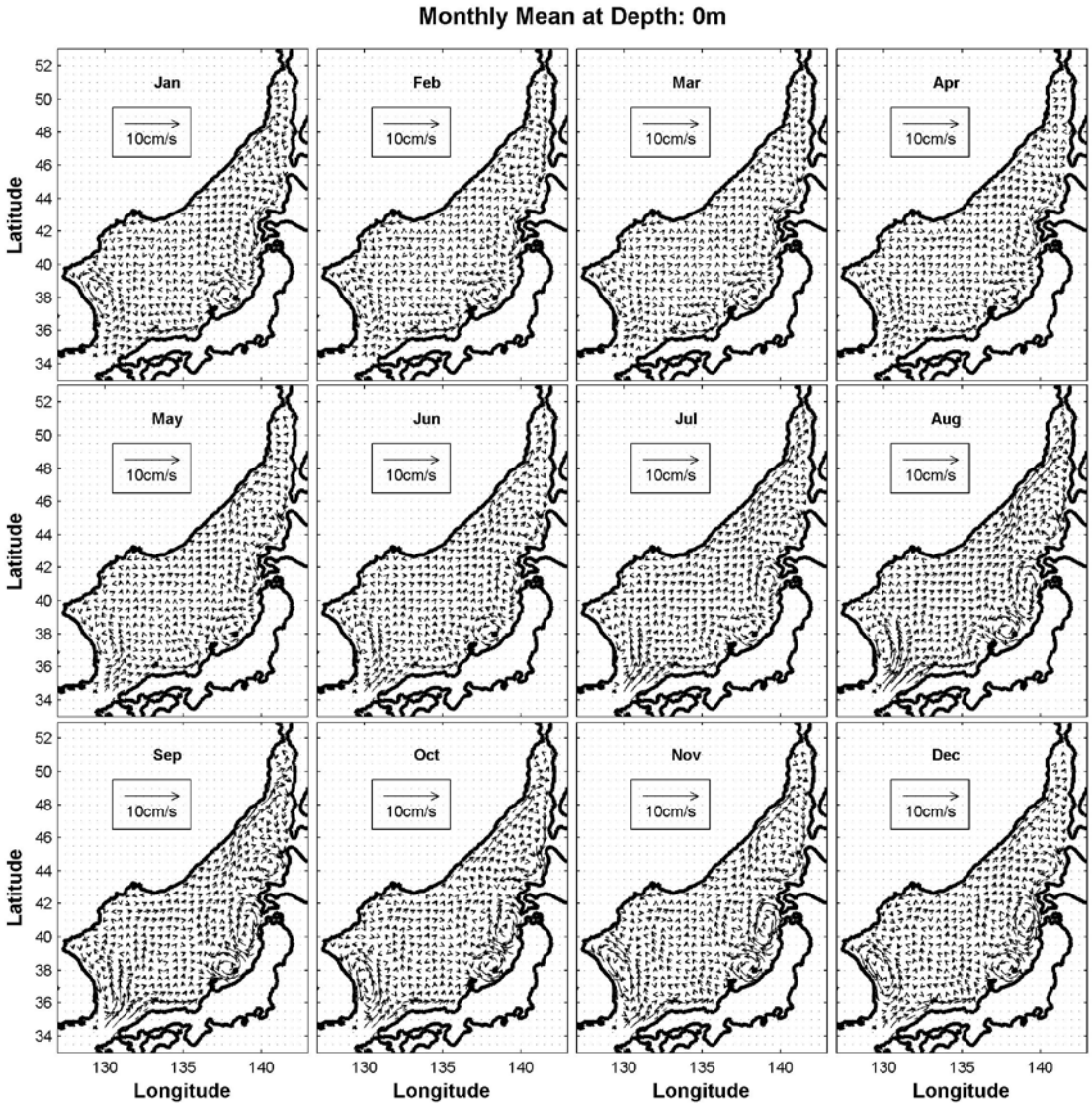

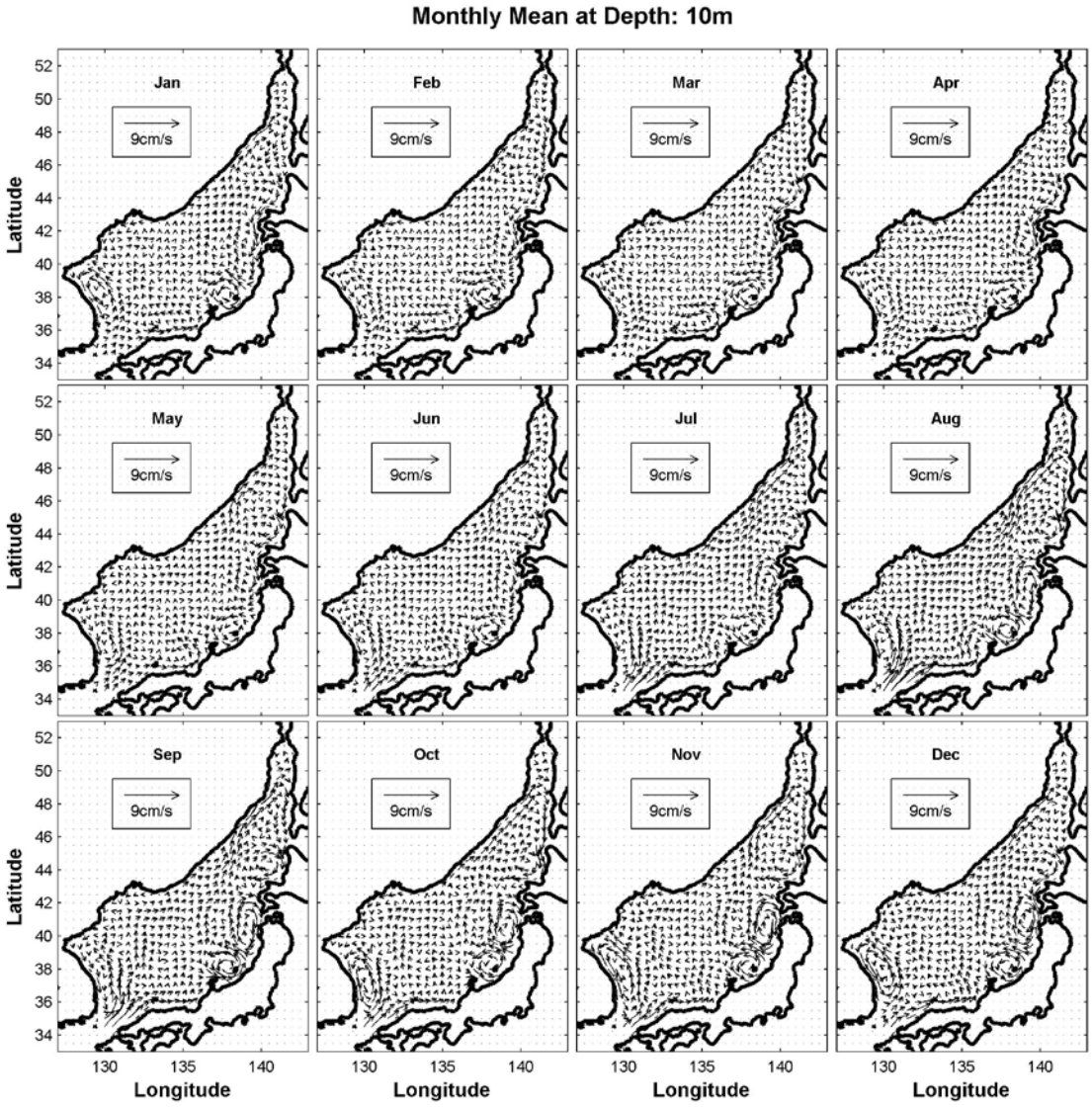
Monthly Mean at Depth: 10m
Jan
Feb
Mar
Apr
May
Jun
Jul
Aug
Sep
Oct
Nov
Dec
9cm/s
Latitude
Longitude
52
50
48
46
44
42
40
38
36
34
130
135
140

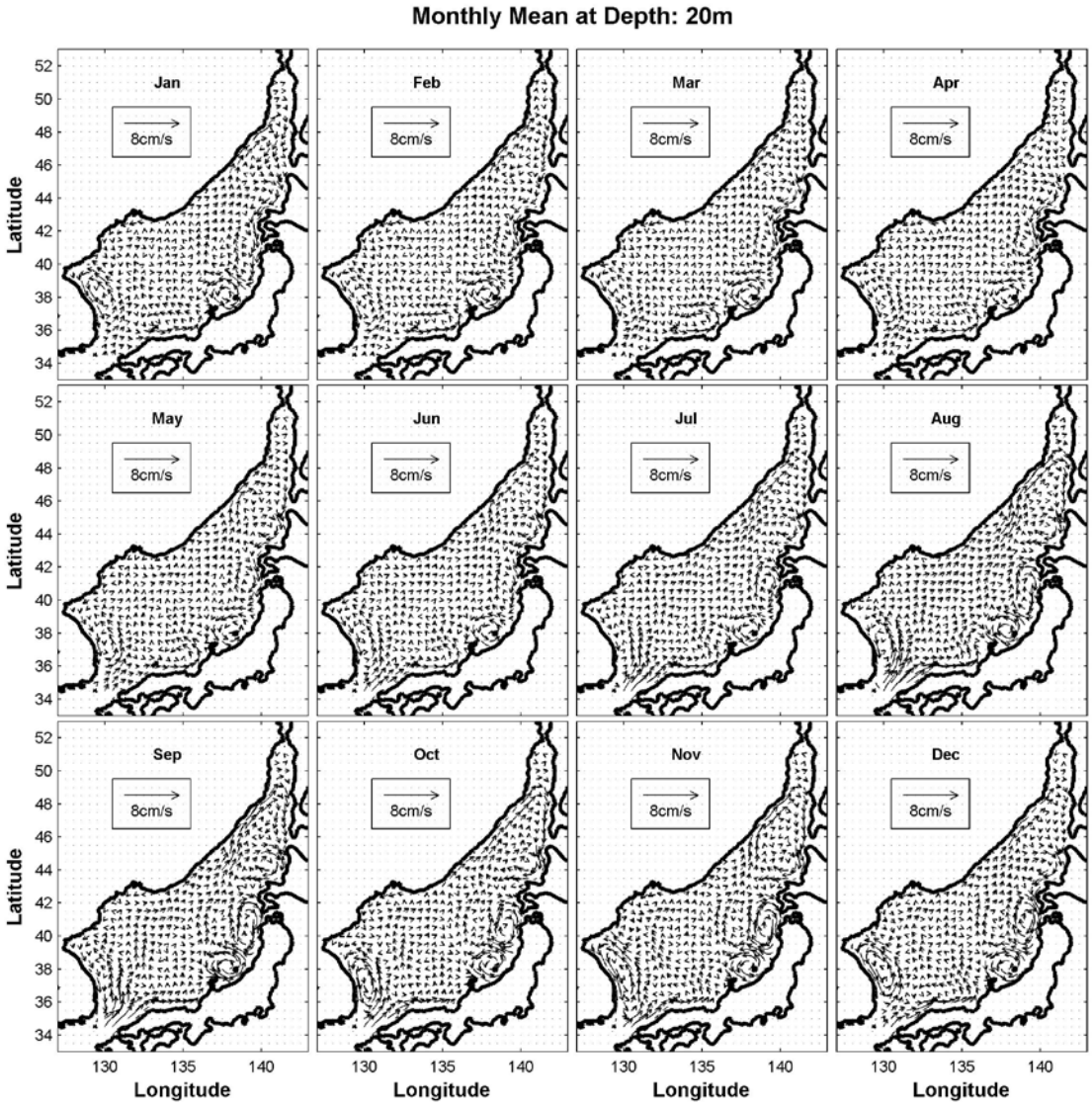
Monthly Mean at Depth: 20m
Jan
Feb
Mar
Apr
May
Jun
Jul
Aug
Sep
Oct
Nov
Dec
8cm/s
Latitude
Longitude
52
50
48
46
44
42
40
38
36
34
130
135
140

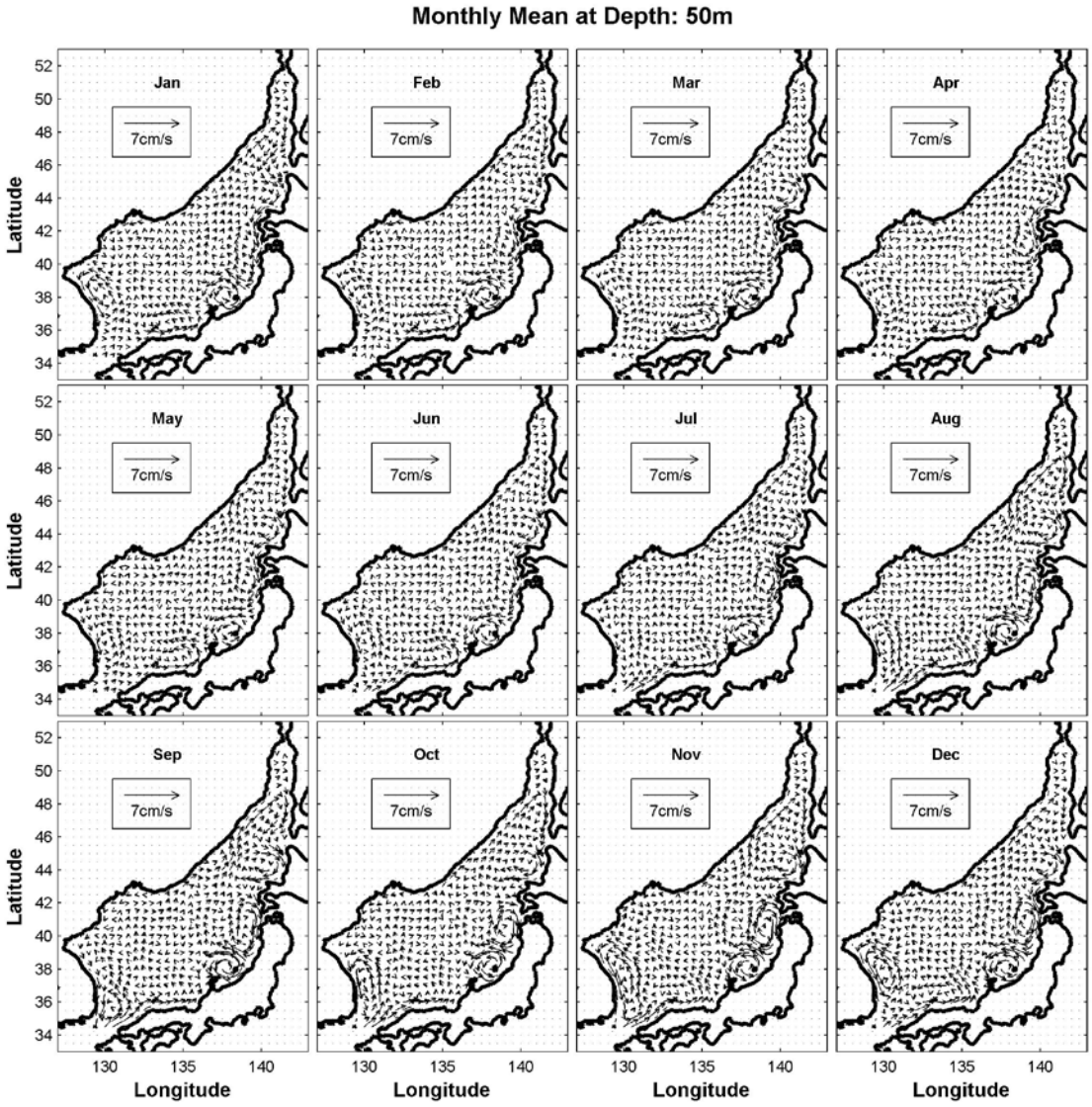
Monthly Mean at Depth: 50m
Jan
Feb
Mar
Apr
May
Jun
Jul
Aug
Sep
Oct
Nov
Dec
7cm/s
Latitude
Longitude
52
50
48
46
44
42
40
38
36
34
130
135
140

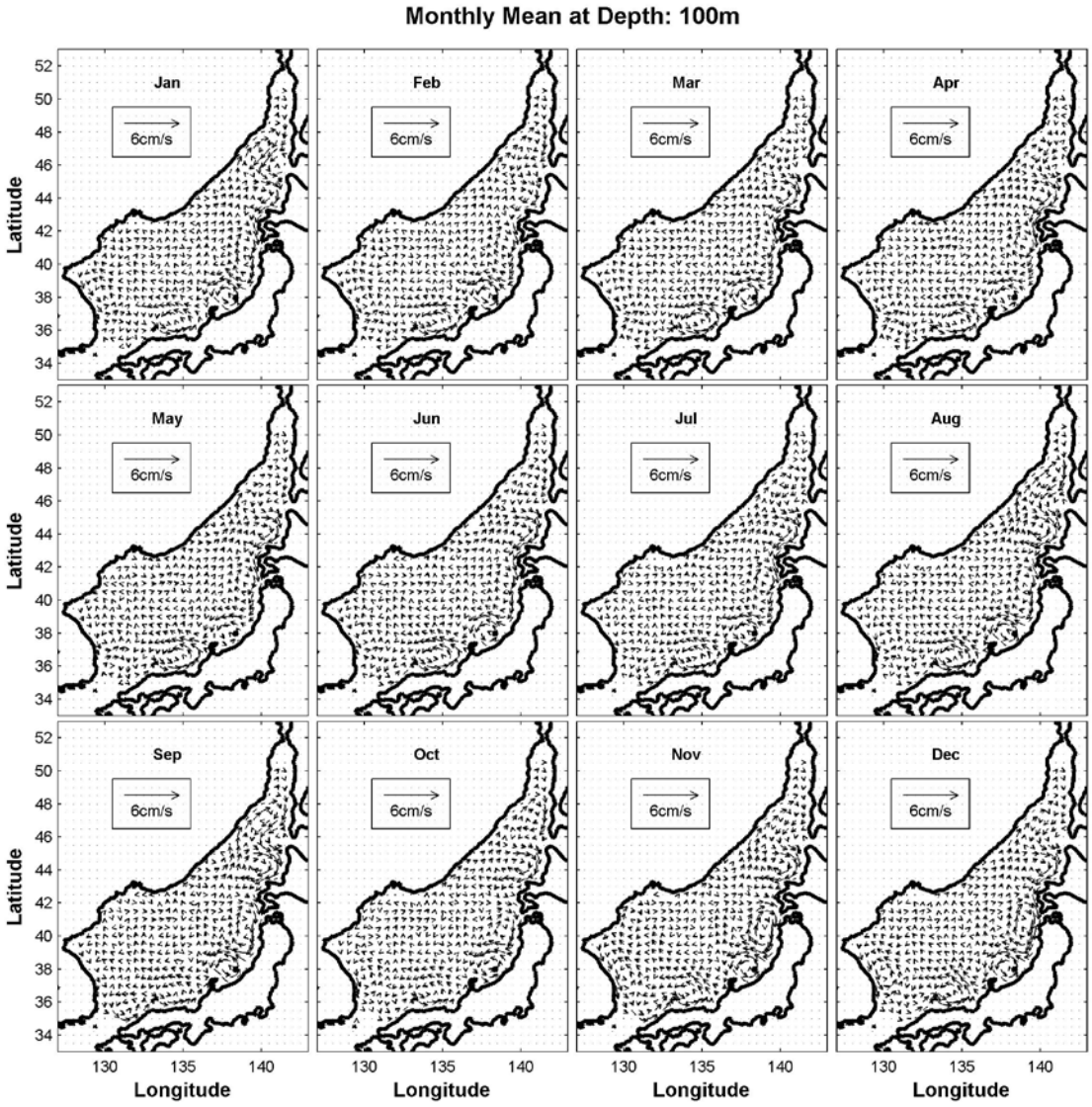
Monthly Mean at Depth: 100m
Jan
Feb
Mar
Apr
May
Jun
Jul
Aug
Sep
Oct
Nov
Dec
6cm/s
Latitude
Longitude
52
50
48
46
44
42
40
38
36
34
130
135
140

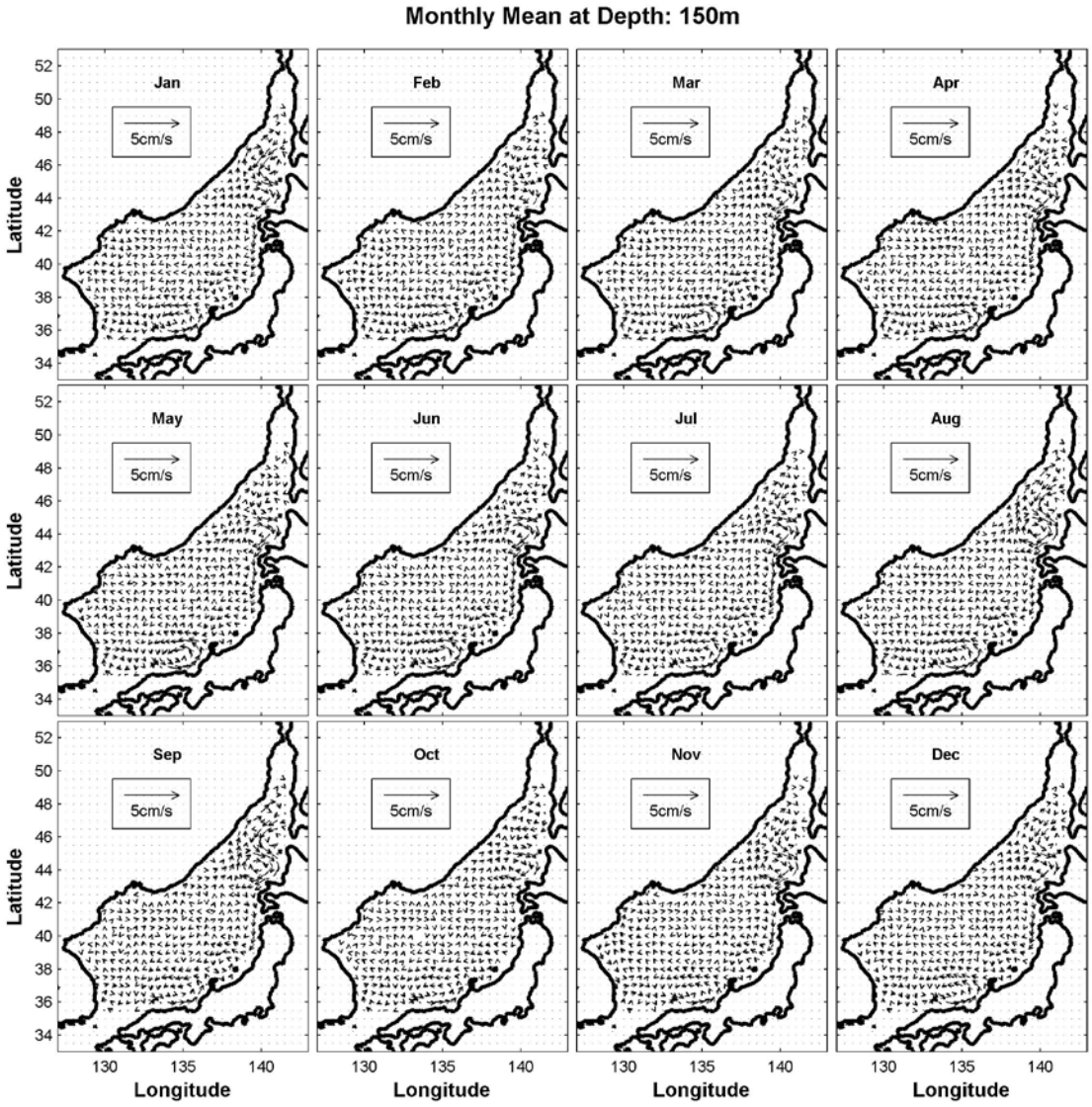
Monthly Mean at Depth: 150m
Jan
Feb
Mar
Apr
May
Jun
Jul
Aug
Sep
Oct
Nov
Dec
5cm/s
Latitude
Longitude
52
50
48
46
44
42
40
38
36
34
130
135
140

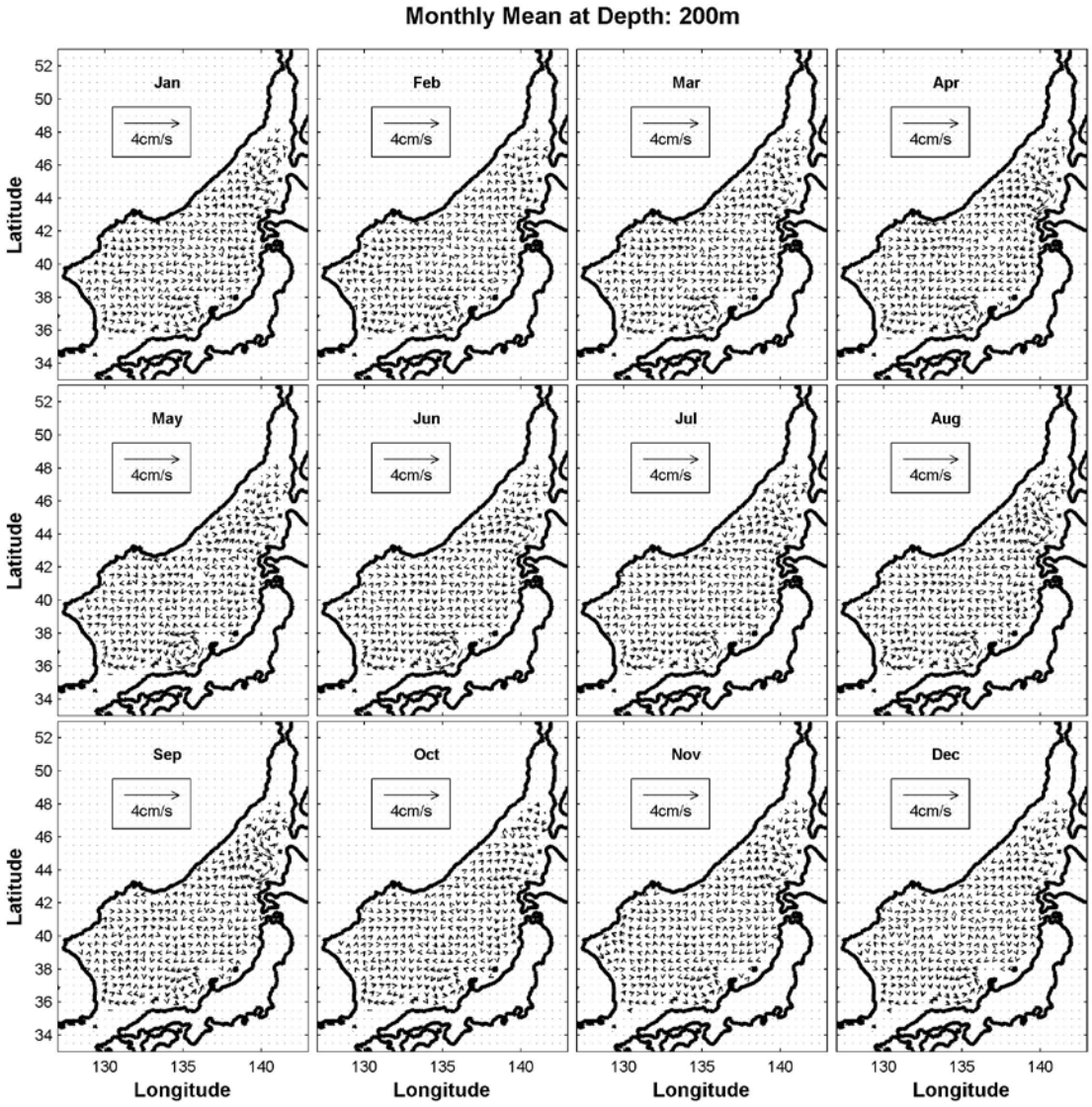
Monthly Mean at Depth: 200m
Jan
Feb
Mar
Apr
May
Jun
Jul
Aug
Sep
Oct
Nov
Dec
4cm/s
Latitude
Longitude
52
50
48
46
44
42
40
38
36
34
130
135
140

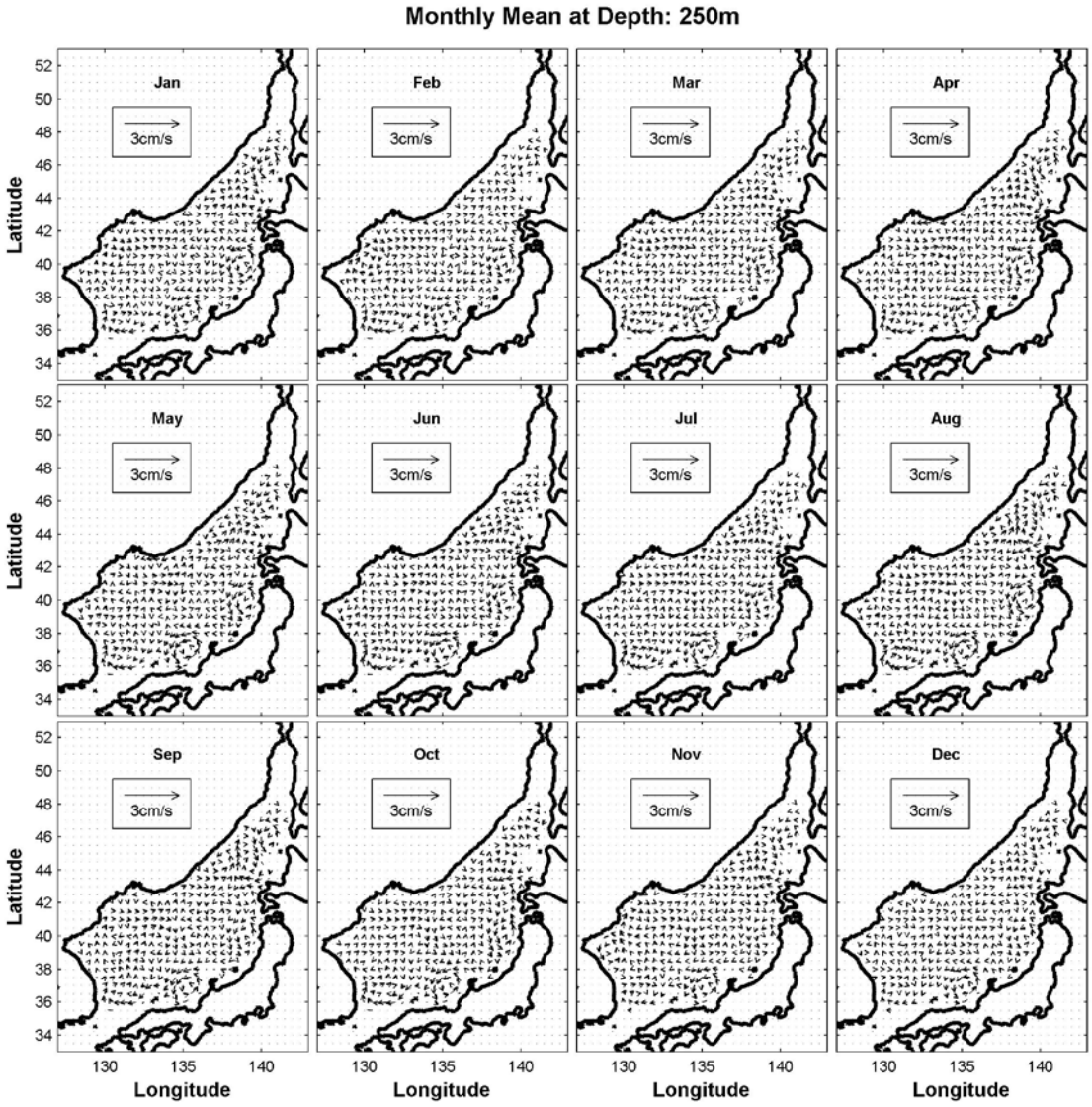
Monthly Mean at Depth: 250m
Jan
Feb
Mar
Apr
May
Jun
Jul
Aug
Sep
Oct
Nov
Dec
3cm/s
Latitude
Longitude
52
50
48
46
44
42
40
38
36
34
130
135
140

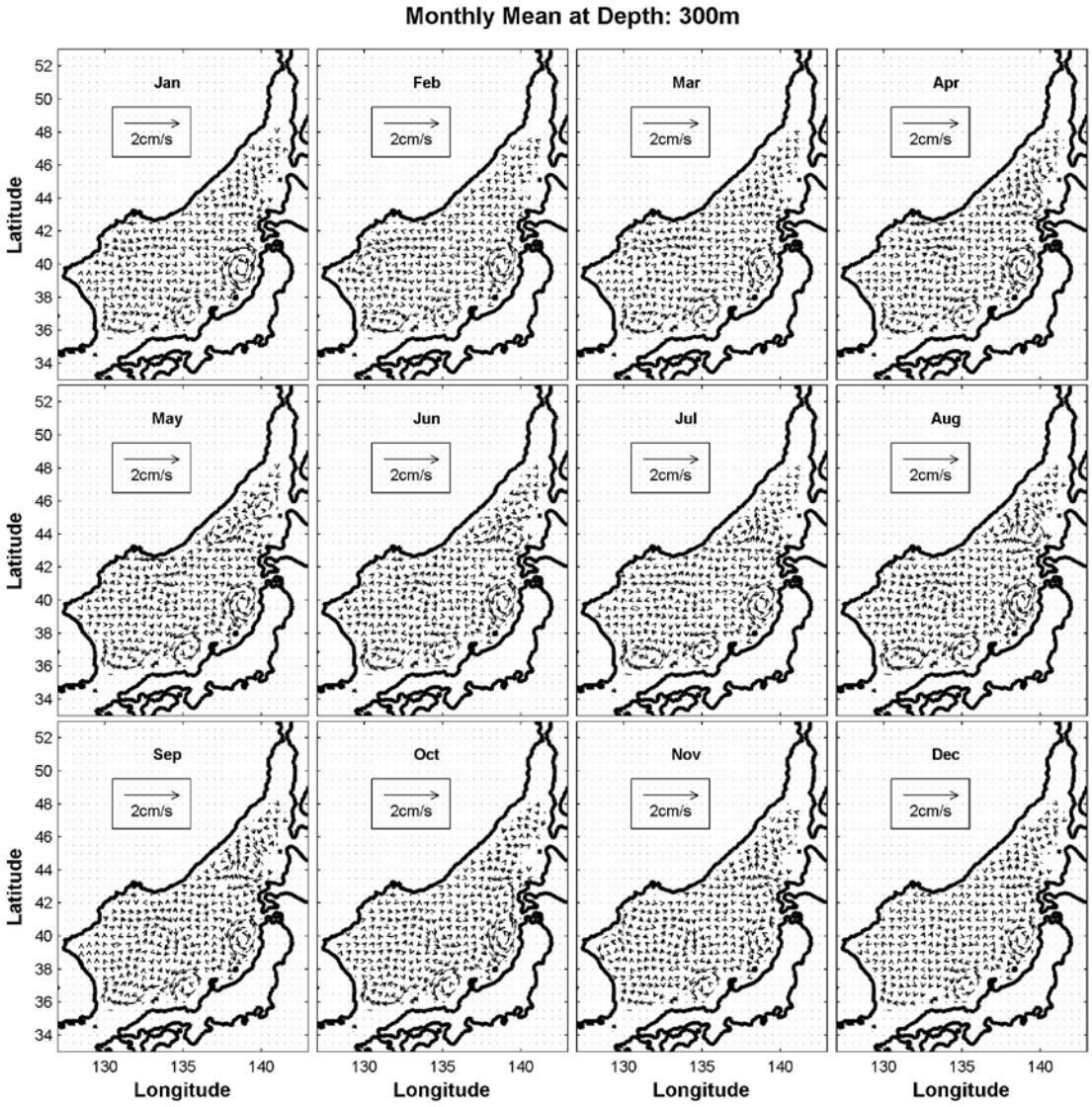
Monthly Mean at Depth: 300m
Jan
Feb
Mar
Apr
May
Jun
Jul
Aug
Sep
Oct
Nov
Dec
2cm/s
Latitude
Longitude
52
50
48
46
44
42
40
38
36
34
130
135
140

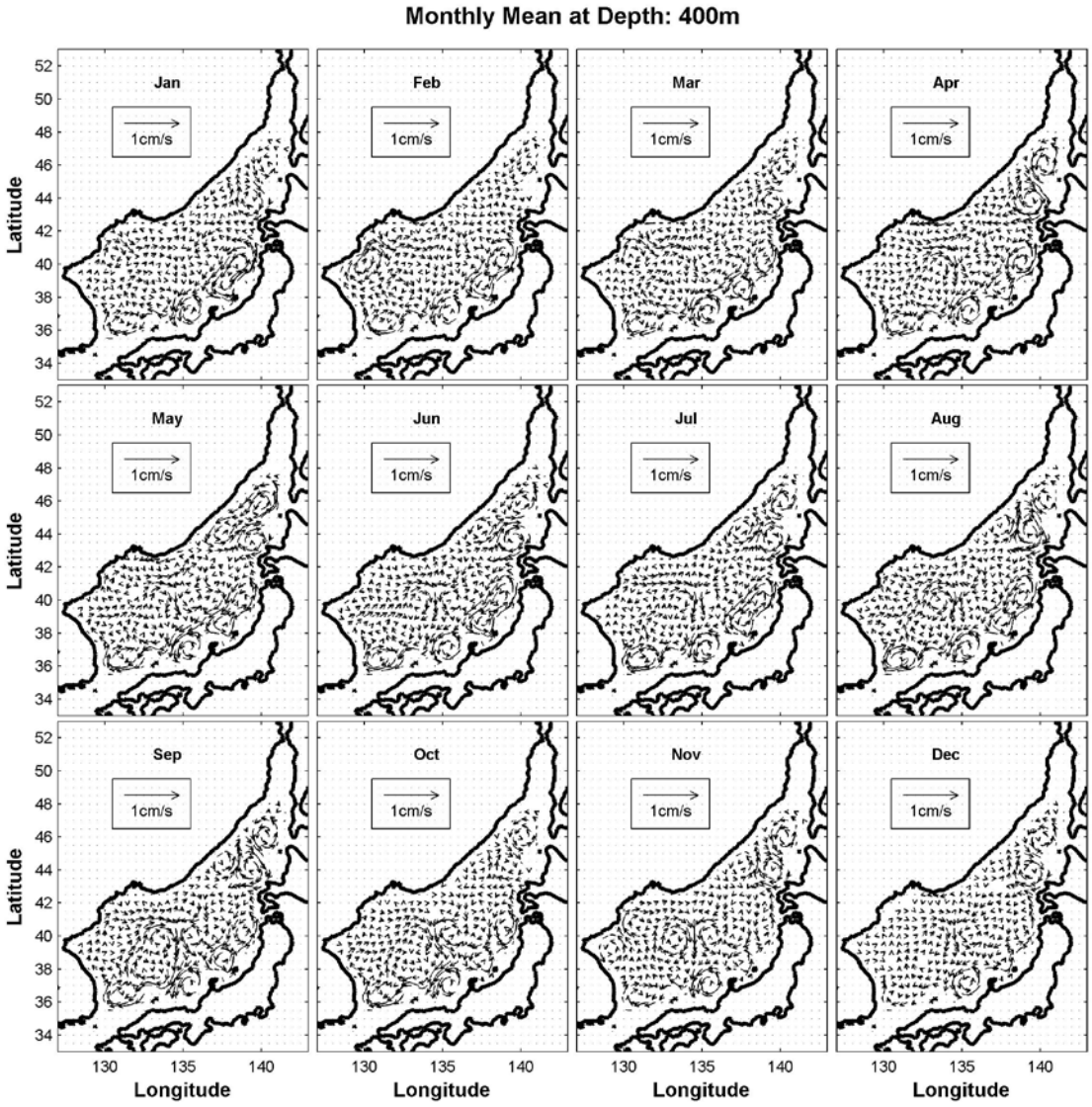
Monthly Mean at Depth: 400m
Jan
Feb
Mar
Apr
May
Jun
Jul
Aug
Sep
Oct
Nov
Dec
1cm/s
Latitude
Longitude
52
50
48
46
44
42
40
38
36
34
130
135
140

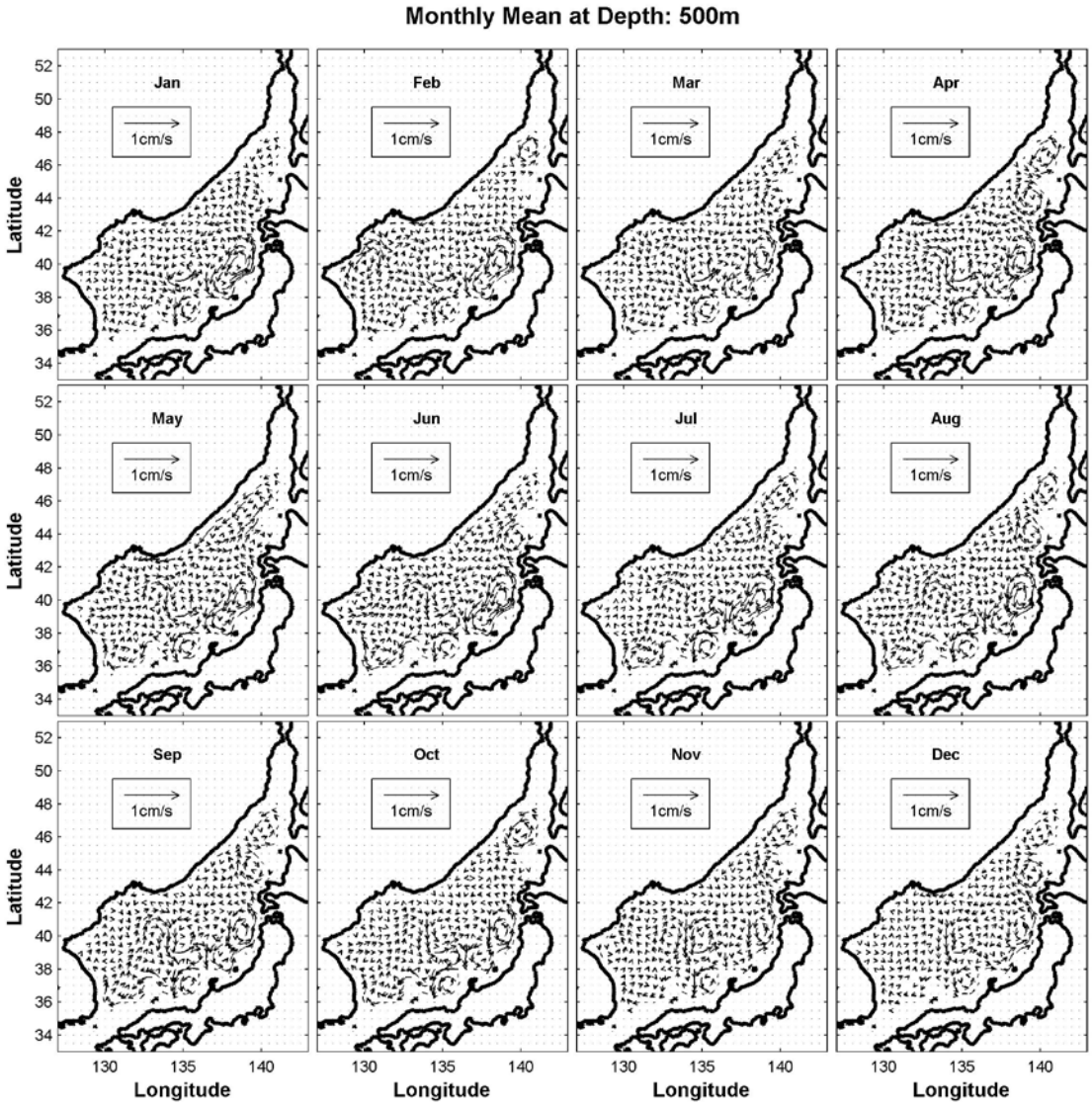
Monthly Mean at Depth: 500m
Jan
Feb
Mar
Apr
May
Jun
Jul
Aug
Sep
Oct
Nov
Dec
1cm/s
Latitude
Longitude
52
50
48
46
44
42
40
38
36
34
130
135
140

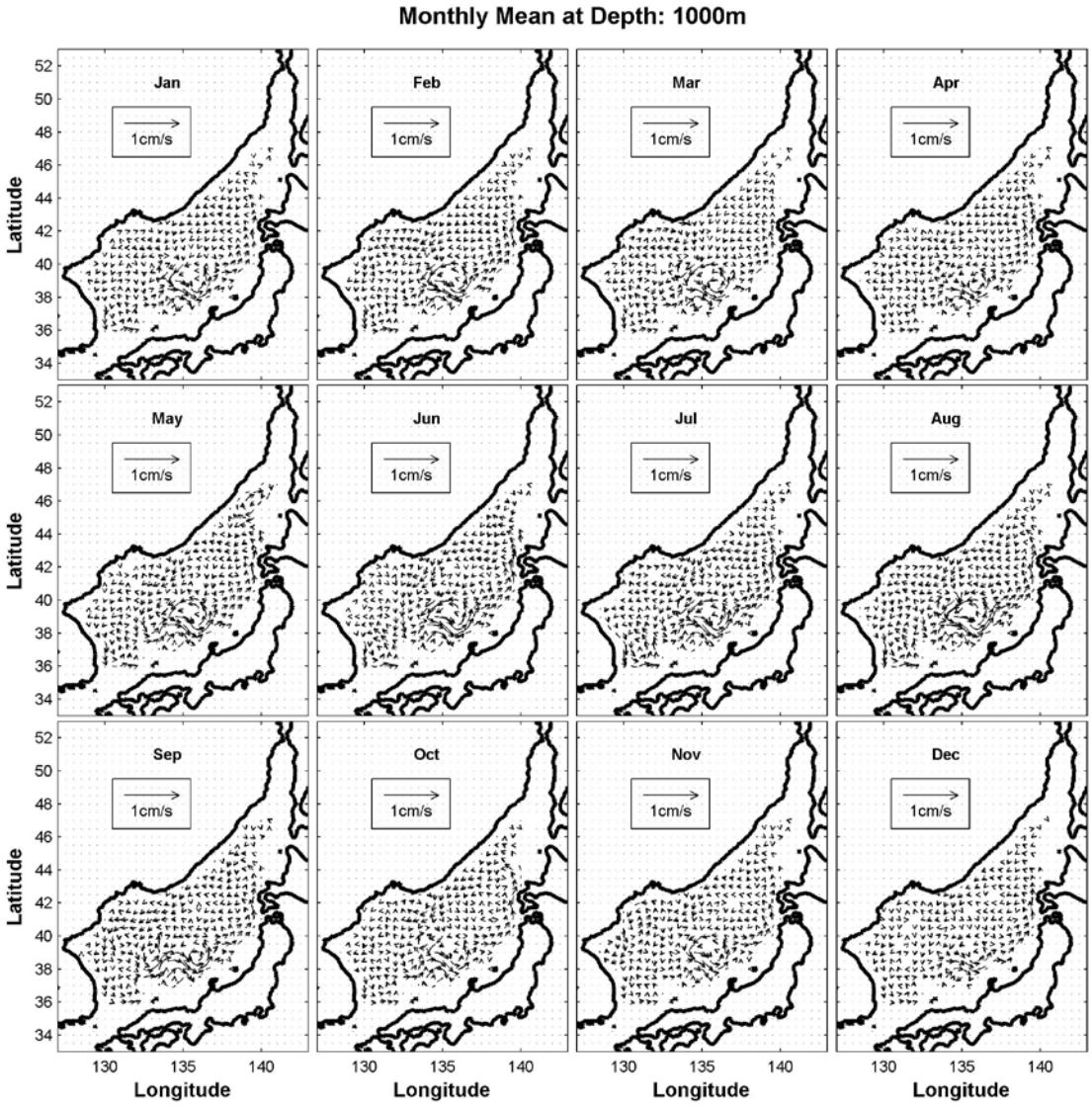
Monthly Mean at Depth: 1000m
Jan
Feb
Mar
Apr
May
Jun
Jul
Aug
Sep
Oct
Nov
Dec
1cm/s
Latitude
Longitude
52
50
48
46
44
42
40
38
36
34
130
135
140

APPENDIX B. FIRST FIVE MODES OF EOF_S

A. HEAT CONTENT

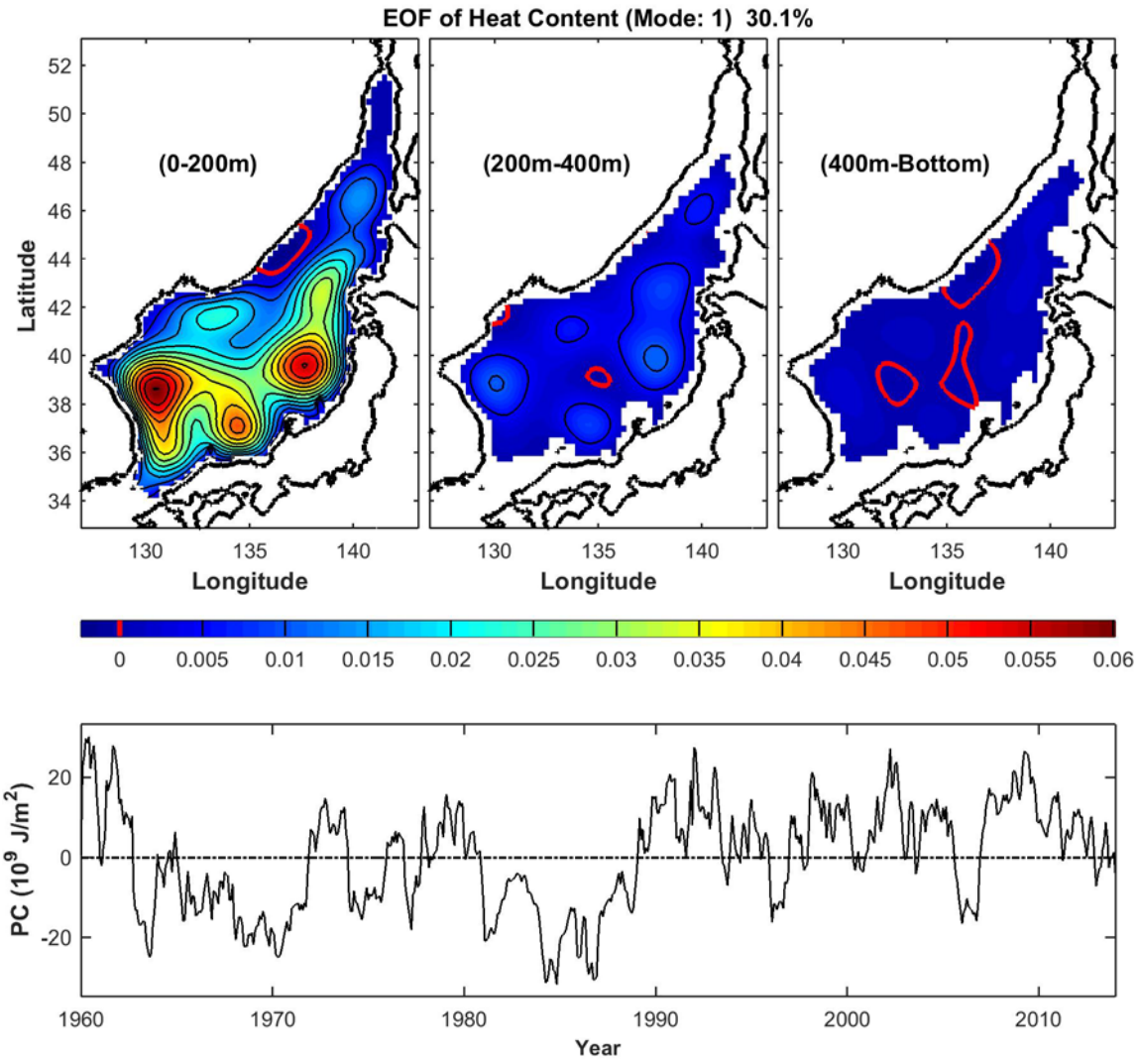

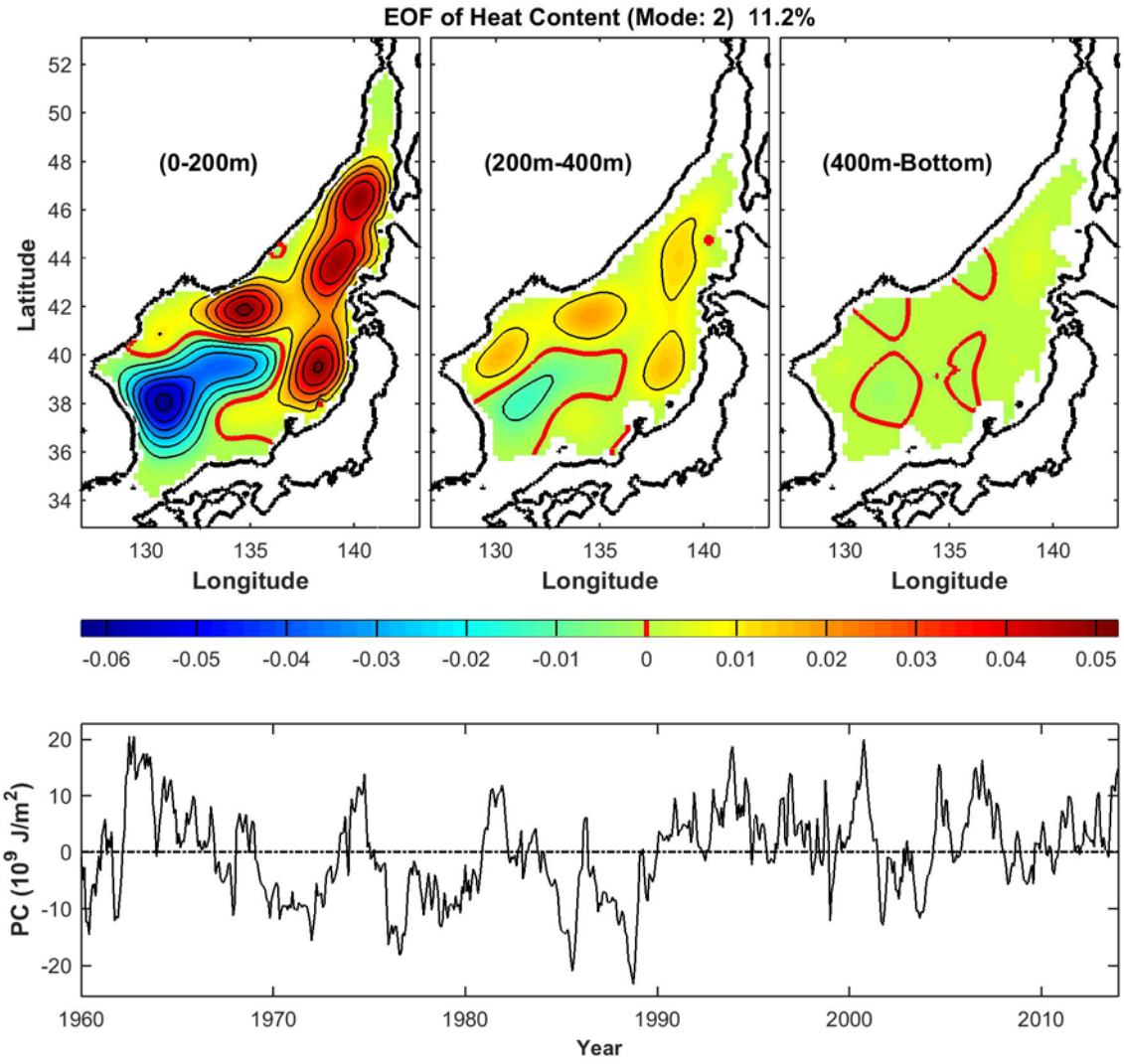
EOF of Heat Content (Mode: 2) 11.2%
(0-200m)
(200m-400m)
(400m-Bottom)
Latitude
Longitude
52
50
48
46
44
42
40
38
36
34
130
135
140
-0.06
-0.05
-0.04
-0.03
-0.02
-0.01
0
0.01
0.02
0.03
0.04
0.05
PC (10^9 J/m^2)
20
10
0
-10
-20
1960
1970
1980
1990
2000
2010
Year

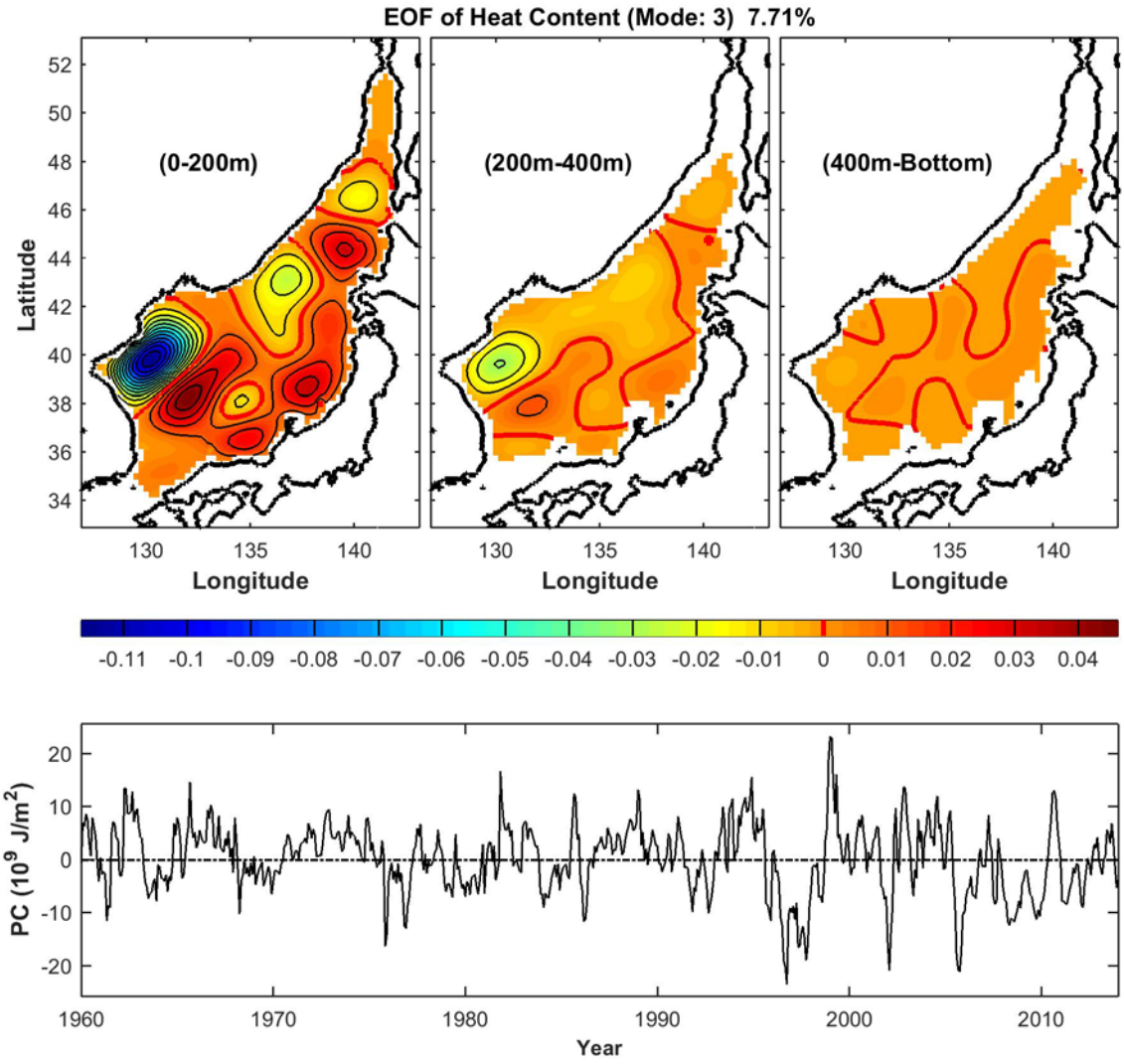
EOF of Heat Content (Mode: 3) 7.71%
(0-200m)
(200m-400m)
(400m-Bottom)
Latitude
Longitude
-0.11 -0.1 -0.09 -0.08 -0.07 -0.06 -0.05 -0.04 -0.03 -0.02 -0.01 0 0.01 0.02 0.03 0.04
PC (10^9 J/m^2)
Year

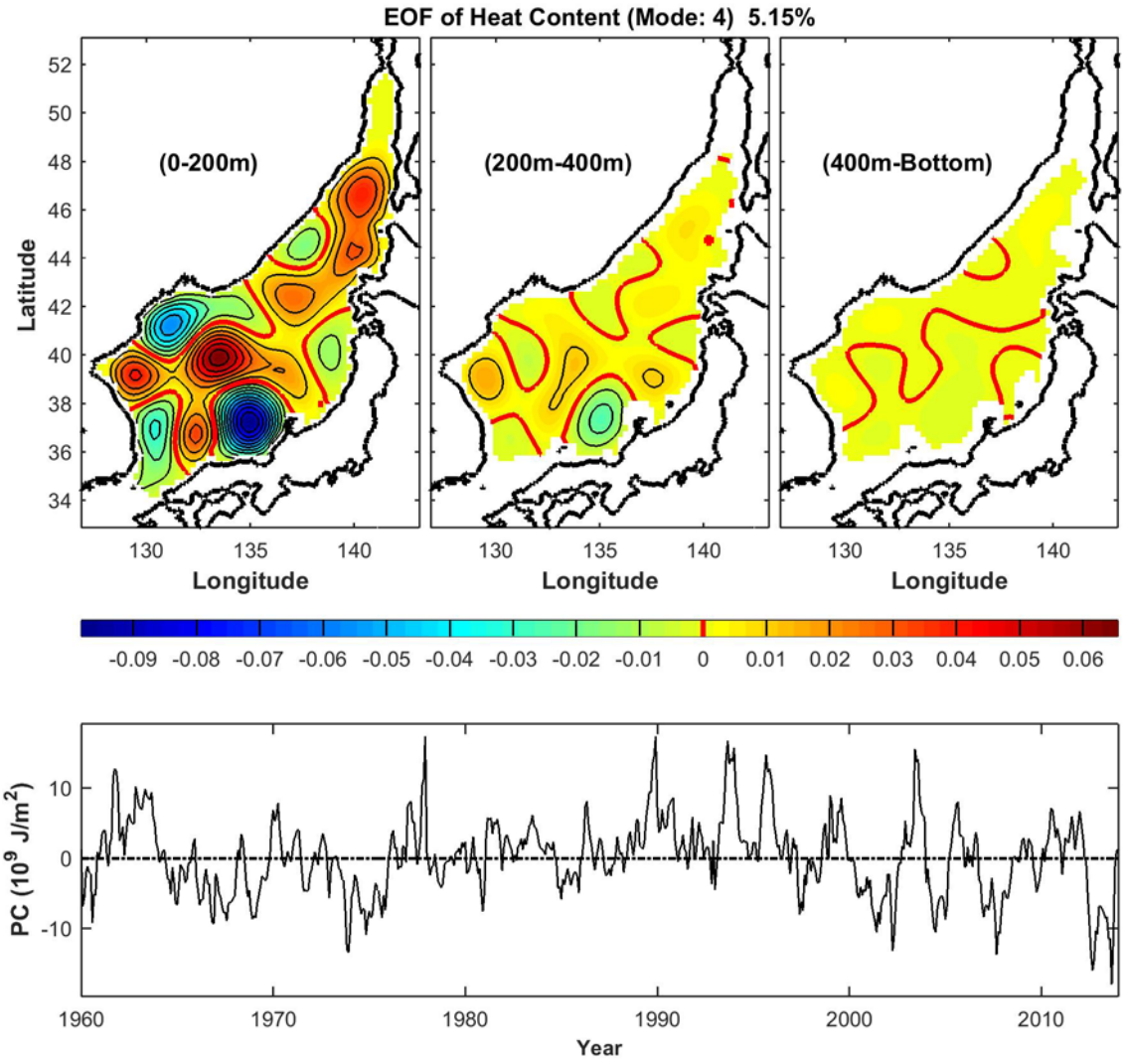
EOF of Heat Content (Mode: 4) 5.15%
(0-200m)
(200m-400m)
(400m-Bottom)
Latitude
Longitude
52
50
48
46
44
42
40
38
36
34
130
135
140
-0.09 -0.08 -0.07 -0.06 -0.05 -0.04 -0.03 -0.02 -0.01 0 0.01 0.02 0.03 0.04 0.05 0.06
PC (10^9 J/m^2)
10
0
-10
1960
1970
1980
1990
2000
2010
Year

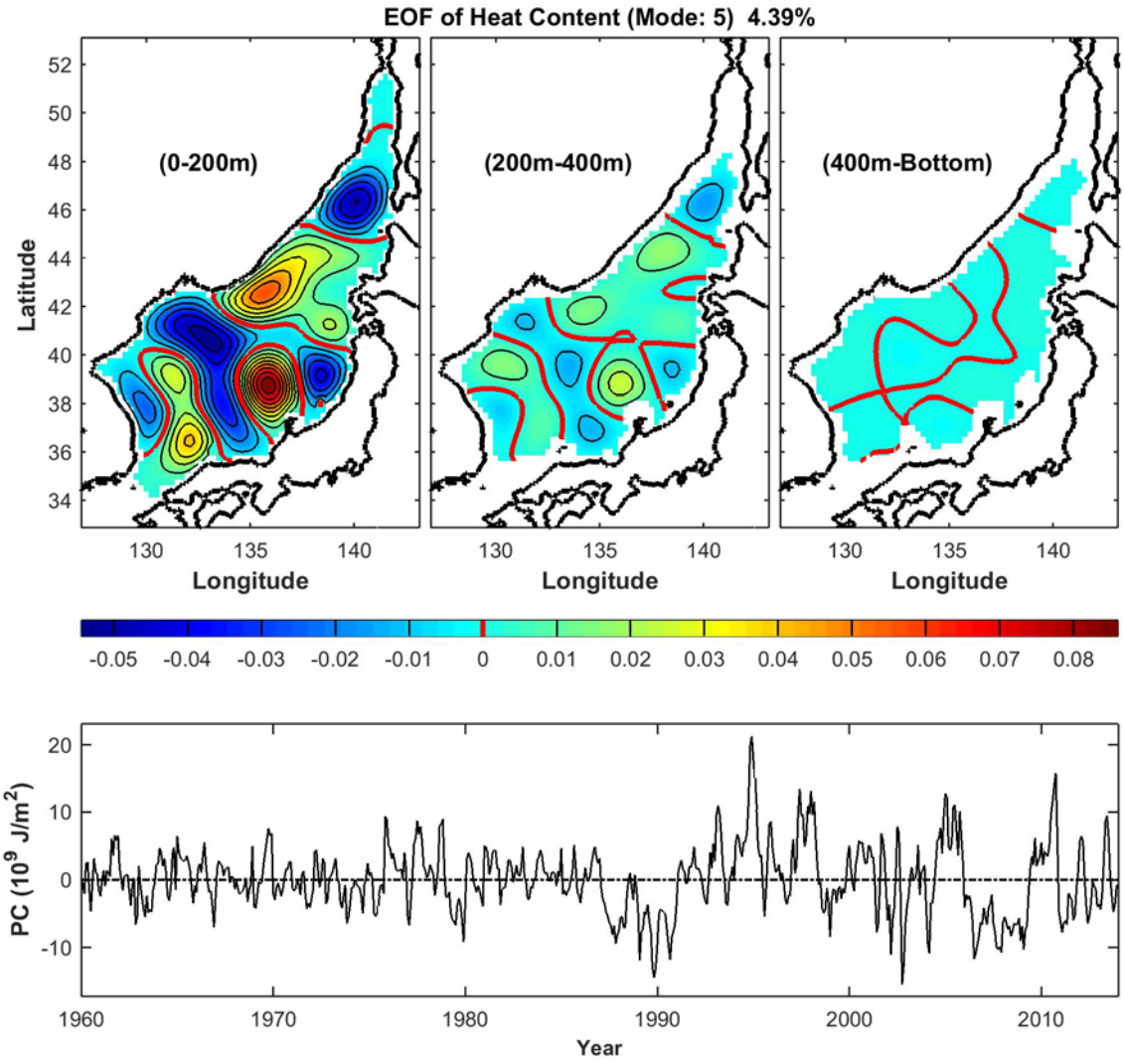
EOF of Heat Content (Mode: 5) 4.39%
(0-200m)
(200m-400m)
(400m-Bottom)
Latitude
Longitude
52
50
48
46
44
42
40
38
36
34
130
135
140
-0.05
-0.04
-0.03
-0.02
-0.01
0
0.01
0.02
0.03
0.04
0.05
0.06
0.07
0.08
PC (10^9 J/m^2)
20
10
0
-10
1960
1970
1980
1990
2000
2010
Year

B. FRESHWATER CONTENT

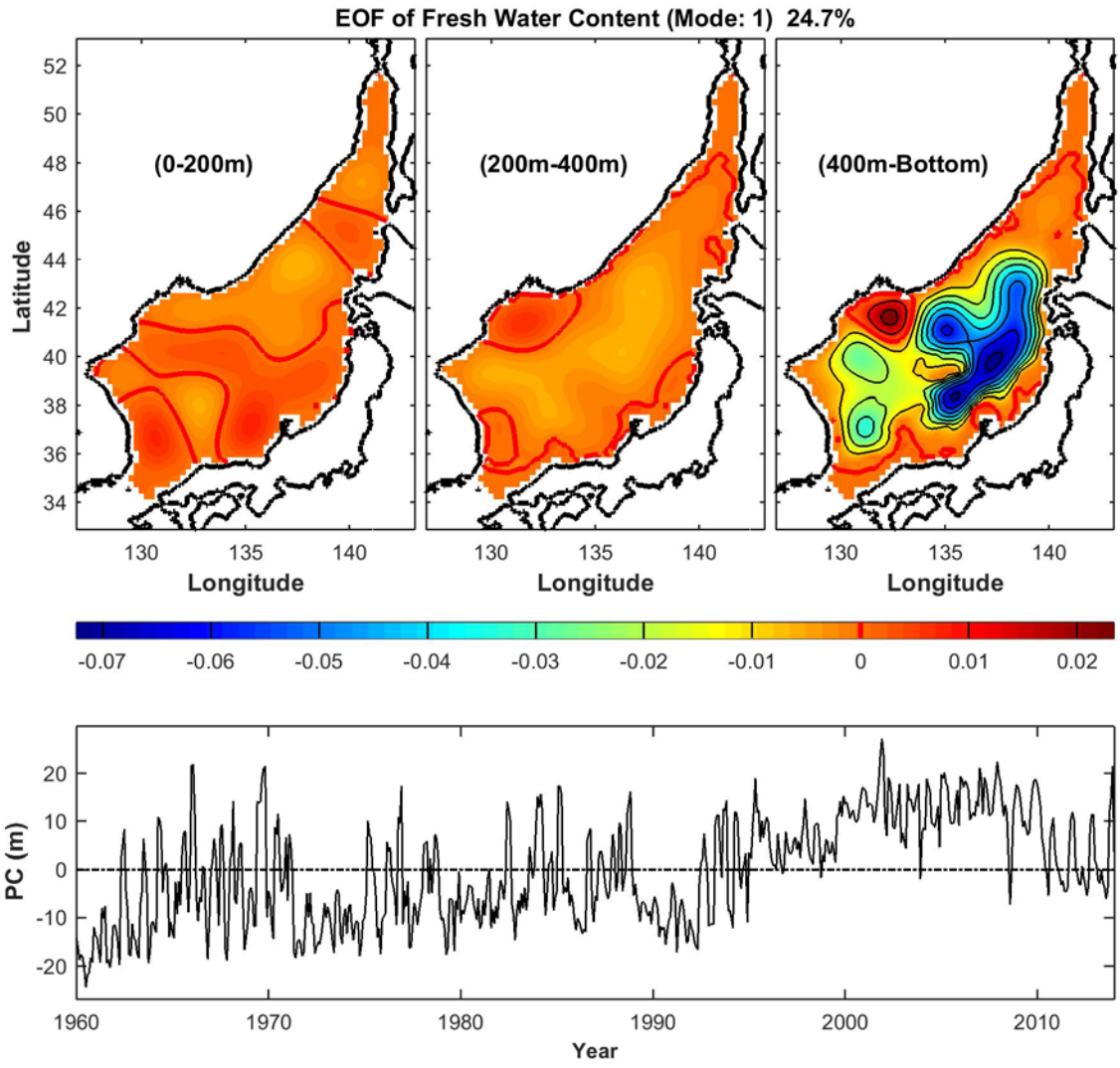

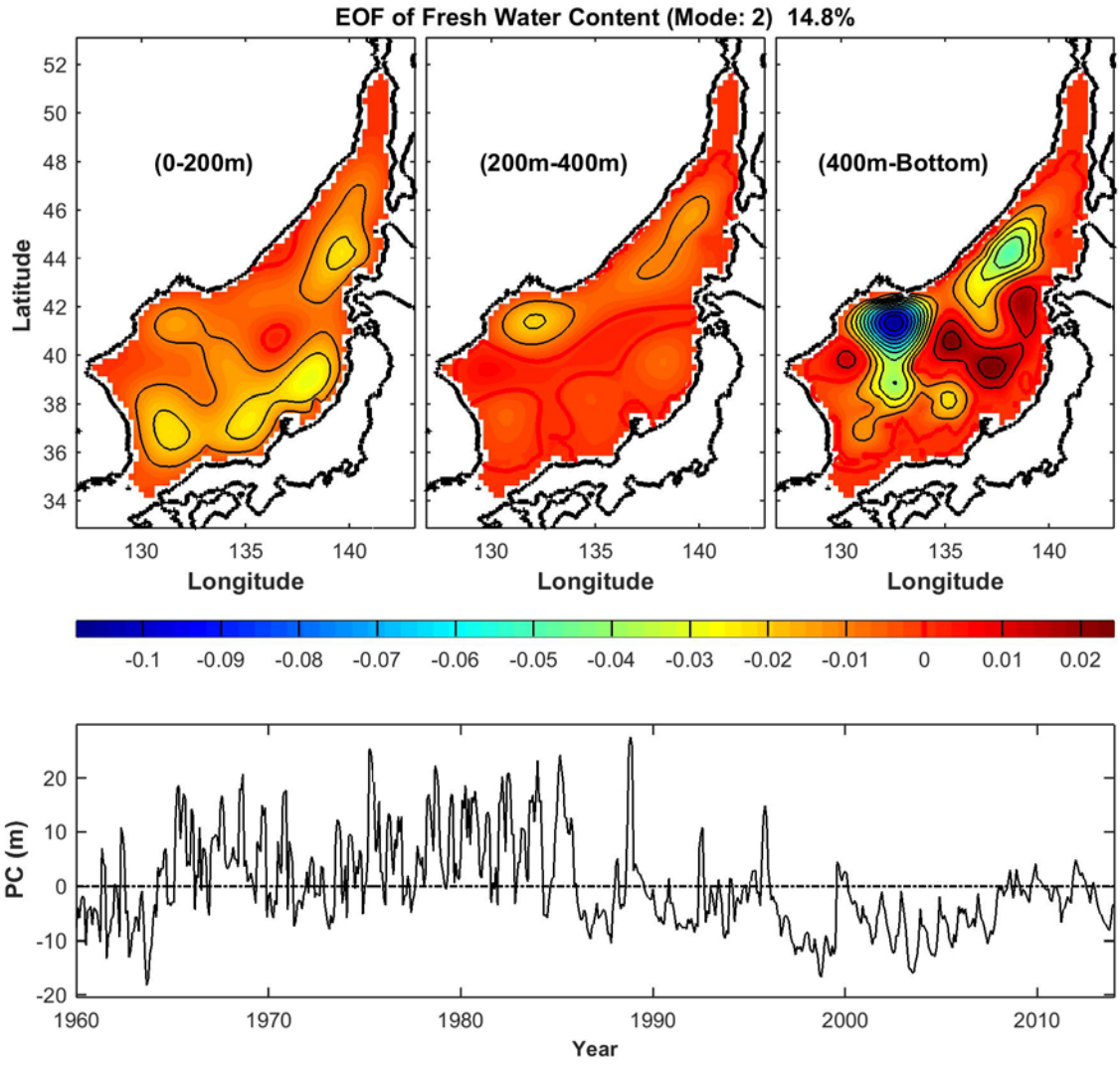
EOF of Fresh Water Content (Mode: 2) 14.8%
(0-200m)
(200m-400m)
(400m-Bottom)
Latitude
Longitude
-0.1 -0.09 -0.08 -0.07 -0.06 -0.05 -0.04 -0.03 -0.02 -0.01 0 0.01 0.02
PC (m)
Year

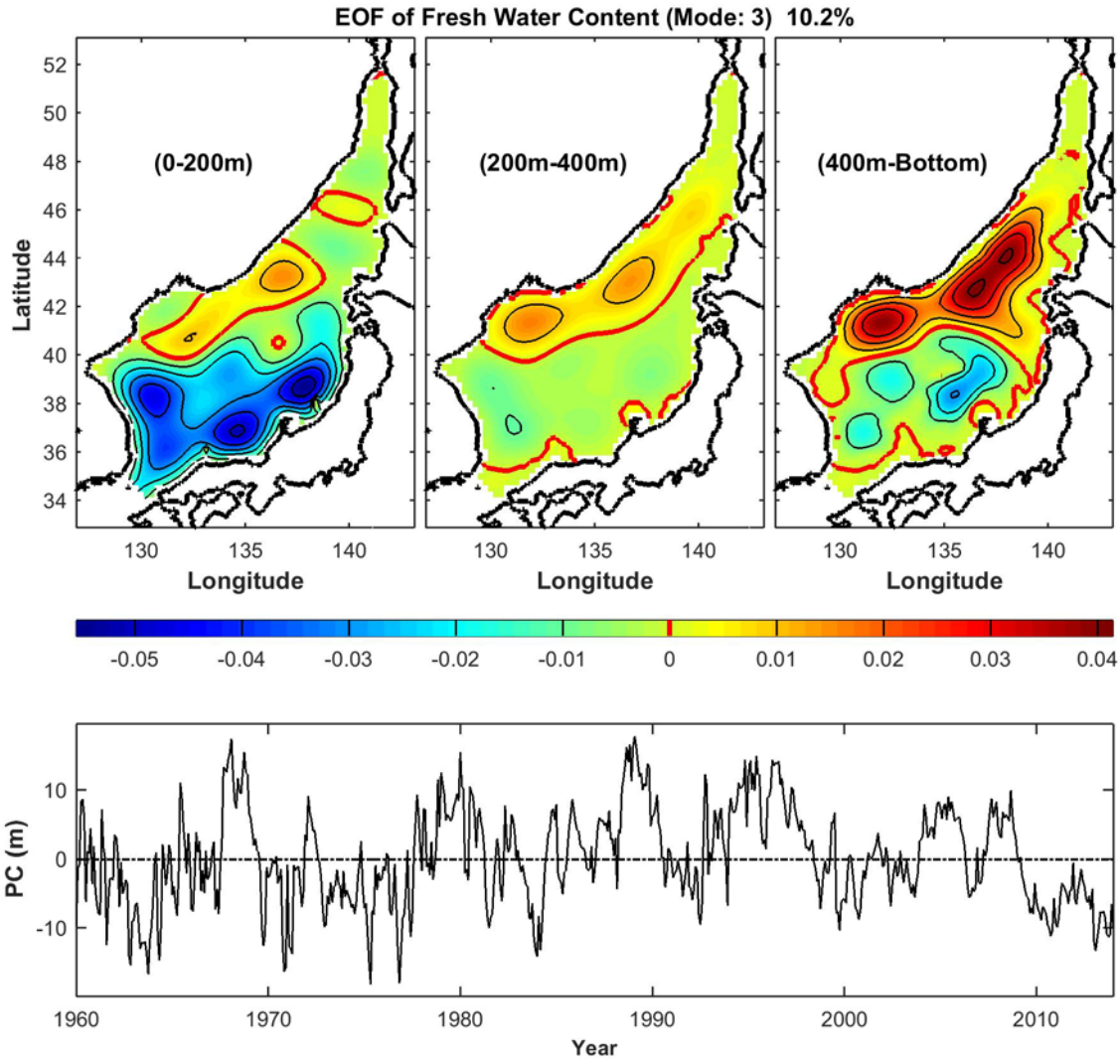
EOF of Fresh Water Content (Mode: 3) 10.2%
(0-200m)
(200m-400m)
(400m-Bottom)
Latitude
Longitude
-0.05
-0.04
-0.03
-0.02
-0.01
0
0.01
0.02
0.03
0.04
PC (m)
Year

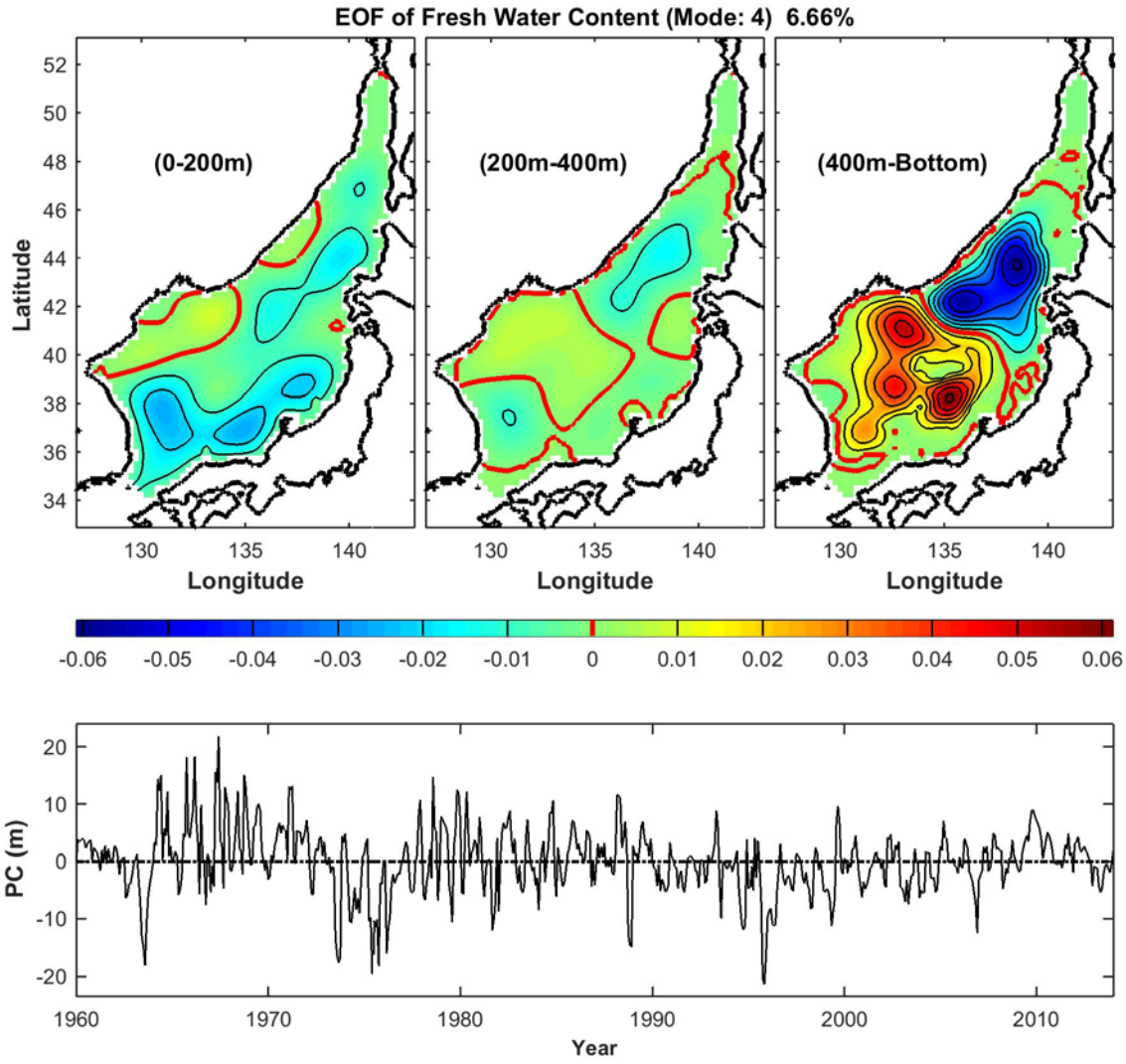
EOF of Fresh Water Content (Mode: 4) 6.66%
(0-200m)
(200m-400m)
(400m-Bottom)
Latitude
Longitude
-0.06 -0.05 -0.04 -0.03 -0.02 -0.01 0 0.01 0.02 0.03 0.04 0.05 0.06
PC (m)
Year

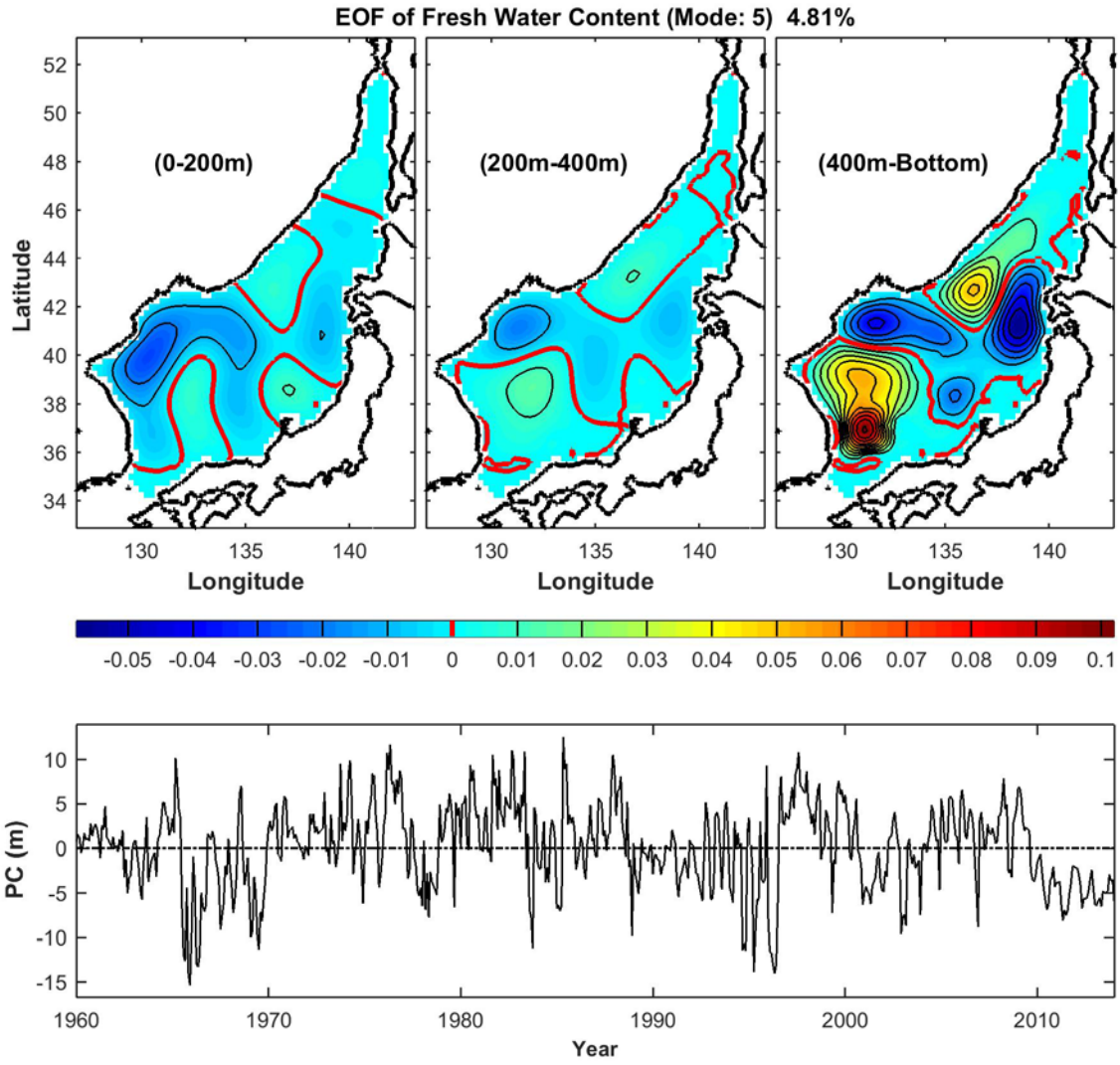
EOF of Fresh Water Content (Mode: 5) 4.81%
(0-200m)
(200m-400m)
(400m-Bottom)
Latitude
Longitude
-0.05 -0.04 -0.03 -0.02 -0.01 0 0.01 0.02 0.03 0.04 0.05 0.06 0.07 0.08 0.09 0.1
PC (m)
Year

LIST OF REFERENCES

Ashjian, C. J., R. Arnone, C. S. Davis, B. Jones, M. Kahru, C. M. Lee, and B. G. Mitchell, 2006: Biological structure and seasonality in the Japan/East Sea.

Beardsley, R., R. Limeburner, H. Yu, and G. Cannon, 1985: Discharge of the Changjiang (Yangtze river) into the East China sea. *Cont.Shelf Res.,* **4**, 57–76.

Bogdanov, N. A., 1984: *Proceedings of the 27th International Geological Congress: Geology of ocean basins.* Vol. 6, VSP International Science.

Boyer, T. P., J. I. Antonov, O. K. Baranova, C. Coleman, H. E. Garcia, A. Grodsky, D. R. Johnson, R. A. Locarnini, A. V. Mishonov, and T. D. O'Brien, 2013: NOAA Atlas NESDIS 72.

Center for Marine Environmental Sciences, 2015: General Geology / Marine Geology. Accessed 10 December 2015. [Available online at http://www.marum.de/en/general_geology__marine_geology.html]

Chang, K., C. Zhang, C. Park, D. Kang, S. Ju, S. Lee, and M. Wimbush, 2015: Oceanography of the East Sea (Japan Sea).

Chu, P. C., 2006: Inverted Circulations in the Pacific Basin. *P-Vector Inverse Method,* 249–363.

Chu, P. C., C. Fan, and W. Cai, 1998: P-vector inverse method evaluated using the Modular Ocean Model (MOM). *J.Oceanogr.,* **54**, 185–198.

Chu, P. C., C. Fang, and C. S. Kim, 2005: Japan/East Sea model predictability. *Cont.Shelf Res.,* **25**, 2107–2121.

Chu, P. C., H. Tseng, C. Chang, and J. Chen, 1997: South China Sea warm pool detected in spring from the Navy's master oceanographic observational data set (MOODS). *Journal of Geophysical Research: Oceans (1978–2012),* **102**, 15761-15771.

Chu, P. C., J. Lan, and C. Fan, 2001: Japan Sea thermohaline structure and circulation. Part I: Climatology. *J.Phys.Oceanogr.,* **31**, 244–271.

Chu, P. C., R. T. Tokmakian, C. Fan, and L. C. Sun, 2015: Optimal Spectral Decomposition (OSD) for Ocean Data Assimilation. *J.Atmos.Ocean.Technol.,* **32**, 828–841.

CIA The World Factbook, 2015: Country Comparison / Exports. Accessed 10 December 2015. ; https://www.cia.gov/library/publications/the-world-factbook/rankorder/2078rank.html]

Conkright, M. E., S. Levitus, and T. P. Boyer, 1994: *World Ocean Atlas: 1994 Nutrients.* Vol. 1, DIANE Publishing, .

Danchenkov, M. A., V. B. Lobanov, S. C. Riser, K. Kim, M. Takematsu, and J. Yoon, 2006: A history of physical oceanographic research in the Japan/East Sea. *Oceanography-Washington Dc-Oceanography Society*, **19**, 18.

Dobrovolsky, A., B. Zalogin, 1982: Seas of the USSR. *M/Publications of MSU, .*

Dorman, C. E., C. A. Friehe, D. Khelif, A. Scotti, J. Edson, R. C. Beardsley, R. Limeburner, and S. S. Chen, 2006: Winter atmospheric conditions over the Japan/East Sea: The structure and impact of severe cold-air outbreaks. *Oceanography-Washington Dc-Oceanography Society*, **19**, 96.

Dorman, C. E., R. C. Beardsley, N. Dashko, C. Friehe, D. Kheilf, K. Cho, R. Limeburner, and S. Varlamov, 2004: Winter marine atmospheric conditions over the Japan Sea. *Journal of Geophysical Research: Oceans (1978–2012),* **109**.

Englezos, P., J. D. Lee, 2005: Gas hydrates: A cleaner source of energy and opportunity for innovative technologies. *Korean Journal of Chemical Engineering,* **22**, 671–681.

Global Firepower (GFP), 2015: 2015 World Military Strength Rankings. Accessed 10 December 2015. [Available online at http://www.globalfirepower.com/]

Hoiles, P. W., S. J. Gallagher, A. Kitamura, and J. M. Southwood, 2012: The evolution of the Tsushima Current during the early Pleistocene in the Sea of Japan: An example from marine isotope stage (MIS) 47. *Global Planet Change*, **92**, 162–178.

IHS Jane's 360, 2015: China, Russia conduct large-scale joint naval exercise. Accessed 10 December 2015. [Available online at http://www.janes.com/article/53759 /china-russia-conduct-large-scale-joint-naval-exercise]

Kantha, L., P. Pontius, and V. Anantharaj, 1994: Tides in marginal, semi-enclosed and coastal seas, part I: sea surface height. *Mississippi State University, http://www.cast.msstate.edu/Tides2D, .*

Kim, K., J. Chung, 1984: On the salinity-minimum and dissolved oxygen-maximum layer in the East Sea (Sea of Japan). *Elsevier oceanography series,* **39**, 55–65.

Kim, K., K. Kim, D. Min, Y. Volkov, J. Yoon, and M. Takematsu, 2001: Warming and structural changes in the East (Japan) Sea: a clue to future changes in global oceans? *Geophys.Res.Lett.,* **28**, 3293–3296.

Kim, K., K. Kim, Y. Kim, Y. Cho, D. Kang, M. Takematsu, and Y. Volkov, 2004: Water masses and decadal variability in the East Sea (Sea of Japan). *Prog.Oceanogr.*, **61**, 157–174.

Lee, J., J. Y. Lee, Y. M. Kim, and C. Lee, 2013: Stress-dependent and strength properties of gas hydrate-bearing marine sediments from the Ulleung Basin, East Sea, Korea. *Mar.Pet.Geol.,* **47**, 66–76.

Legeckis, R., 1978: A survey of worldwide sea surface temperature fronts detected by environmental satellites. *Journal of Geophysical Research: Oceans (1978–2012),* **83**, 4501–4522.

Levitus, S., J. Antonov, O. Baranova, T. Boyer, C. Coleman, H. Garcia, A. Grodsky, D. Johnson, R. Locarnini, and A. Mishonov, 2013: The World Ocean Database. *Data Science Journal,* **12**, WDS229-WDS234.

National Geographic Information Institute, 2015: The Geography of Dokdo. Accessed 10 December 2015. [Available online at http://www.ngii.go.kr/dokdoen/contents/contentsView.do?rbsIdx=54#none]

Park, K., J. Y. Chung, and K. Kim, 2004a: Sea surface temperature fronts in the East (Japan) Sea and temporal variations. *Geophys.Res.Lett.,* **31**.

Park, K., J. Y. Chung, K. Kim, and P. C. Cornillon, 2005: Wind and bathymetric forcing of the annual sea surface temperature signal in the East (Japan) Sea. *Geophys.Res.Lett.,* **32**.

Park, Y., A. Choi, Y. H. Kim, H. S. Min, J. H. Hwang, and S. Choi, 2010: Direct flows from the Ulleung Basin into the Yamato Basin in the East/Japan Sea. *Deep Sea Research Part I: Oceanographic Research Papers,* **57**, 731–738.

Park, Y., K. Oh, K. Chang, and M. Suk, 2004b: Intermediate level circulation of the southwestern part of the East/Japan Sea estimated from autonomous isobaric profiling floats. *Geophys.Res.Lett.,* **31**.

Ryu, B., M. Riedel, J. Kim, R. D. Hyndman, Y. Lee, B. Chung, and I. Kim, 2009: Gas hydrates in the western deep-water Ulleung Basin, East Sea of Korea. *Mar.Pet.Geol.,* **26**, 1483–1498.

Senjyu, T., H. Shin, J. Yoon, Z. Nagano, H. An, S. Byun, and C. Lee, 2005: Deep flow field in the Japan/East Sea as deduced from direct current measurements. *Deep Sea Research Part II: Topical Studies in Oceanography,* **52**, 1726–1741.

Tachibana, Y., K. Oshima, and M. Ogi, 2008: Seasonal and interannual variations of Amur River discharge and their relationships to large-scale atmospheric patterns and moisture fluxes. *Journal of Geophysical Research: Atmospheres (1984–2012),* **113**.

Tada, R., T. Irino, and I. Koizumi, 1999: Land-ocean linkages over orbital and millennial timescales recorded in Late Quaternary sediments of the Japan Sea. *Paleoceanography,* **14**, 236–247.

Talley, L. D., V. A. Luchin, V. I. Ponomarev, A. N. Salyuk, A. Y. Shcherbina, P. Y. Tishchenko, and I. Zhabin, 2006: Water Masses. *Oceanography,* **19**, 32.

Teague, W. J., D. S. Ko, G. A. Jacobs, H. T. Perkins, J. W. Book, S. R. Smith, K. Chang, M. Suk, K. Kim, and S. J. Lyu, 2006: *Currents through the Korea/Tsushima Strait: a review of LINKS observations,* .

Watanabe, T., O. Katoh, and H. Yamada, 2006: Structure of the Tsushima warm current in the northeastern Japan Sea. *J.Oceanogr.,* **62**, 527–538.

Woo-Seok, K., P. Watts, 2012: *The Plant Geography of Korea: with an emphasis on the Alpine Zones.* Vol. 19, Springer Science & Business Media, .

Yoon, J., 1982: Numerical experiment on the circulation in the Japan Sea. *Journal of the Oceanographical Society of Japan,* **38**, 81–94.

INITIAL DISTRIBUTION LIST

1. Defense Technical Information Center
   Ft. Belvoir, Virginia

2. Dudley Knox Library
   Naval Postgraduate School
   Monterey, California